Systems, materials, and methodologies for multi-material hybrid additive manufacturing functionally graded structures

by

Esmat Sheydaeian

A thesis
presented to the University of Waterloo
in fulfillment of the
thesis requirement for the degree of
Doctor of Philosophy
in
Mechanical and Mechatronics Engineering

Waterloo, Ontario, Canada, 2017

Examining Committee Membership
The following served on the Examining Committee for this thesis. The decision of the Examining Committee is by majority vote.

External Examiner NAME:	R. Jill Urbanic
	Title: Associate Professor
Supervisor(s) NAME:	Ehsan Toyserkani
	Title: Professor
Internal Member NAME:	Mihaela Vlasea
	Title: Assistant Professor
Internal Member NAME:	Behrad Khamesee
	Title: Professor
Internal-external Member NAME:	Leonardo Simon
	Title: Professor

Author's Declaration

This thesis consists of material all of which I authored or co-authored: see Statement of Contributions included in the thesis. This is a true copy of the thesis, including any required final revisions, as accepted by my examiners.

I understand that my thesis may be made electronically available to the public.

Statement of Contributions

I would like to acknowledge the names of my co-authors who contributed to the research described in this dissertation, these include:

Prof. Ehsan Toyserkani: supervision of the research, providing original idea for the current thesis, editing papers, providing lab facilities

Prof. Mihaela Vlasea: brainstorming, editing paper

Prof. Pu Chen: providing lab facilities

Kaveh Sarikhani: running the experiments, analyzing the data, editing paper

Zachary Fishman: running the experiments, editing paper

Abstract

Over the last three decades, additive manufacturing (AM), which is based on fashioning 3D objects through a layer-by-layer construction, has greatly expanded. The progress in this field is due to the capability of fabricating parts with more complexity in the topology and diversity in the array of applicable materials. One such an example is structuring of cellular solids and composite materials appropriate for the vast range of applications.

Among different AM methods, powder-bed AM of heterogeneous structures has been utilized to make complex parts. However, the adoption of this process is hindered due to the inability to create closed internal channels that is an essential factor, defining the properties of solids. This inability is mainly related to the de-powdering issue associated with trapped powders inside closed voids. A novel combined approach has been used to attain the design criteria, by selectively encapsulating sacrificial materials within the designated layers during manufacturing and decomposing the substances in post-processing steps.

The main objective of this dissertation is to investigate two hypothesized methods for the functional printing of titanium cellular structures with graded pores arranged in a controlled manner. The products in this study were characterized through employing several methods including shrinkage measurements, porosity measurement, mechanical compression test, hardness test, scanning electron microscopy, micro and nano computerized tomography, and X-ray diffraction.

The employed methodologies have been classified into two approaches according to the shape of the secondary material embedded into the main substance: 1) crystalline solid particles and 2) liquid resin droplets. For the first approach, a micro-punching system was proposed as a means of positioning the sacrificial particles at designated locations in the AM process. The prototype of the unit was developed and its performance and quality of the products were evaluated. The performance analysis revealed the potential of deploying the method for selective encapsulation of particles from multiple materials and different sizes: (0.3±0.0) µm-(0.5±0.0) µm.

In the second approach, an application of a hybrid AM system integrating binder jetting and material extrusion is investigated to form the graded cellular solids. A proper polymeric sacrificial resin combined bisphenol-A ethoxylated diacrylate and cellulose acetate butyrate was developed to attain the green specimens' quality and the dimensional accuracy in the morphology of the encapsulated pores. The statistical significance of employing this method was explored on the mechanical and porosity of the titanium structures. Compare to the standard samples (no polymer included), the porosity was increased between 6% to 16% depending on the polymer layout in the structures. The stiffness and yield stress measurements suggested a range of 2.48±0.37 GPa to 3.55±0.49 GPa and 107.65±18.14 MPa to

145.75±13.85 MPa, respectively. Moreover, the influence of layer thickness and binder saturation level while selectively varied throughout the structure was evaluated to accompany the proposed ideas.

Additionally, a novel hybrid AM approach was introduced for developing titanium matrix composites. A highly loaded titanium di-boride ceramic resin was developed and pressure-less sintering protocols were adapted. The quality of the composite with graded periodic reinforcement was determined. Evaluating the data suggested a higher possibility for the formation and growth of titanium boride whisker as the temperature elevated in the heat treatment step (1400°C). The stiffness of the samples was enhanced significantly by increasing the temperature and volume fraction of reinforcement elements. In particular, those samples sintered up to 1400°C displayed 6.4% to 15.2% improvement in the stiffness. The similar improvement trend in the density of the porous matrix was observed (4.5%-19%).

The pore morphology and properties of the Ti structures developed in this thesis are comparable with the size of trabecular separation and properties of the cancellous bones. However, the proposed studies can be deployed in other applications which required the production of lightweight structures.

Acknowledgment

First, I would like to express my sincere gratitude to my supervisor, Dr. Ehsan Toyserkani, who has patiently guided and endlessly assisted me throughout my time as his student. I will forever be indebted by his guidance and support.

I hereby acknowledge my thesis examining committee members, Dr. Jill Urbanic from the University of Windsor, Dr. Leonardo Simon, Dr. Behrad Khamesee, and Dr. Mihaela Vlasea from the University of Waterloo for taking the time to review my thesis and provide valuable feedback.

I would also like to acknowledge Natural Sciences and Engineering Research Council of Canada (NSERC), the Federal Economic Development Agency for Southern Ontario (FedDev Ontario), and the University of Waterloo and the Department of Mechanical and Mechatronics Engineering for financial support of the project.

I would like to thank my current and past Multi-Scale Additive Manufacturing (MSAM) colleagues at the University of Waterloo, Dr. Ehsan Marzbanrad, Dr. Ahmad Basalah, Dr. Elahe Jabari, Dr. Amir Azhari, Dr. Olivier Jay, Dr. Mehrnaz Salarian, Dr. Haniyeh Fayazfar, Dr. Yahya Mahmoodkhani, Farzad Liravi, Bahare Marzbanrad, Yuze Huang, Zhidong (Brian) Zhang, Evan Wheat, Henry Ma, Philippe Meszaros, Richard Liang, Farid Behzadian, Xixi Zhang, Ami Woo, Carole Villian, Lisa Brock, Issa Rishmawi, Laurie Wilfong, Jerry Ratthapakdee, and Karl Rautenberg for their friendship and assistance.

I sincerely thank Dr. Pu Chen, Dr. Adrian Gerlich, Dr. Robert Pilliar, Dr. Cari Whyne, Dr. Eugene Hu, Dr. Boxin Zhao, Dr. William Melek, Dr. Michael Collins, Dr. Baris Fidan, Dr. Stefan Rehm, Dr. Nancy Oczowski, Dr. Shreyas Sundaram, Dr. Jeffery Orchard, Dr. Kaveh Sarikhani, Dr. James Hinebaugh, Dr. Craig Metcalfe, Dr. Alireza Zehtab Yazdi, Dr. Hamed Shahsavan, Zachary Fishman and Abdelbaset R.H. Midawi for their support in completing this research and my PhD.

I would like to express my gratitude and appreciation to the staffs of the Department of Mechanical and Mechatronics engineering at the University of Waterloo, Dr. Yuquan Ding, Mark Griffett, Robert Wagner, Martha Morales, William Penney, Andy Barber, Eugene Li, Neil Griffett, James Merli, Jian Zou, Allison Walker, Karen Schooley, Carla Daniels, Jen Skinner and Adrian Buchanan.

I would also like to thank the University of Waterloo writing and communication center, the center for teaching excellence, the center for career action, the graduate office, the international student experience and all others who kindly offered their support to me.

My heartfelt thanks go to my beloved family, I am so fortunate to have you in my life. Mom and dad, I am very grateful for all of your unconditional support, patience, and love. You have always encouraged and challenged me to try to be a better version of myself. I would not be where I am today if it were not for you and your blessing. I would also like to thank my siblings for their encouragement, kindness, and love. Growing up with you has been one of the best things that happened in my life, I love you.

To my loved ones:

Family

and

Friends

Table of Contents

List of Figures

List of tables

1 Introduction

1.1 Overview

In recent decades, the development of additive manufacturing (AM) methods has created extensive opportunities for fabricating parts characterized by complex geometry and formulated from a wide variety of materials. A number of scientific and technological studies have addressed possible applications of this methodology: rapid casting and the manufacture of biomedical and dental prostheses and metallic and synthetic implants. However, current utilization of AM is not limited to these applications, and an AM footprint can be seen in studies that have addressed the shortcomings of conventional methods in other areas, such as the food industry, fashion and art, medicine, construction, aerospace enterprises, and education. Some of the work in these fields has involved employing AM to create functionally graded structures for biomedical and industrial applications.

In medical applications, for example, a combination of an AM process with new fields of study such as regenerative medicine, stem cell research, and tissue engineering has produced promising results for improving health and quality of life. The ability to create parts whose geometry and internal features are complex is assisting researchers with their efforts to enhance the feasibility of mimicking human tissues and organs through bioprinting. Progress in this area could provide the alternative of replacing damaged parts with patient-customized bio-substitutes, which would decrease the demand for organ donors and artificial implants.

In industrial and engineering applications, applying AM methods creates an opportunity for the design and manufacture of parts characterized by external and internal complexity, such as that associated with pore morphology and distribution as well as introducing multiple materials. Controlling these parameters would enable the engineering of samples that have specified values for properties such as stiffness, acoustic and magnetic wave propagation, permeability, and mechanical strength. Tailoring AM features for the effective development of lightweight structures and composites could have a positive impact on the transportation industry and lead to decreased energy demands and improved environmental conditions.

This research will include the investigation of new approaches to the AM of samples with controllable internal architectures as well as an assessment of the effect of AM process parameters and materials' characteristics on the properties of AM-produced parts.

1.2 Motivation

Functionally graded structures that exhibit a variety of porosity levels or variations in the materials within the structure have a wide range of applications in industry and biomedicine, such as the manufacture of bio-substitutes [1]–[3]. Cellular structures are also addressed in other applications, including in the aerospace and automotive industries and in the manufacture of electromagnetic wave attenuators, filters, sound isolators, catalysts, and energy absorbers [4], [5]. Depending on the application, these structures could include either open or closed-cells [5].

Methods of manufacturing functionally graded structures can be divided into two groups: conventional and AM techniques. Although AM offers more promising solutions [6], it still entails challenges that must be addressed. For example, de-powdering to remove loose powder is one of the obstacles related to powder-bed AM methods. A number of methods for conducting this step are suggested in the literature [2], [7], [8], with limitations on the amount of force required to preserve the integrity of the samples and dimensional resolution of the features [9], [8]. One possibility is to place a sacrificial material on a selected point on each layer, which can then be decomposed during the sintering process [10]. Moreover, structuring the multi-material object has been addressed by applying different methods based on the type of process [11]–[15]. Applying bimodal powders has been suggested as one solution [16]–[20]. However, this method can only benefit from the AM's ability to structure a complex geometry but the sporadic distribution of the reinforcement is similar to that of other conventional methods.

Some fabrication parameters such as layer thickness, roller speed, and functional variation of binder saturation level within structures can also control the porosity of heterogeneous structures through their effect on the compaction force and integrity of parts applied in a powder-based AM process [21], [22]. Although control of these factors is unachievable in commercially available systems, a new design for a multiscale porous 3D printer [10] developed in the AM laboratory at the University of Waterloo, Canada, has overcome barriers to conducting experiments in this area.

1.3 Objectives

Control of the size and distribution of the pores in each layer, the ability to create closed internal channels/voids plus feasibility of introducing multiple materials selectively within the architecture are some essential requirements for the use of AM or other conventional methods with respect to the creation of heterogeneous structures.

In this work, the methods of achieving these goals through the management of second material were reviewed. After evaluating the proposed ideas in the literature, a prototype of a novel design for inserting the material, in form of solid particles, selectively on each layer was proposed. A variety of experiments

was designed in order to explore the impact of altering the effective input parameters of the system on the elements of the output from the system.

Moreover, a hybrid additive manufacturing system integrating two methods of binder jetting and material extrusion was deployed to explore the influence of material compositions, design and manufacturing parameters on developing functionally graded structures with controlled close cell distribution. A similar approach was adapted to investigate the feasibility of additive manufacturing metal matrix composites incorporating a custom developed ceramic resin as a reinforcement periodically arranged within the matrix.

In addition to these components of the research, the effect of a number of the parameters involved in the AM process, such as variations in layer thickness and binder saturation level, were also addressed in order to observe the effect of these factors on the integrity of green parts, cell features, mechanical properties of the final parts. The main objective of the proposed research was to combine the findings of these studies for the creation of a functionally graded structure.

1.4 Outline

This thesis consists of eight chapters. The first chapter is dedicated to the introduction, objective and motivation of the thesis. Chapter two outlines a short literature survey on various methodologies for handling the material to bring a conclusion on the proper design and methodology for inserting multiple materials at the designated place in each layer. The purpose of this chapter is to evaluate possible alternatives for retrofitting the available open source binder jetting system. In addition, the introduction section of chapters 3-7 incorporates a short literature survey attributed to the objectives of the associated chapter.

The third chapter is a journal article published in the Journal of Additive Manufacturing:

- E. Sheydaeian, Z. Fishman, M. Vlasea, and E. Toyserkani, “On the effect of throughout layer thickness variation on properties of additively manufactured cellular titanium structures,” Addit. Manuf., vol. 18, pp. 40–47, 2017.

The fourth chapter is a journal article published in the Journal of Manufacturing Processes:

- Esmat Sheydaeian, Ehsan Toyserkani, “A system for selectively encapsulating porogens inside the layers during additive manufacturing: from conceptual design to the first prototype”, Journal of Manufacturing Processes 26 (2017) pp. 330-338.

The fifth chapter is a journal article published in the Journal of Materials and Design:

- E. Sheydaeian, K. Sarikhani, P. Chen, and E. Toyserkani, “Material process development for the fabrication of heterogeneous titanium structures with selective pore morphology by a hybrid additive manufacturing process,” Mater. Des., pp. 142–150, 2017.

The sixth chapter is a journal article submitted to the International Journal of Advanced Manufacturing Technology:

- E. Sheydaeian and E. Toyserkani, “Additive manufacturing of functionally graded titanium structures with selective closed-cells layout and controlled morphology,” IJAM, pp. 1–18, 2017.

The seventh chapter is a journal article submitted to the Journal of Composite Part B:

- Esmat Sheydaeian, Ehsan Toyserkani, “A new approach for fabrication of titanium-titanium boride periodic composite via hybrid additive manufacturing and pressure-less sintering”, Journal of Composite Part B, 2017.

The conclusions and future works are outlined in chapter eight. Figure 1-1 demonstrates the schematic of the thesis outline categorizing the chapters into four main sections: process, system design, material and characterization of products.

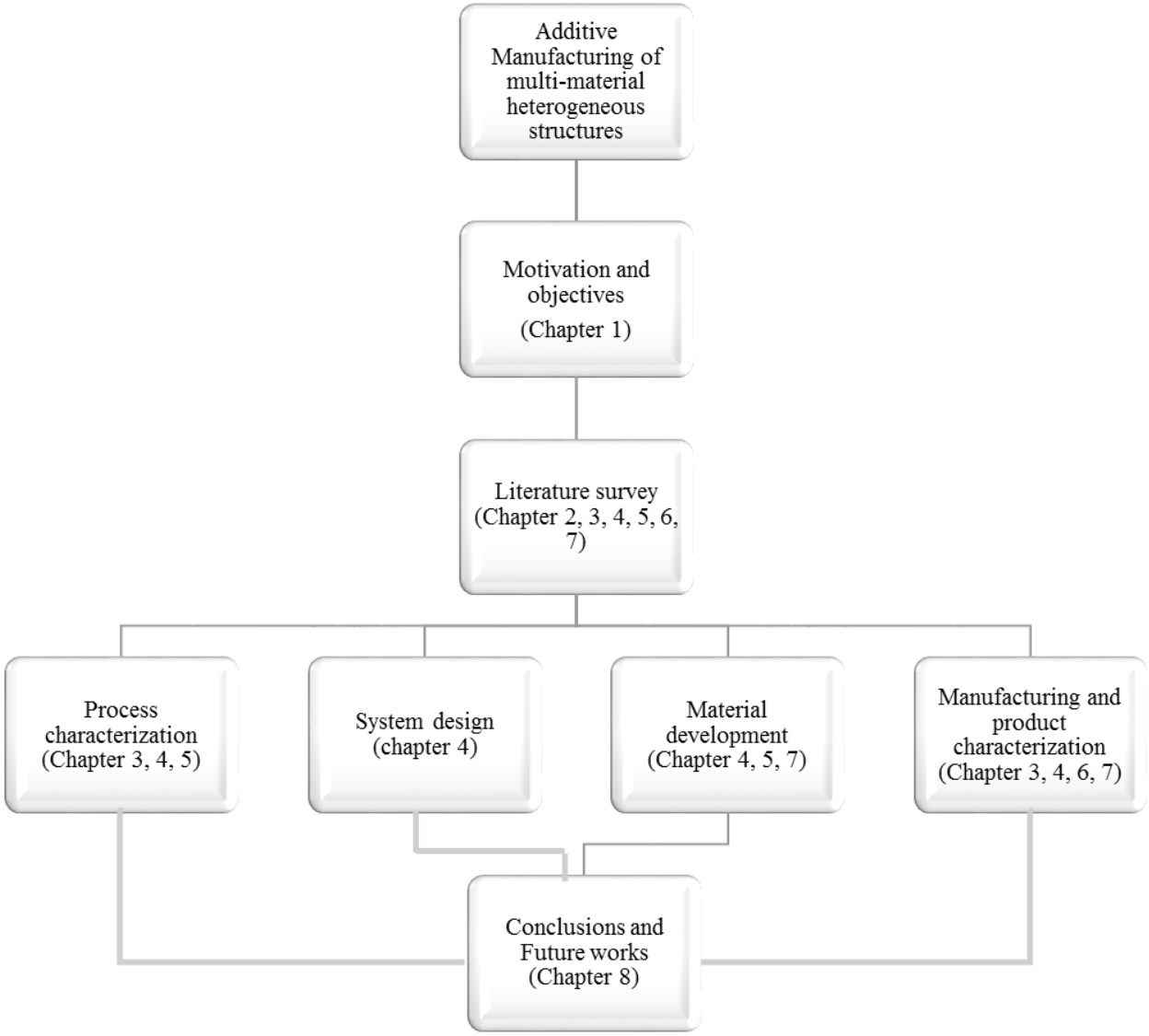

Figure 1-1 The schematic of the research outline

2 Short literature survey[1]

2.1 Introduction

Functionally graded structures with different levels of porosity or variation in materials within the structure have a wide range of the applications in industry and biomedicine. According to the studies with regard to manufacturing bio substitutes such as bio-implants and bioscaffolds, pore size and distribution, as well as pore interconnectivity, are some of the factors with a significant effect on bone tissue in-growth [1]·[2]. In addition, the level of porosity effects on the mechanical properties of the substitute such as mechanical strength and stiffness, allowing the porosity to be adjusted to the similar parameters of tissues. Moreover, the flow of biofluids through the porous media activates the cell growth. All of these properties affect the stability of the implant in the patient body [3]. Cellular structures are addressed in other applications including aerospace, automotive industry, electromagnetic wave attenuators, filters, sound isolations, catalysis, and energy absorber [4], [5]. Depending on the application, the cellular structures may include open or closed cells [5].

Methods for manufacturing the functionally graded structures can be divided into two groups: conventional and additive manufacturing (AM) techniques. Conventional methods include solvent-casting, particulate-leaching, gas foaming, fiber meshes/fiber bonding, phase separation, melt molding, emulsion freeze drying, solution casting and freeze drying [6]. The main drawback of these methods is the uncontrollability of the cell size and distribution in the internal structures. However, AM approaches offer a more promising solution to overcome this problem [6]. AM fabrication techniques create three dimensional (3D) objects from a computer-aided design (CAD) model in a layer-by-layer fashion [6], [23]. Several methods are addressed in the literature under the AM categories. There are seven methods proposed by ASTM standard [24] including:

- Vat polymerization
- Powder-bed fusion
- Material extrusion
- Sheet lamination
- Material jetting
- Direct energy deposition
- Binder jetting

[1] The introduction section of chapter 3 to 7 provides more details associated to the objective of each chapter.

With all benefit in AM, each method has a limitation on the type and shape of the material. In addition, the ability to create the closed-channels, pores and encompassing multiple materials at the selective points on each layer is one of the other constraints.

Moreover, in the case of the powder-bed AM techniques, de-powdering (one of the post-processing steps [25]) is another challenges in this process specifically from small internal features. Binder jetting method is such an example for powder-bed AM which is applied in this study. This method allows the creation of each layer by spreading a thin layer of powder, typically using a roller mechanism, followed by injecting a liquid binder solution according to the 2D image corresponding to the layer slice being printed. The binder acts as an adhesive for the underlying powder to provide the overall 3D green part structural integrity[24],[6]. These steps are repeated in order to complete the 3D object in a layer-by-layer fashion. Different categories of materials including ceramics, metals, and polymers have been proposed as the powder media[26]. According to the literature[27], any kind of flowable powder material could be printable by selecting the proper binder solution and process parameters. The powder material composition can also be tailored to include further adhesive particles or flow enhancers to increase printing quality[28]. After the AM process, a post-processing de-powdering step is necessary to remove the excess powder around the part or within the designed cavities[25]. For ceramic materials and metallic alloys, this step is typically followed by a heat treatment to thermally disintegrate the binder and to create sinter necks between the main powder constituents[29]–[35]. During the sintering process, the liquid and/or solid binders are typically burned off [36][2].

The de-powdering step is removing the excessive powder particles including the particles around the sample and those trapped in the internal cavities. Different methods for this step are suggested in literature such as applying vibration [2], and air blowing from nozzle [7]. One other method is by filling cavities with a liquid and employing microwave energy to boil the liquid and generate fluid flow for removing the loose powder [8]. However, in the binder jetting method hence the green part is not strong enough there is a limitation on the amount of force applied to the green part [9]. Also, generation of the fluid flow into the cavities for removing the loose particles can affect the holes resolution [8].

One solution for this problem is to place a sacrificial material on a selected point on each layer which can be decomposed in the sintering process [10]. The sacrificial element can also be removed from the structure by applying different methods such as leaching, dissolving, heat treatment and etc. [37]–[42] to create and

[2] This paragraph is copied from the following paper: E. Sheydaeian, M. Vlasea, A. Woo, R. Pilliar, E. Hu, and E. Toyserkani, "Effect of glycerol concentrations on the mechanical properties of additive manufactured porous calcium polyphosphate structures for bone substitute applications," J. Biomed. Mater. Res. Part B Appl. Biomater., pp. 1–6, 2016. The copyright permission is provided in the Letters of Copyright Permission section.

control the porosity in the final part. However, depending on the application, this material can be selected to remain as part of the final structure after manufacturing [43] to create a specific property and architecture complex materials such as composite. The main objective of this study is to explore the feasibility of applying this approach for fabrication of functionally graded titanium and titanium matrix composites.

From the wide range of powder materials proposed in the literature, titanium has been selected in this research. Titanium (Ti) and its alloys are widely applicable due to outstanding properties such as corrosion resistance, relevant high strength per weight ratio, non-magnetic property, and high thermal resistivity [44]–[46]. Such properties have increased their demand in industrial (e.g. aerospace, automotive) [47], [48] as well as biomedical applications, such as load-bearing bone implants with promising biocompatibility [45]. However, in orthopedic practice, the solid Ti is still much stronger than the bone tissue, which suggests the fabrication of functionally graded cellular Ti to meet the similar mechanical/stiffness properties with surrounding tissue and eliminate the stress shielding effect [49]. The average porosity and mechanical properties of the human cancellous bones are as follow: (55-95) % porosity, 0.01 to 2 GPa for Young's modulus as well as 0.4 to100 MPa for yield stress [49], [50].

In next section, first different methods to structure multi-material objects through AM will be presented. Next, different methods to achieve the graded functionality in the structure by introducing the second material will be discussed.

2.2 Additive manufacturing of multi-material structures

Introducing additive manufacturing (AM), which is based on fashioning 3D objects through layer-by-layer construction, has created a promising path towards the fabrication of structures with more complex topology as well as more varied material selection. In recent years, development of commercialized and open-source multi-materials 3D printers has been pushing the boundaries even further. Incorporating the vast range of materials selectively distributed within the architectures has resulted in a variety of designs and novel applications. The areas benefiting from this opportunity include robotic [51], electronics [52], sensor development [53], 4D printing [54], tissue engineering [55], art [56], education [57][58], and composite development [59]. Some of the popular methods proposed to facilitate manufacturing of multi-material as well as composite architecture include material extrusion [11], jet printing [12], stereolithography [13], and ultrasonic consolidations [14][15].

In the powder-bed AM, structuring the multi-material object has been addressed by applying different methods based on the type of process. One way to enhance the structural properties is through applying a bimodal powder containing matrix and reinforcement powder [16]–[20]. However, this approach for the fabrication of metal matrix composites (MMC) can only be benefited from the AM ability to structure a

complex geometry but from controlling the materials layout point of view, it is similar to that offered by other conventional methods. In the binder jetting method, injecting multiple liquid binders [60], in addition to retrofitting a system for selectively encapsulating solid particles [61] of two or more materials or liquid polymeric resin [10], [62], have been suggested.

2.3 Methods for incorporating multi-material selectively in powder bed AM techniques

Control of the pore size and distribution in each layer and ability to create the closed internal channel and periodic structures are some of the important requirements in AM or other conventional methods to create heterogeneous structures. Different possibilities were addressed in multi-scale porous 3D printer [10] as a novel design for a binder jetting 3D printer systems to achieve these goals. In this section, each of these methods in addition to some other approaches for particle manipulation will be introduced and advantages and disadvantages of each approach will be discussed.

2.3.1 Vacuum insertion mechanism

One method to create controllable porosity is by inserting solid porogen particles at designated points in each layer. For this purpose, a system with the ability to handle the particles and locating them in the designated place on each layer is required. In [10] and [63], applying the vacuum pressure to pick the particles and release them by positive pressure at the selected positions was proposed.

The effective parameters in this method include picking head parameters such as the size of the holes and surface quality of the head, the amount of vacuum and positive pressure, particle size, environment moisture and effective distance between head and porogen reservoir; were studied and experimented [63]. According to the result of the experiments, one of the main challenges in this approach was the capability of picking a single particle. Since the Van der Waals forces between particles in the reservoir increased the possibility of particles agglomeration. Therefore, a cluster of materials instead of a single particle was picked in each trial. Also, this method was not very well repeatable [63]. Several approaches were suggested to improve the performance: flatting the porogen in the reservoir, making only one layer of the porogen in the reservoir or decreasing the humidity in the system. This technique was suitable for handling the particles in the range of 190 µm to 210 µm.

2.3.2 Electrostatics insertion mechanism

Another solution is to apply an electrostatic force for handling the particles and release them with the air pressure [10]. Application of an electrostatic force for manipulation of small particles is addressed in the literature for either the conductive or non-conductive materials [64]–[66]. Kawamoto [64] conducted the modeling and experiments for manipulation of lunar dust as a weakly conductive material, by applying

electrostatic forces. Applying the voltage difference between the probe and plate created a dielectrophoresis force to pick the particle from the plate. The amount of voltage required for this system depended on the particle diameter. For example, for a particle with a 5 μm diameters, 5 volts and for 20 μ diameters 30 volts was reported in this research.

Another study by Kawamoto and et al. [65] suggested a higher amount of voltage to pick the non-conductive particles (1 to 1.4 K volts) even with a different design of probe. In addition to separating the small particles (less than 200 μm[65]) from the probe, a negative voltage was required to release the particle by creating a corona discharge [64]–[66].

Similar to the vacuum insertion mechanism, picking more than one porogen per trial was one of the problems with this method. In addition, employing a high amount of voltage to pick a particle, especially in the case of the non-conductive material, was another concern. In addition, corona discharge for creating the ionic wind to release the particle from the probe can effect on the arrangement of the powder bed particles and reduce the printing resolution for the applications of this study. For this purpose, employing the air pressure will be the more reasonable solution for this case.

2.3.3 Acoustic levitation

Overcoming to surface forces such as surface tension, electrostatics, and van der Waals forces is one of the important concerns in handling the materials in microscale [67]. Therefore, non-contact handling of the materials has been introduced and studied as one of the solutions. Vandaela and et al. [67] introduced the material levitation as one of the solutions for this problem. According to this article, levitation techniques categorize to magnetic, electrostatic, optical, Bernoulli, air cushion and acoustic levitation. Acoustic wave can generate both in gaseous or liquid media which makes it one of the important candidates to conduct the research in this area [67]. Acoustic levitation divided into the standing wave and near-field methods.

Although this method seemed to be more promising, especially in bioapplications [68], there are several concerns that need to be addressed. Particle agglomeration is still a problem in this approach which can effect on the repeatability of the result. In addition, creating the complex shape requires increasing the complexity of the design and control of the systems. Moreover, to prevent the powder-bed particles dislocation, the working distance between the system and the powder-bed will be limited which effects on the porogen particles impact on the powder bed.

2.3.4 Laser-induced forward transfer direct writing

Studies related to laser-induced forward transfer (LIFT) were established first by Bohandy et al. in 1980. This technique is addressed in the literature among direct writing methods [69]. In this approach, a ribbon

including the transparent material which is coated by donor material will be exposed by a laser beam to deposit the donor material on the substrate.

The donor material can be a layer of metal [69], an organic material such as polymers [70], [71], liquid [72] or a solution including a sacrificial agent (MAPLE-DW[3]) [37]. For organic material with UV transparency, a thin layer (sub-micron) of the coating of the material such as titanium on the ribbon is required to act as an absorber [69]. Heat generated by exposing the laser light can evaporate or melt the donor material on the selective point of ribbon and separated from that. The laser beam wavelength (λ) and exposing time (T_e) are two of the important factors in this process.

A series of experiments was conducted to study the feasibility of using this method for the current research. None of the trials, which included different materials and coatings were successful when employing the available laser equipment (λ~1050 μm). Based on these results and the equipment costs, such as UV laser source (suggested in the literature [70], [71]) and condensing system in case it is required, this method was not considered as an option.

2.3.5 Dispensing a sacrificial material

Embedding a sacrificial photopolymer into a 3D printed part is one of the methods used to create internal channels [32], [73]. In this approach, first, a photopolymer is injected onto the designated area of a layer. Then, exposing a UV light solidifies the liquid during the photopolymerization step (Figure 2-1).

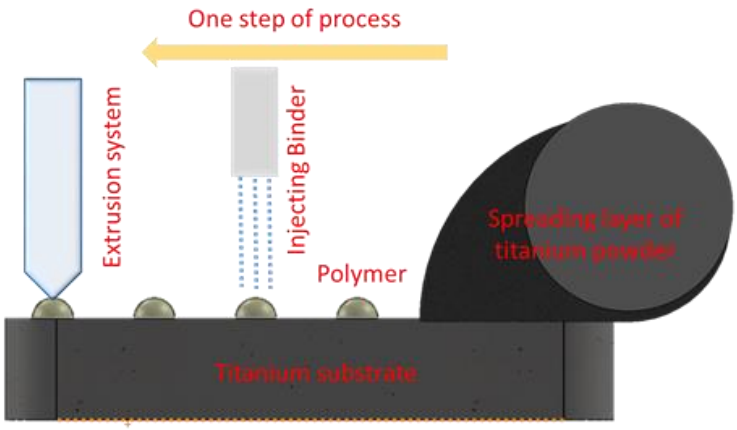

Figure 2-1 Example of one layer manufacturing by incorporating polymer droplets within the layers [74]

[3] Matrix assisted pulsed laser direct write

The penetration of the material into the powder-bed before the photopolymerization step is a challenge for applying this method, as this created deformation in the samples. However, increasing the material viscosity is suggested to improve this method[4].

2.3.6 Summary

In this chapter, different methods of additive manufacturing processes and specifically binder jetting technique were introduced. Since the aim of this research is to explore different approaches and materials to create the functionally graded architecture with utilizing the powder-bed additive manufacturing, different techniques were presented and discussed. According to the presented studies, there are several drawbacks by applying each method including part deformation, poor printing resolution, non-repeatability of the tests and complexity of the design, control and equipment expenses.

To conquer these problems a novel system based on the idea of micro punching was presented and studied[5]. Detail of the system is presented in chapter 4. Also, in chapter 3 effect of combining variable layer thickness on mechanical and structural properties (such as porosity) to create the functionally graded structure is presented. The associated problems in deploying the method suggested in section 2.3.5, is discussed thoroughly in chapter 5 by developing a proper sacrificial polymer. Then, this method was employed in the fabrication of functionally graded structures (chapter 6) and periodic composites (chapter 7).

[4] More detail on this method and properties of the polymer is presented in chapter 5
[5] Chapter 4

3 On the effect of throughout layer thickness variation on properties of additively manufactured cellular titanium structures

3.1 Introduction

Porous cellular structures have become increasingly relevant in different fields of study due to their selectively tailored properties, such as controlled stiffness, thermal conductivity, fluid permeability, acoustic and magnetic properties, impact energy absorption, and electrical isolation, as well as the lightweight design [5], [75], [76]. Controlling the cell size and distribution throughout the structure can demonstrate the variation in each of these properties within the sample and classify it as a functionally graded structure (FGS) [77]. The footprint of FGS configurations can be found in nature, with human bone as one of the well-known examples [78], [49]. The in-depth knowledge of the physiological micro- and macro- structure of bone, in combination with a variety of manufacturing methodologies and tools, has generated promising results in the design and fabrication of bone implants [6].

For bone substitutes or implants, specific manufacturing criteria need to be addressed to successfully implant and stabilize the device in a patient's body [6], [79]. Such criteria include the biocompatibility of the material, bulk, and localized mechanical properties, as well as the design, featuring the anatomy of the bone and its internal structure such as pore morphology. The last factor is essential for allowing body fluid permeation throughout the implants to enhance the bone growth and implant-bone fixation [49], [80]. In addition, porosity directly affects the mechanical properties of bone substitutes and control of this parameter can simulate the appropriate biomechanical response with the surrounding tissue [2], [81].

The development of additive manufacturing (AM) processes [82], (also known as 3D printing), combined with image processing techniques, has created a substantial opportunity for tailoring the design of implants according to each individual patient's anatomy [83]. The binder-jet AM process, one of the AM classes, constructs a 3D object in layer by layer fashion via spreading a thin layer of powder and injecting a binder to provide structural integrity [24]. A heat treatment cycle is often required as a post-processing step to achieve the final product. Several parameters, such as powder size, shape and distribution, binder material and saturation level, layer thickness and sintering protocol have been mentioned in the literature as influential factors on the properties of the samples [33], [84]–[86].

The layer thickness, by affecting the applied compaction force on each layer, can tailor the porosity and mechanical properties of the samples. Several studies have been presented by researchers to evaluate the effect of this parameters via employing different methods of AM [22], [87]–[94]. According to the proposed

results, decreasing the layer thickness, by increasing the compaction force applied on each layer, has a direct effect on enhancing the density and mechanical strength of samples. In these studies, only one layer thickness has been applied throughout the entire part during the manufacturing process. It can be due to the lack of ability to selectively change the layer thickness in real-time and accordingly adapt the slicing of the 3D objects in the commercially available 3D printer software.

The aim of this study is to manufacture functionally graded porous Ti structures by incorporating a variable layer thickness throughout the sample at pre-defined locations via a binder jetting AM process. The 3D printer system in this work has been developed in at the University of Waterloo [Waterloo, Canada], which provides the possibility incorporating different processes parameters as compared to the commercially available binder jetting system. The details of this system specification have been described elsewhere [32]. In this study, four categories of the samples were designed. The first two were AM- made with a single layer thickness throughout to act as a control reference (A and B); and in the second two categories, the layer thickness was varied from high to low to high (150 µm / 80 µm / 150 µm) (C) and from low to high to low (80 µm / 150 µm / 80 µm) (D) in each batch, respectively. Sample C and D were designed with a symmetrical distribution of layer thickness with similar weight ratio (0.5) to investigate the effect of layer thickness arrangement on mechanical properties of the specimens. To select the minimum layer thickness (80 µm), one step calibration was performed to adjust the roller speed to achieve a reasonable print quality by avoiding part distortion and cracking between two consecutive layers while considering the range of the powder particle size. Then the maximum layer thickness was selected approximately two times greater than the minimum (150 µm) to provide the reasonable variation when samples were studied.

A set of analyses were performed to evaluate the relation between the layer thickness and properties of the samples, including a shrinkage analysis, porosity measurement, mechanical strength, stiffness and SEM analysis. In addition, to study the internal distribution of pores based on the layer thickness, the data from a µCT scan of one sample from each group was obtained and analyzed with an image processing method to provide a clear understanding of the internal structure of the samples. The bulk porosity, pore size, and distribution as well as sinter neck size and distribution were obtained using the µCT analysis. In addition, an ANOVA single factor analysis of variance was performed to evaluate the significant differences between the data by using p-value < 0.5[6].

[6] The similar statistical analysis approach was carried out through the other chapters

3.2 Methods, materials, and results

3.2.1 Material preparation[7]

In this study, Titanium (Ti) spherical powder [CP Ti, PhellyMaterials, Ber- genfield, NJ], ASTM (F67-06 Grade 2) was blended homogeneously with polyvinyl alcohol (PVA) [Alfa Aesar, Ward Hill, MA] to prepare the powder for additive manufacturing. A powder blend was produced composed of 97%wt. of Ti with a particle size ranging from 75 to 90 μm and 3% wt. of PVA powder with a particle size < 63 μm. The powder combination was placed on a jar mill [US Stoneware, East Palestine, OH] for four hours to improve the mixture's homogeneity. ZB60 binder [Zb^{TM} 60, 3D Systems, Burlington, MA] was selected as a liquid binder in the printhead [ImTech 610, OR, USA] for the AM process.

3.2.2 Additive manufacturing process

To develop the experiments, four different categories of samples were designed. Each category included 8 cylindrical samples, designed with 5 mm diameter and 8 mm height [SolidWorks Corp., Concord, MA]. A height to diameter ratio of 1.5 to 2, obtained by considering the shrinkage analysis reported by Basalah and et.al [33], was used in the design to meet the ASTM E9—09 standard [95] for the mechanical compression test. Then, each design was divided into the proper number of slices based on the designated layer thicknesses of 80 and 150 μm in netfabb [netfabb GmbH, Germany]. Groups A and B of the samples were sliced with only one layer thickness throughout the part, 80 μm, and 150 μm respectively. Sample C had a stacked layer thickness configuration of 150/80/150 μm, with the 80 μm layer thickness section occupying the middle 4mm section of the part. Similarly, Sample D had a stacked layer thickness configuration of 80/150/80 μm, with the 150 μm layer thickness section occupying the middle 4mm section of the part. Figure 3-1 shows the schematic of process and layer thickness configuration.

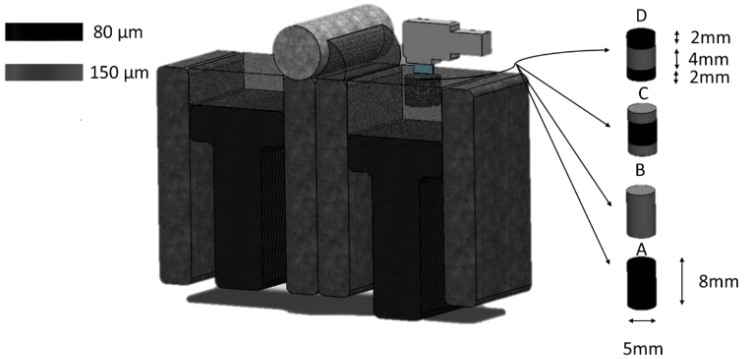

Figure 3-1 Schematic of process and layer thickness configuration in Samples A, B, C and D

[7] The similar powder combination and liquid binder was employed in the binder jetting system in the other chapters

Each batch of samples was 3D printed by employing the binder jet multi-scale 3D printer developed at the University of Waterloo [Waterloo, Canada] [32]. A one-step spread-ability study was performed to select the roller linear and rotational speeds to avoid layer spread defects (Figure 3-2).This step was performed as one of the characterization steps since the custom-designed system is currently in the experimental stage.

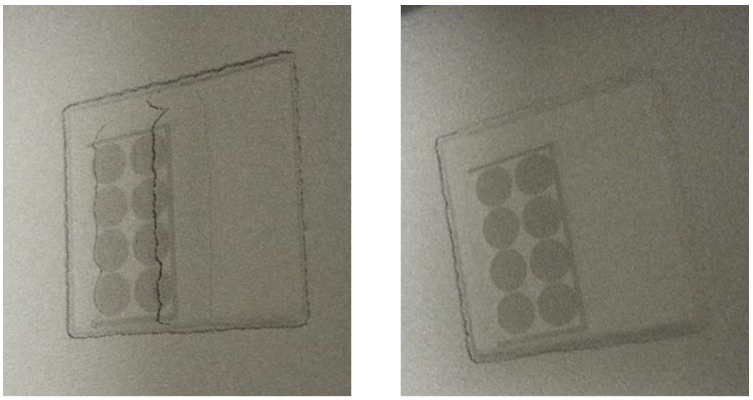

a b

Figure 3-2 Effect of roller speed parameters on the quality of the print. a) shows the crack formation due to the layers displacement and b) shows the quality of the accepted powder spreading

Table 3-1 shows the qualitative relationship between the roller speed parameters and quality of the powder spreading. According to this result, roller linear and rotational velocities were set to 50 mm/sec and 75 RPM to achieve the best quality, particularly for printing with a lower layer thickness (80 µm).

Table 3-1 Correlation between the layer thickness, roller speed and powder spread-ability (X: crack formation. Ok: consistent layer spread)

Layer thickness (µm)	Linear speed(mm/s)	Rotational speed(RPM)	Print quality
20	100	145	X
50	100	145	X
50	50	75	X
80	50	75	Ok
150	50	75	Ok

After the 3D printing process, green samples were collected from the 3D printer, and a de-powdering step was performed to prepare them for sintering in a MTIV high-temperature tube furnace [GSL-1500X-50, Richmond, CA]. Figure 3-3 shows the heat treatment protocol with two main steps including first, de-binding the samples at 295^0C and then the solid-state sintering to remove the PVA residuals and initiate the sinter necks formation between the Ti powder particles up to 1400^0C [33].

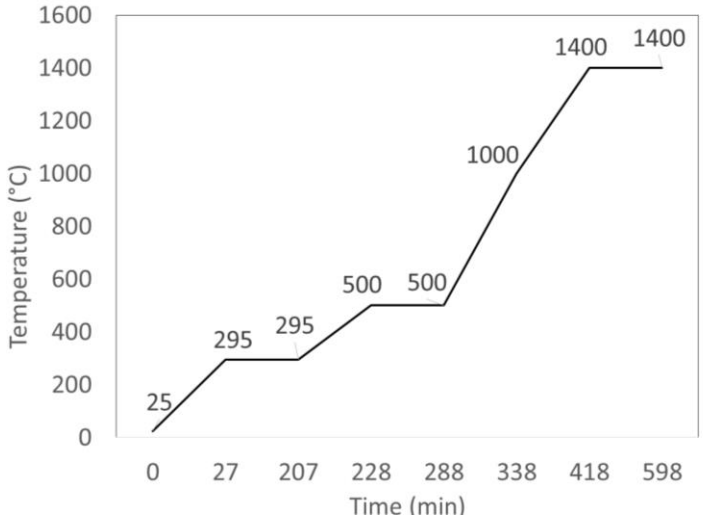

Figure 3-3 Sintering steps for Titanium samples

3.2.3 Shrinkage analysis

To investigate the effect of heat treatment on the dimensional deviation of samples, the height, and diameter of each sample were measured three times with digital caliper [Absolute-Digimatic; Mitutoyo Corp., Kawasaki, Japan] before and after sintering respectively. Then the shrinkage for each geometrical aspect was calculated by applying the following equations and the average of the measurement for each sample [84].

$$Diameter_{Shrinkage} = \frac{D_{Green} - D_{Sintered}}{D_{Green}} \quad \textbf{(3-1)}$$

$$Height_{Shrinkage} = \frac{H_{Green} - H_{Sintered}}{H_{Green}} \quad \textbf{(3-2)}$$

Table 3-2 shows the result of the analysis. ANOVA analysis suggested a significant difference in both height and diameter shrinkage among the categories (p-value<0.05). However, the difference was more notable in comparing group A and B in terms of height shrinkage.

Table 3-2 Average of the dimensional deviation of the samples

Sample	Diameter Shrinkage (%)	Height Shrinkage (%)
A	4.27±2.04	4.56±0.49
B	4.67±1.80	6.08±0.66
C	3.77±0.79	4.27±1.05
D	2.48±1.25	3.67±1.03

3.2.4 **Porosity measurement**

The porosity measurement was performed by applying the Archimedes' principle (ASTM B311 [96]& C373 [97]). First, the samples were cleaned of any residual powder by submerging them into distilled water and placing them in an ultrasonic bath [VWR Ultrasonics Cleaner B2500A-DTH, VWR International, PA, USA] for 5 minutes at 30°C. Then, the specimens were dried in the oven at 130°C for 1.5 hours to be prepared for measuring the dry mass (W_{dry}) with micro precision balance [APX-203; Denver Instrument, Bohemia, NY]. Next, the samples were immersed in distilled water and boiled for three hours. This step was followed by placing them in a universal specific gravity kit [Sartorius YDK01 Density Determination Kit, Sartorius AG, Goettingen, Germany] to measure the submerged mass (W_{sub}), and then the wet mass (W_{et}) after removing them from the setup. The porosity was calculated by using the following formula [33].

$$P_{apprent} = \left(\frac{W_{wet} - W_{dry}}{W_{wet} - W_{sub}}\right) \quad \textbf{(3-3)}$$

The results are summarized in Figure 3-4. The lowest and the highest porosity were observed in group A (30±1)% and group D (34±1)%, respectively. The ANOVA single factor analysis showed a significant variation in porosity (p-value<0.05) between all batches. However, by comparing the porosity of the samples with uniform layer thickness distribution (A and B), the difference was more remarkable.

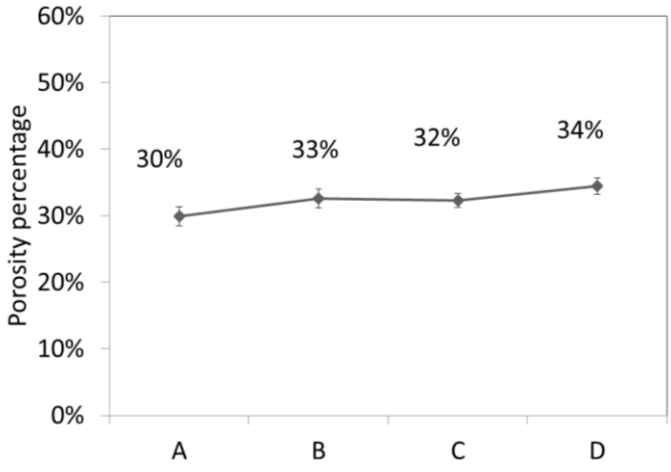

Figure 3-4 Bulk porosity of the Samples A, B, C. D after thermal heat treatment

3.2.5 **Mechanical compression test**

The population of (n=7) samples from each category in Figure 3-1 was subjected to a compression test. The test equipment (Instron-4206, USA) was set up for 1KN load cell with a loading rate of 1mm/min. Data for the force and displacement recorded by this system were used in equation 4 and 5 to define the stress (σ) and strain (ε) applied to the samples.

$$\sigma = \left(\frac{F}{A_0}\right) \quad \textbf{(3-4)}$$

$$\varepsilon = \left(\frac{\Delta x}{l_0}\right) \quad \textbf{(3-5)}$$

Based on this data, the stress-strain curve for each sample was generated to determine the Young's modulus (E) and yield stress (0.2% stress). The results are shown in Figure 3-5 and Figure 3-6. The ANOVA analysis did not show any significant differences in the Young's modulus and yield stress (p-value>0.5).

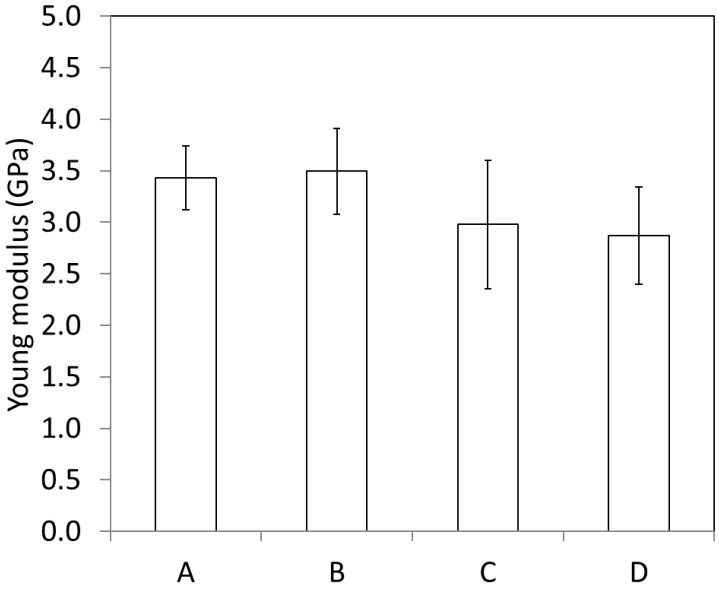

Figure 3-5 The average of the Young's modulus of samples (GPa)

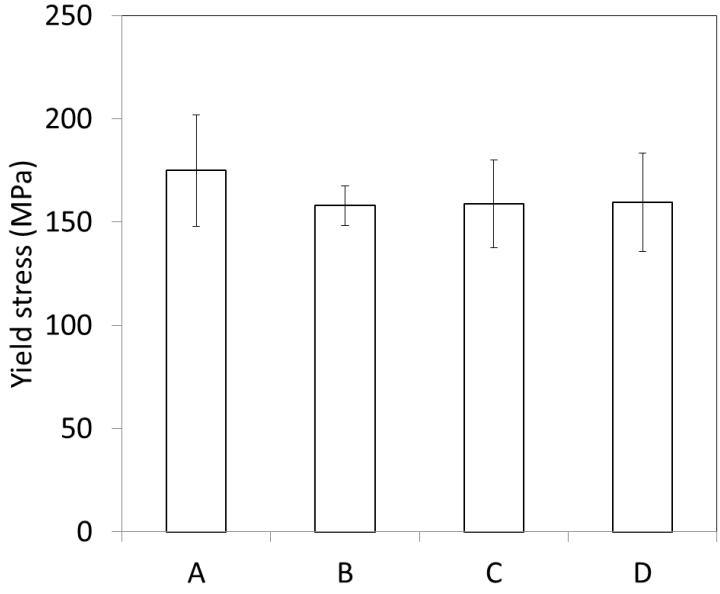

Figure 3-6 The average of the yield stress of samples (MPa)

In addition, to study the correlation between the layer thickness variation and stiffness of the part, Young's modulus of the samples in category C and D was first theoretically calculated with the data obtained from experiments for samples A and B and then compared with the experimental result of the compression test. For this purpose, C and D were assumed to form three sections in which each one printed with the different layer thickness (Figure 3-1). Equivalent Young's modulus (E_{em}) for C and D according to this assumption can be derived from equation 6. The results are presented in Table 3-3 with the highest range of error for category D.

$$E_{em} = \frac{2E_A E_B}{E_A + E_B} \quad \textbf{(3-6)}$$

Table 3-3 The Young's modulus of category C and D from calculation and experimental data

Sample	E measurement (GPa)	E calculation (GPa)	Error (%)
C	2.98	3.46	16
D	2.87	3.46	21

3.2.6 SEM

Scanning Electron Microscopy (SEM) [20 kV SEM; JSM-6460, Jeol, Akishima, Tokyo, Japan] was conducted on one sample from each category. The goal was to observe the size and shape of the sinter necks along the vertical axis and ensure consistency in sintering between batches.

SEM analysis (Figure 3-7) indicated a similar condition in terms of the shape and size of the sinter necks as well as virtually similar distribution of them. The Ti particles retained their spherical shape, indicating that solid state sintering occurred [98], with a similarly sized sinter neck among all four groups of samples.

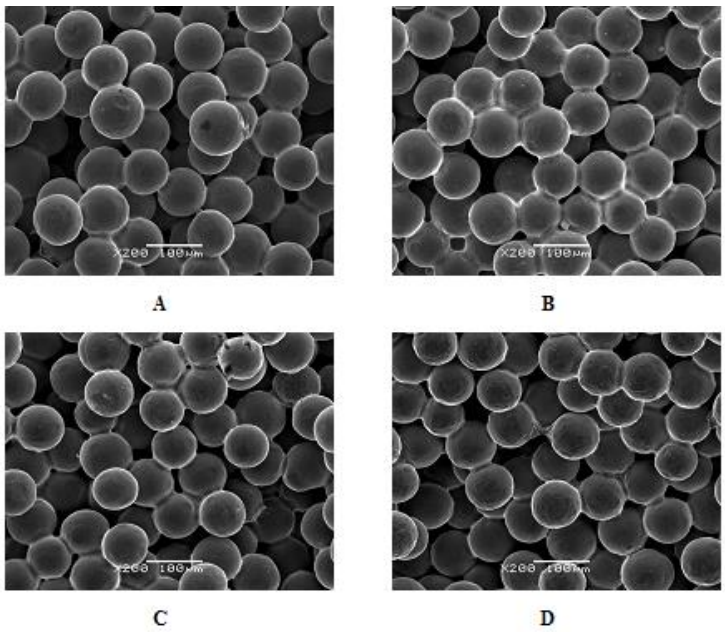

Figure 3-7 SEM results for each category with a magnification of x200 for the middle section of Samples A and B and the top section of C and D.

3.2.7 Micro computerized tomography (µCT scan)

The porous Ti samples were imaged with X-ray micro-computed tomography (µCT), on a SCANCO Medical µCT 100 system [SCANCO Medical AG, Switzerland]. The µCT scan was performed at ~6W (90 kVp, 66 µA) and with a 0.1 mm copper filter. The scan's 3D reconstruction had a spatial resolution of isotropic 6.6 µm/voxel. For each sample, the µCT image data was processed with a custom analysis in Matlab [MATLAB, MathWorks, MA]. The greyscale data were segmented to label the material and the void phases in the porous media. The material phase of the segmented µCT data was then analyzed to characterize the microstructure's pore networks using the methodology developed by Hinebaugh and Bazylak [99].

The average porosity, average pore size, and average sinter neck size as a function of sample height were calculated via image processing of the data from the µCT scan. A representative three-dimensional color rendering of a $1mm^3$ cubic volume extracted from the middle section of Sample C is presented in Figure 3-8.showing the pore size distribution and the particle size distribution.

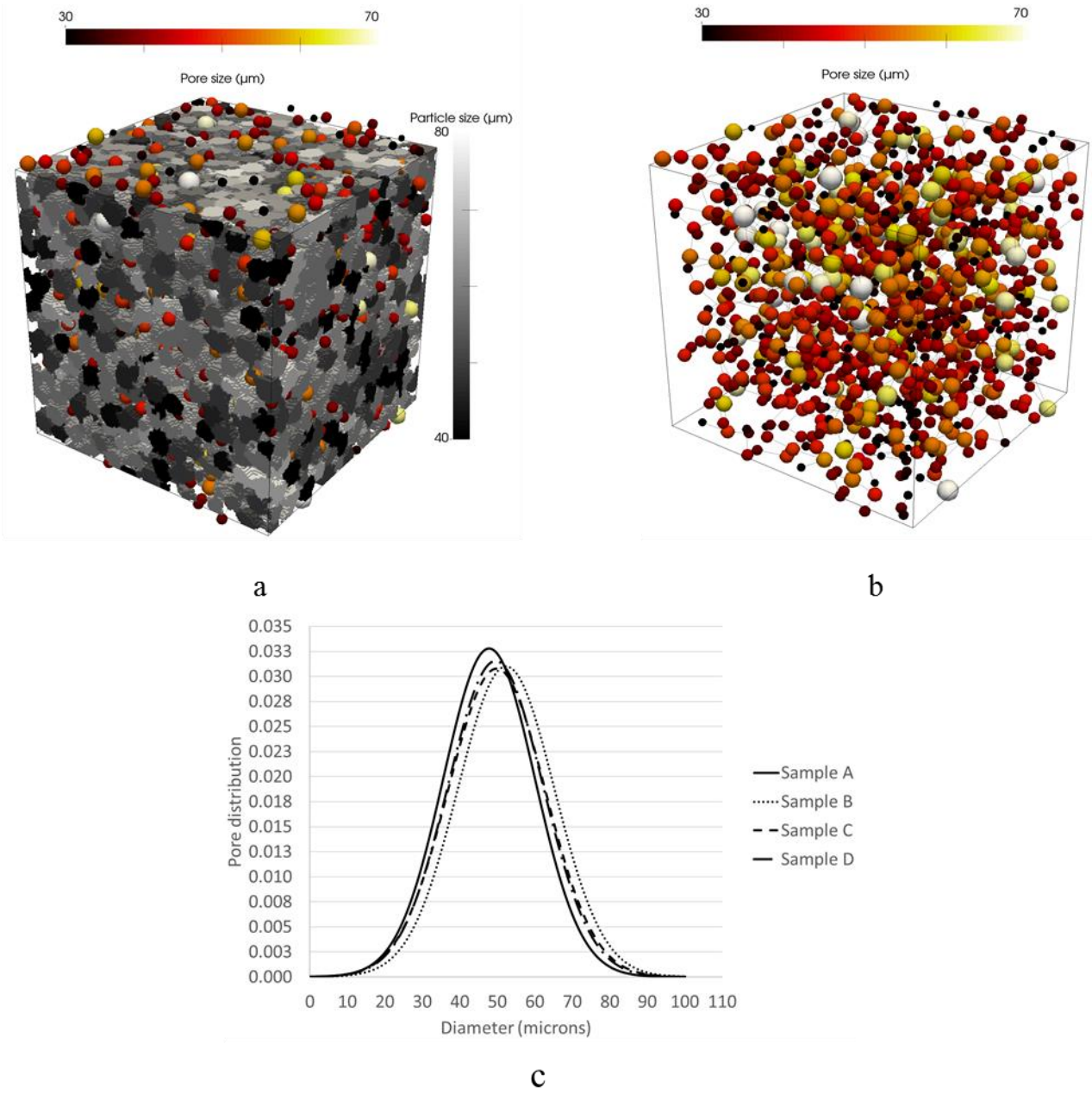

Figure 3-8 Three dimensional rendering of 1mm × 1mm × 1mm subsection of the middle part of Sample C based on the data from the µCT scan. a) shows the solid particles and pores b) demonstrates the pores size and 3D distribution c) shows the normal distribution of pores along the samples

Figure 3-9 shows the average of porosity distribution among samples in respect to their height.

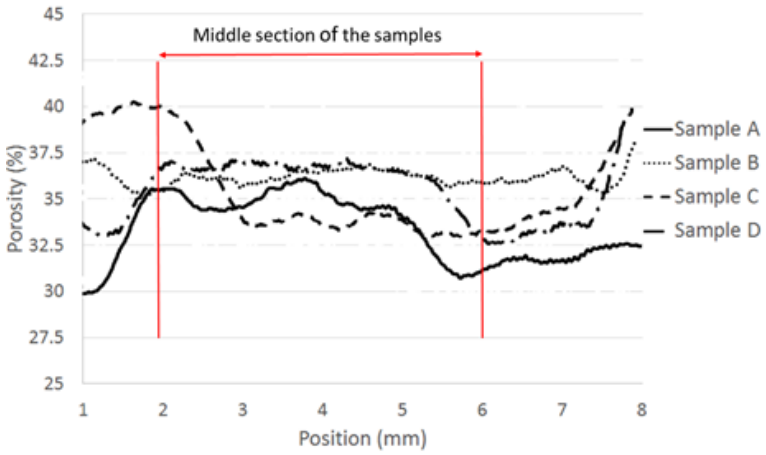

Figure 3-9 Average porosity distribution along samples height

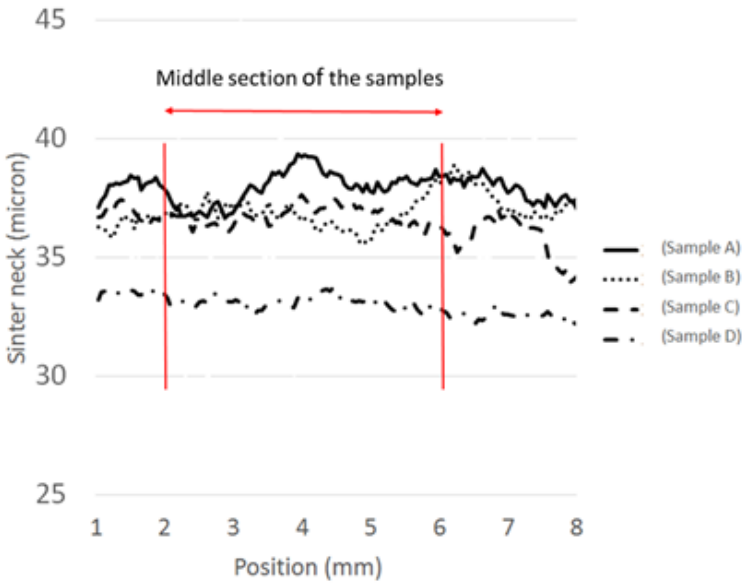

Figure 3-10 Average sinter neck size scattering along the height of the samples

The average bulk porosity throughout the samples in addition to the middle section of samples C and D was calculated and shown in Table 3-4.

Table 3-4 Average bulk porosity of the samples through the height and in the middle section from analyzing the data of µCT scan

Sample	Bulk Porosity (%)	Average porosity in the middle section (%)
A	33.1	NA
B	36.3	NA
C	35.7	34.0
D	35.1	36.0

3.3 Discussion

Four groups of samples with different layer thickness configurations were designed (Figure 3-1) and manufactured from spherical Ti powder by employing a custom binder jet additive manufacturing method. The effect of the roller linear and rotational speed parameters and layer thicknesses on the quality of the powder spread-ability was studied (Table 3-1). The results demonstrated that the roller speed has a significant effect on the layer displacement/crack/scratch formation. This can be attributed to the friction coefficient between the roller and the particles as well as the friction between particles, in addition to the existing Van Der Waal and electrostatic forces and surface energies among the particles and roller [32,33]. Based on these qualitative results, the roller linear and rotational velocities were set to 50 mm/sec and 75 RPM, respectively.

To study the effect of the layer thickness, several analyses were performed on the additive manufactured specimens, including a shrinkage analysis, porosity measurement by applying the Archimedes approach, mechanical compression strength, SEM, and μCT scan imaging combined with image processing.

The shrinkage analysis showed a higher level of dimensional deviation in the height of the samples (3.7±1.0)% to (6.1 ± 0.7)% compared to the diameter (4.7±1.8)% to (1.8±1.7)%, as expected from the previous studies due to the layout of the samples during 3D printing process [84]. An ANOVA single factor analysis of variance indicated a significant difference between the shrinkage sets of data. However, in the case of Group B, which was AM-made with the layer thickness of 150 μm, the shrinkage in height was more observable in comparison to Group A with a layer thickness of 80 μm. This difference in shrinkage could be attributed to having a lower compaction force during green part fabrication with a 150 μm layer thickness, which results in higher green part density[101].

Applying the Archimedes method for measuring the porosity of the samples indicated a range of (30±1)% in Category A to (34±1)% in Category D for this parameter (Figure 3-4). The ANOVA analysis suggested a notable statistical variation in porosity among all categories with a distinguishable difference between the controlled groups, manufactured with uniform layer thickness. Based on the correlation between layer thickness and compaction force, as mentioned elsewhere [21], [101], the parts with the higher compaction force are expected to result in a lower porosity, which is consistent with the results obtained in this study. Porosities of C and D did not reveal any statistically significant difference when compared to each other. The porosity data corroborates the shrinkage data, with the highest shrinkage corresponding to the lowest bulk porosity [33], [84], [102].

From the ANOVA analysis, no significant variations among categories were observed for Young's modulus and yield stress. It can be associated with the small range of the porosity differences (< 5%) [2], [81], and

the large statistical deviation in experimental data. Young's modulus for samples in Group B was slightly higher than others 3.5± 0.4 GPa, and Group A showed the highest value for the yield stress 175±25 MPa, (Figures 3-5 and 3-6) [33]. This trend between A and B could be attributed to their differences in the range of porosity. However, samples C and D with a slightly higher porosity (~2%) obtained from the Archimedes method, did not reveal the same trend compared to the control groups (A and B).

The correlation between the range of the porosity and mechanical properties in this study is comparable with the previous data presented on the fabrication of titanium porous structures [103], [104]. According to our best knowledge, there is no study available in a literature with the corporation of the all parameters suggested in this article. Similar powder size distribution and combination, have been employed in research by Basalah *et. al.* [33] by applying the 120 µm for layer thickness and similar sintering protocol. Comparing our results with this study revealed the same range of porosity and shrinkage in addition to the improvement in mechanical properties of the samples. However, the standard deviation in our work is higher. The improvement in the mechanical properties of the samples can correspond to the roller speed parameters setting suggested in this article.

In addition, when considering using the Ti porous cellular matrix as a bone substitute, there is a good fit between the range of the data for porosity and mechanical strength in this study and the same properties in the human cancellous bones: (55-95) % porosity, 0.01 to 2 GPa for Young's modulus as well as 0.4 to100 MPa for yield stress [49], [50].

In order to investigate the effect of different layer thickness configurations, for AM-made parts, the modulus of elasticity for samples C and D was also estimated by the experimental data extracted from control samples A and B. Equation 6 suggested that the same value of the theoretical Young's modulus for C and D based on the samples configuration is achievable. The experimental data suggested that indeed, the modulus of elasticity for the functionally graded samples C and D are very similar, but they differ from the theoretical value by 16% and 21% error, respectively. From the high range of standard deviations, either the manufacturing process parameters or particle agglomeration can correspond to the range and variation of the errors. Further investigations can be suggested.

Qualitative analysis of the SEM data did not indicate any significant observable differences between the samples with comparable qualitative sinter neck formation as it was reported for the same of powder size distribution and sintering protocol elsewhere [33].

The porosity distribution extracted from the µCT scan data illustrates that the porosity of the C and D samples is between the range of the porosity of the reference groups (A and B) with a decrease in the

porosity in the mid-section of sample C, associated with the layer thickness of 80 µm, and an increase in this parameter in the same region for D as a result of the manufacturing with 150 µm layer thickness (Figure 3-9). This result suggests that tailored porosity is achievable along the layer stacking direction through the deviation of layer thickness during part production. Moreover, the lowest bulk porosity for Category A (33.1%) and the highest for B (36.3%) were obtained from this data (Table 3-4). The bulk porosity obtained from the µCT scan data confirmed that the bulk porosity of the Sample C and D is in between of the results for A and B which is in contrast with the data from the Archimedes approach (Figure 3-4). This variation can be due to the precision difference in applying each of these methods for measuring porosity in addition to the standard deviation resulted from statistical analysis. This measurement can better support the trend of the yield stress and Young's modulus reported in Figure 3-5 and 3-6, respectively and in correlation with the porosity of the specimens. In addition, the highest yield stress in Sample A can be attributed to the highest average size of the sinter neck (Figure 3-10). The average yield stress of each category of samples is corroborated with the sinter neck size data shown Figure 3-10; a higher sinter neck size correlating with better mechanical performance in compression [105].

This study has investigated the effect of the layer thickness configuration on the properties of the functionally graded Titanium structures manufactured with the manufacturing binder jetting method in order to create an orthopedic implant structure. The results suggested that the variation in layer thickness affects the shrinkage and porosity more substantially than the samples mechanical properties, such as the modulus of elasticity and yield stress. Among these groups, the properties of the samples which were 3D printed with one constant layer thickness appeared to be affected more by this parameter than the others, which combined the three regions, each with a different layer of thickness in manufacturing the same samples. The porosity distribution determined from analyzing the µCT-Scan data more clearly revealed the effect of the layer thickness variation in the internal structure of the samples and supported our hypothesis on the microstructural properties of sample C and D compared to the standard groups A and B.

Future studies could focus on the effect of the wider range of particle size and layer thickness with different configurations and incorporate the different roller speeds into the structural and mechanical properties of the AM-made porous matrix to determine the sensitivity of the process to these parameters. In addition, increasing the number of samples in each group can be suggested as one way to increase statistical confidence. Furthermore, based on this paper a DoE will/can be performed to understand the impact of each input parameter on the outcome and optimize properties for a specific application (bone augmentation for instance).

3.4 Conclusion

In this study, four categories of Ti samples with different layer thickness configurations were designed to study the effect of this deviation on the additively manufactured functionally graded titanium structures. Different types of analysis were performed on the samples, including porosity measurement by applying the Archimedes method and analyzing the data from the μCT scan, and mechanical properties measurements, such as Young's modulus and yield stress. Porosity analysis suggested that about 5% difference deviation in porosity is achievable only by changing the layer thickness throughout the part. However, the mechanical properties did not show any significant changes: 2.9 ± 0.5 to 3.5±0.) GPa for Young's modulus and 158±10 to 175±27 MPa for yield stress. These results indicated a success in the manufacturing of porous cellular Ti structures with a customized variation of porosity while obtaining a similar mechanical strength behavior under compression stress.

4 A system for selectively encapsulating porogens inside the layers during additive manufacturing: from conceptual design to the first prototype

4.1 Introduction

Functionally graded structures (FGS) with different levels of porosity or variation in materials within the structure have a wide range of applications. According to studies of manufacturing of bio-substitutetes such as bone implants and bone scaffolds, pore size and distribution, as well as pore interconnectivity, are some of the factors shown to have a significant impact on bone tissue in-growth [1],[2][49]. In addition, level of porosity affects the mechanical properties of the substitute, such as mechanical strength and stiffness, which can be tailored to mimic the tissue properties. All of these properties determine the stability of an implant in a patient's body [3]. Heterogeneous structures would include open or closed cells, depending on the application for which they are designed [5].

Methods for manufacturing FGS can be divided into two groups: conventional and additive manufacturing (AM) techniques. Difficulty in control of the cell size and their distribution is one drawback of conventional methods. On the other hand, AM approaches offer a more promising solution to overcome this problem [6]. AM fabrication techniques create three dimensional (3D) objects from a computer-aided-design (CAD) model in a layer-by-layer fashion [6], [23]. Several methods are addressed in the literature under the AM categories [24].

In powder, bed is methods such as binder jetting [84], one of the challenges is de-powdering [25], specifically from small internal features or encapsulated cavities inside samples. De-powdering refers to the removing excessive powder particles, including the particles surrounding the sample and those trapped inside the internal cavities. A number of methods have been used for de-powdering, such as applying force throughout vibration [2], air pressure [7] and boiling fluid inside the internal channels [8]. However, due to the delicacy of the green samples in binder jet AM, there is a limitation on the amount of force to protect the structural integrity and resolution of the internal features [8], [9].

One solution for this problem is to encapsulate sacrificial porogen particles at selected points of each layer. This step will be followed by removing the porogens throughout different methods such as leaching, dissolving, heat treatment, etc. [37]–[42]. In some applications, porogen material can be left as part of the final structure to provide a specific property [43].

The aim of this study is to present a new methodology for embedding porogen particles inside the binder jet AM-made samples while the particles are in solid phase in each stage. Manufacturing heterogeneous

structures by dispensing a UV sensitive polymer on each layer and by solidifying the material via exposing a UV light source has been under investigation by our group [21].

Different methods of solid micro-particles handling have been studied including the contact [10] [64]–[66], and non-contact based approaches [67] [68], [69],[70], [71], [72],[37]. The main motivations of this chapter for a new methodology are as follows: complexity of the design, control and repeatability of the experimental data caused by the effect of interfacial forces, limited range of the particle size and number, possible powder bed rearrangement throughout the suggested particle releasing method, as well as the overall expenses and spatial limitation on the custom design binder jet AM system [21].

In this work, we propose a novel design based on an idea of separating the porogen particles from a thin sheet of material by a simple punching action. Pure paraffin/wax is selected as the sacrificial porogen in this study. The specific properties of paraffin, such as formability, low melting temperature, low electrical conductivity and high volume expansion during melting, have made it a suitable candidate for a wide range of applications, including indirect AM [106], energy storage [107][108], porogen particles [109][110], etc.

To investigate the feasibility of the proposed concept, first a prototype of the system, called "Porogen Insertion Mechanism (PIM)", was developed and several experiments were designed to study the effect of system inputs on the number, size, shape, and distribution of the porogen particles. After evaluating the results of the characterization step, four categories of the samples were designed and additive manufactured from titanium (Ti) powder through a combination of the binder jet AM method and PIM. The three groups included one layer in which the paraffin porogens were embedded. The last group was studied as a control sample. To ensure the biocompatibility of the selected paraffin products and design a heat treatment protocol, Thermogravimetric analysis (TGA) was performed on the wax materials. After the sintering process, the porosity of Ti samples, by applying the Archimedes method, was measured. The dimensional deviation of the cavities, as a result of porogen removal, was determined by analyzing the SEM data.

4.2 Methods, materials, and results

4.2.1 Design and characterization of the system

The schematic of this method is presented in Figure 4-1. In this approach, first, the porogens are separated from the sheet (ribbon) of sacrificial material by activating a needle. Then, they are pushed into the powder bed to prevent the migration of porogens from the designated location when the new layer of powder is spreading in the next step of 3D printing.

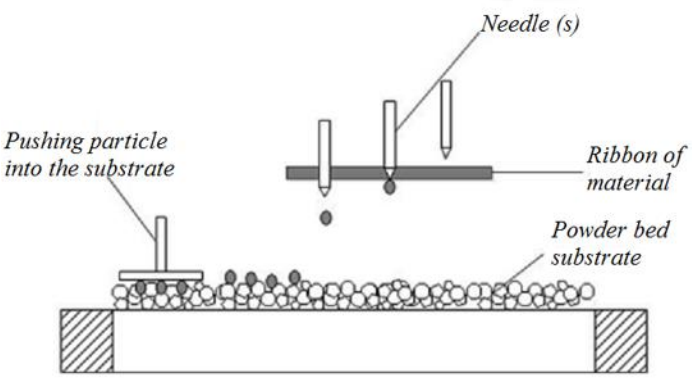

Figure 4-1 Schematic image of inserting porogen at selected points

The porogen insertion mechanism (PIM) system includes three main components: punching and pushing head, a thin sheet (ribbon) of sacrificial material (Figure 4-2-a), and a control board. The punching head includes a linear motion module, which moves the needle(s) over the sheet of sacrificial material, a needle-actuator (solenoid) assembly, and a bracket to push the particles inside the powder bed. The PIM is attached to one of the Z-axises (Figure 4-2-b) of our custom-made binder jet AM system [32], to adjust the working distance with each substrate. Design of the system was completed in SolidWorks [SolidWorks Corp., Concord, MA]. To control the system, an electronics board, including an Arduino board [Arduino Uno, Italy], a motor controller [Easy Driver v4.4, Schmalzhaus], and freewheeling diodes, was designed and assembled. Given the space limitations for mounting the system and available resources for the first prototype, the PIM mechanism was developed to fulfill the minimum requirements for system operation.

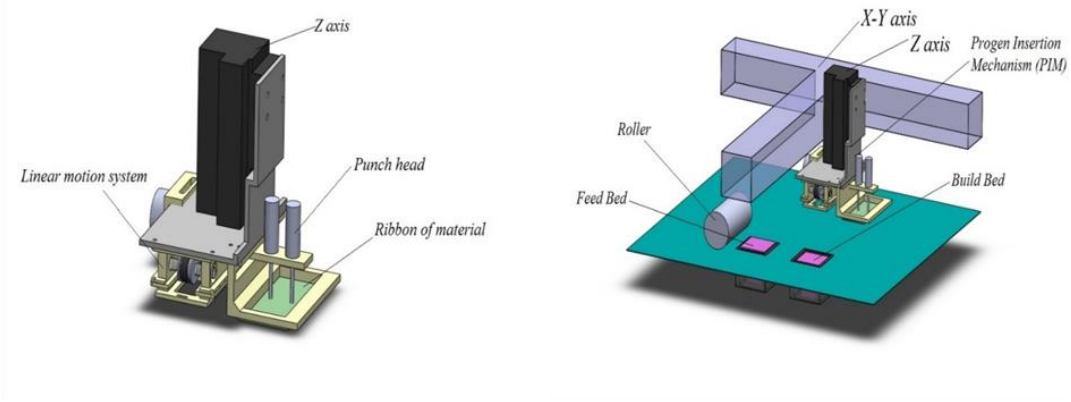

Figure 4-2 The main mechanical components of PIM (a), and assembly of it on the multi-scale porous 3D printer's gantry robot [21]

To build the sheet of sacrificial material, paraffin/wax [Tealights, China] was heated up to 100^0C to liquefy. Then a piece of a mesh was placed inside the melted wax and pressed to result in a layer thickness of 150-

300 µm. Afterward, the wax-mesh combination was immediately placed into the water at room temperature to solidify the material. Since the paraffin material in this study is brittle, the existence of the mesh facilitates the punching process, even in a high impact condition due to the speed of needle-actuator assembly [111]. The first prototype of the integrated system is presented in Figure 4-3.

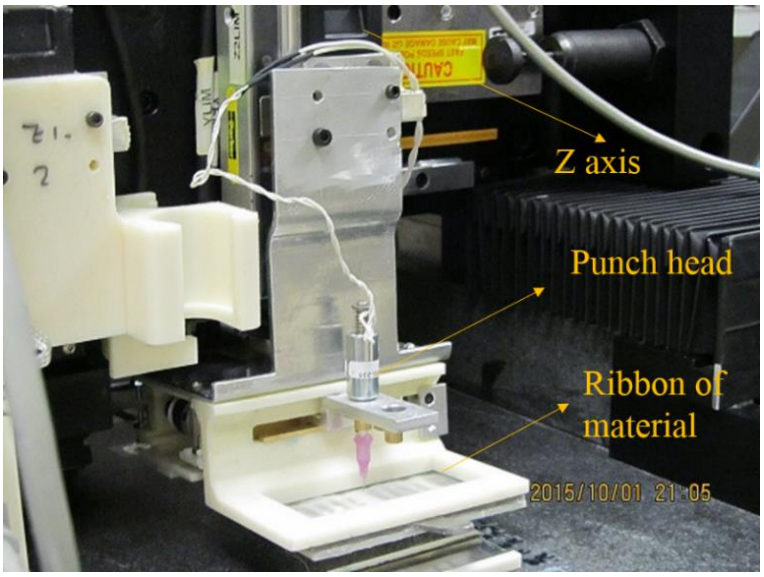

Figure 4-3 Assembly of the design on the Z-axis

To ensure the biocompatibility of selected pure paraffin product, Thermogravimetric analysis (TGA) [TA Instrument, DE, US] was performed. This experiment was designed in two steps. In the first step, performed in an air atmosphere, paraffin particles were heated up to 295^0C with a heating rate of 5^0C/min. Then, the temperature was raised up to 800^0C with the same heating rate. To simulate our titanium sintering protocol [112], this step was performed in the nitrogen environment to eliminate the effect of oxygen on the decomposition of hydrocarbon chains. The result is presented in Figure 4-4.

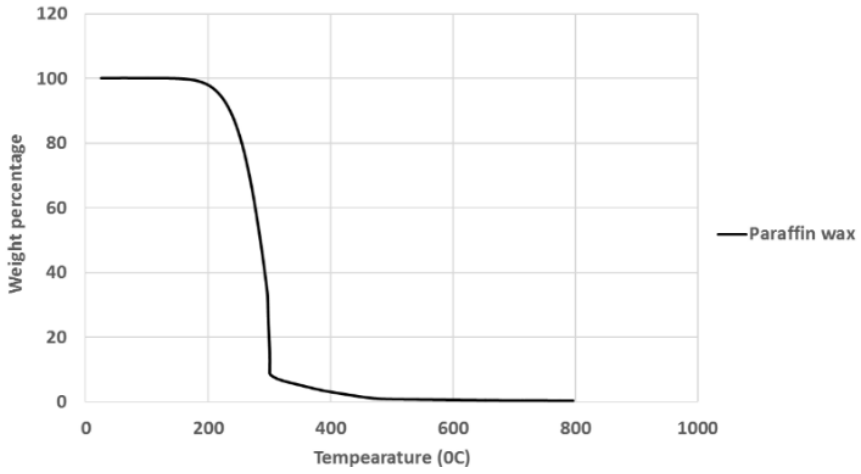

Figure 4-4 Result of the TGA for selected pure paraffin wax

Based on the system capabilities, 15 experiments were designed to gain insight into the PIM performance. The experiments were devised to study the effect of needle diameter (Table 4-1), solenoid voltage, mesh features (Table 4-2 and Figure 4-5), a ribbon of the material thickness and its working distance from the substrate. Table 4-3 details the setup of the experiments. The effect of input parameters was studied on the particle size, shape, number and distributions.

Table 4-1 Needle size

Needle	Diameter (mm)
N-A	0.28
N-B	0.49

Table 4-2 Mesh specifications

Mesh	Average size of meshes (mm)	Average size of fibers(mm)
F-A	0.38±0.05	0.18
F-B	0.51±0.13	0.37
F-C	0.53±0.10	0.07

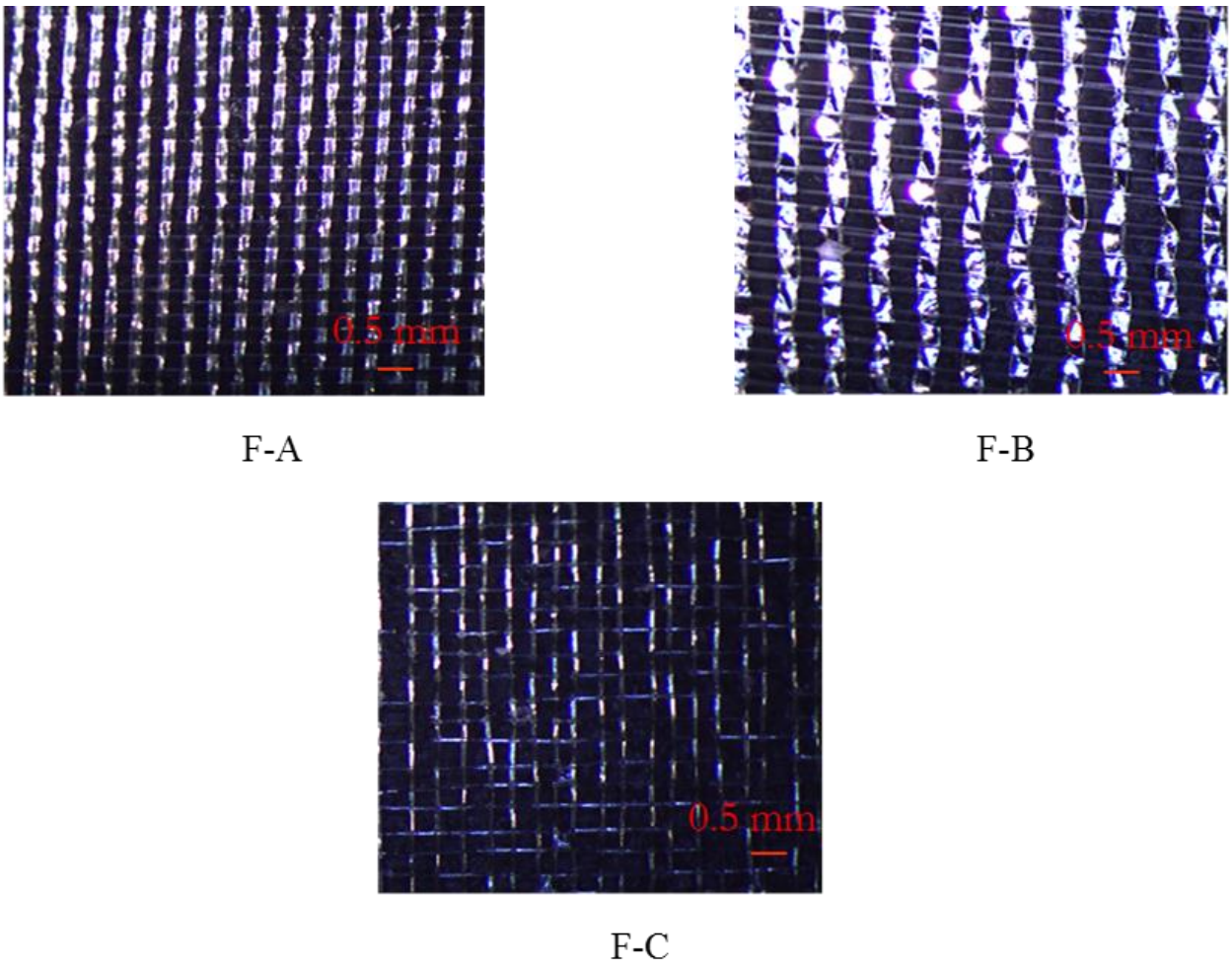

Figure 4-5 The mesh structures

To study the particles' distribution, the distance of separated particles from the center of needles was divided into three zones of Z1 (>2mm), Z2 (<2mm) and Z3 (<1mm). For evaluating the results, particles that landed in Z1 were omitted from the final results and the percentage of the porogens in Z3 in relation to the overall number of the particles in Z2 was determined as a favorable result ("in range"). In addition, the average percentage of the particles in Z1 in correlation to the overall number of the porogens was measured as an "off range" data. This data was used to identify the number of particles which were separated at further locations from the needle impact point on the ribbon.

The effect of the ribbon material thickness on the number of the particles and their locations has been studied (E9, E10, E13, and E14). The particles' distribution was also evaluated when the working distance was varied between the experiments (E10 and E15). In the characterization phase, a microscope slide [Fisherfinest, USA] was used as the substrate. The particle size and its distribution were observed by a

stereo microscope [Leica A60S, Leica Microsystems, ON, Canada], and measured with USB camera viewer software.

In each test, the solenoid was activated 20 times, two times for each location, to enhance the likelihood of releasing at least 10 particles from the ribbon. To ensure the repeatability of the results, each experiment was performed twice.

Table 4-3 Input parameters of the experiments for studying the effect of the system's inputs

Experiment	Fabric	Needle	Voltage (v)	Thickness (mm)	Height (mm)
E1	F-A	N-A	10	0.217	5
E2	F-A	N-A	8	0.217	5
E3	F-A	N-B	8	0.133	5
E4	F-A	N-B	10	0.133	5
E5	F-B	N-A	10	0.297	5
E6	F-B	N-A	8	0.297	5
E7	F-B	N-B	8	0.357	5
E8	F-B	N-B	10	0.357	5
E9	F-C	N-A	10	0.150	5
E10	F-C	N-A	8	0.150	5
E11	F-C	N-B	8	0.123	5
E12	F-C	N-B	10	0.123	5
E13	F-C	N-A	10	0.305	5
E14	F-C	N-A	8	0.305	5
E15	F-C	N-A	8	0.160	1

The size of porogens was determined by measuring the diameter of each particle under the stereoscope. The shape of all particles was estimated by a square or rectangle, based on observation of the particles under the microscope (Figure 4-6). Figure 4-7 shows the average and standard deviation of results for the different combination of the mesh structure, needle size, and voltage in addition to the effect of the thickness of a sheet of the material. ANOVA analysis demonstrated more significant difference among the data when F-C was used as a mesh. In addition, increasing the size of the needle by using N-B or applying the higher value of the voltage (10 volts) increased the sensitivity of results in comparison to the input variables (p-value<0.05).

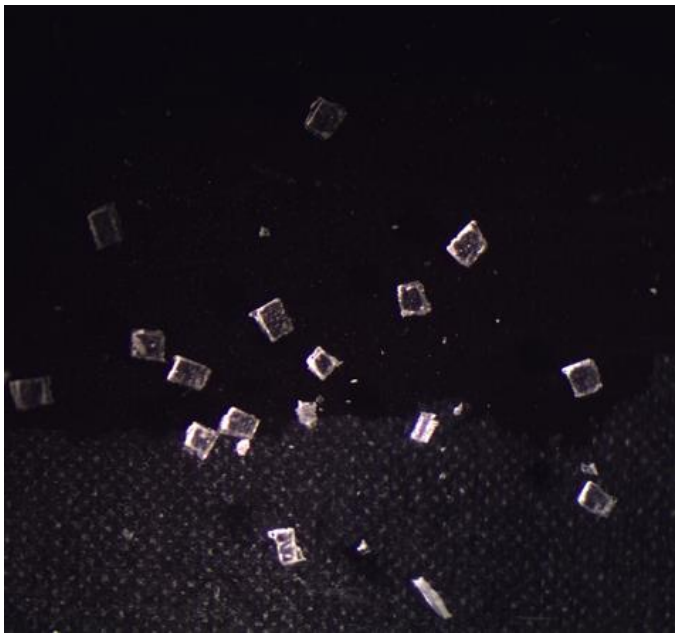

Figure 4-6 Particles shape

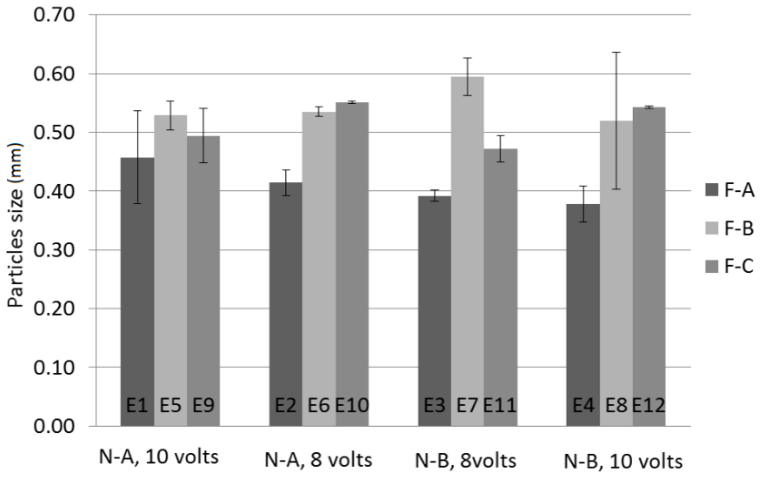

Figure 4-7 The average size of the particles in relation to size of the needle, applied voltage, and type of meshes

Figure 4-8 and Figure 4-9 show the average number of porogens which were separated for each trial. This factor was calculated by dividing the number of separated particles in each test by 10. Then, the average and standard deviations of this value were determined. In experiments performed by N-A, ANOVA analysis showed a significant variation (p-value <0.05) between E1 and E2 (F-A). A similar pattern was observed between different meshes (E3, E7, E11) when the size of needle increased (N-B), while the solenoid was operated with 8 volts. The single factor ANOVA analysis also showed notable differences in the average number of particles between the result from E10 and E14 (8 volts and different thickness).

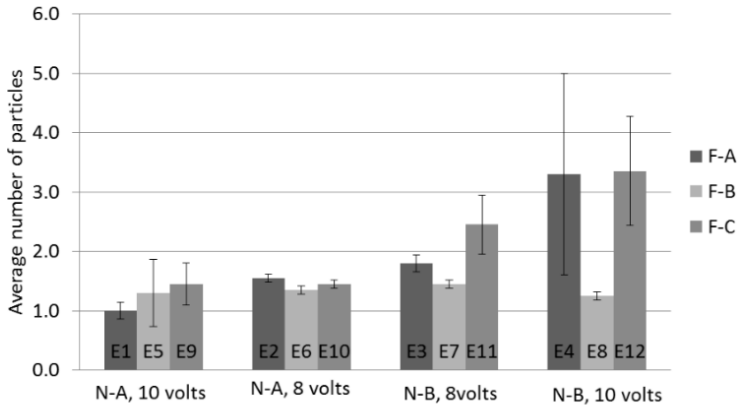

Figure 4-8 The average number of the porogen for each actuation sequence in relation with size of the needle, applied voltage, and type of meshes

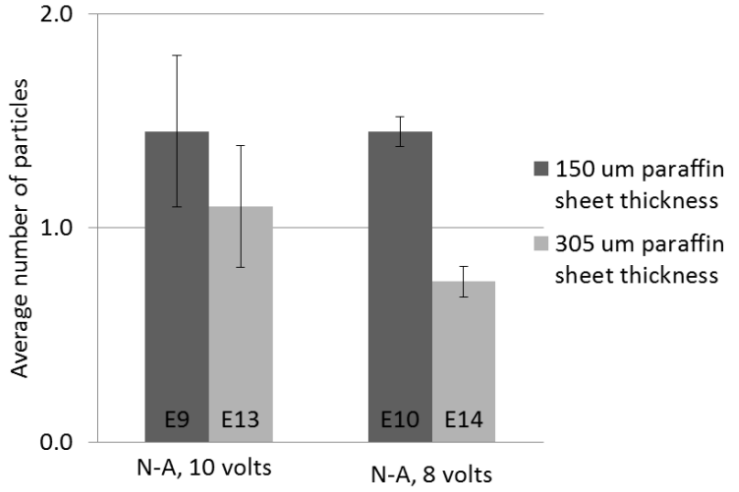

Figure 4-9 The average number of the porogen for each actuation sequence in relation to the applied voltage and thickness of paraffin sheet for F-C

As shown in Figure 4-10 and Figure 4-11, the number of separated particles was different in each experiment. Figure 4-12 and Figure 4-13 show the average and standard deviation for the particles distribution, in experiments E1 to E12, in the "off range" and "in range" zones, respectively. According to the data from the single factor ANOVA analysis, for F-B, the number of "off range" particles was notably different between E6 and E7 ($p<0.05$) when the diameter of the needle increased. In F-C, the difference between outputs by alternating the needle size, as a single factor, or voltage also significantly varied (Figure 4-12). In addition, the range of standard deviation was directly influenced by increasing the size of the needle or voltage value (1% for E2 and E6 to 26% for E1). The same trend was observed by studying the

percentage of particles that were landed ≤ 1mm ("in range") distance from the needle (Figure 4-13). ANOVA single factor analysis did not show any significant differences for this parameter (p-value>0.05).

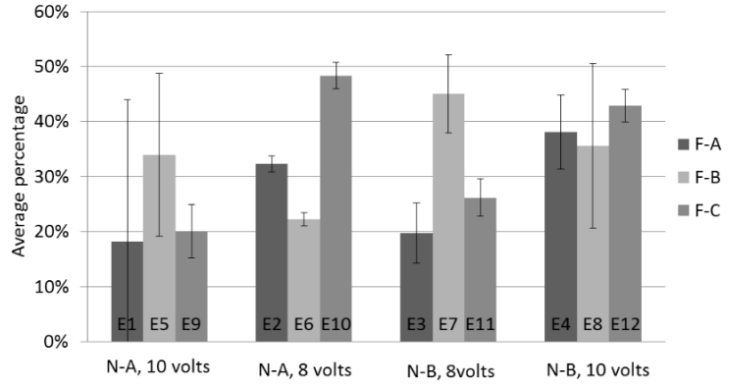

Figure 4-10 The average number of the porogen landed in the off range zone in relation with size of the needle, applied voltage, and type of meshes

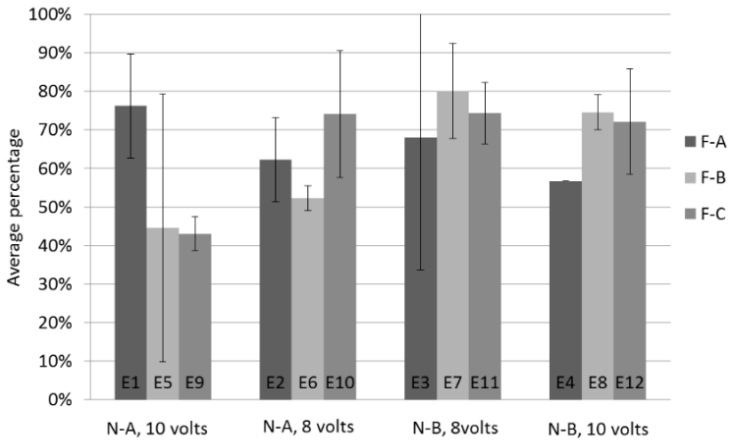

Figure 4-11 The average number of the porogen landed in the in range zone in relation with size of the needle, applied voltage, and type of meshes

Figure 4-12 and Figure 4-13 present the effect of ribbon layer thickness and working distance from the substrate, respectively, on the porogen particles distribution. As shown in Figure 14, increasing the sheet thickness directly affected the range of standard deviation, even when the minimum diameter of the needle (N-A) and voltage value (8 volts) was applied (E14). The variation in the working distance did not reveal any remarkable differences among the data (Figure 15).

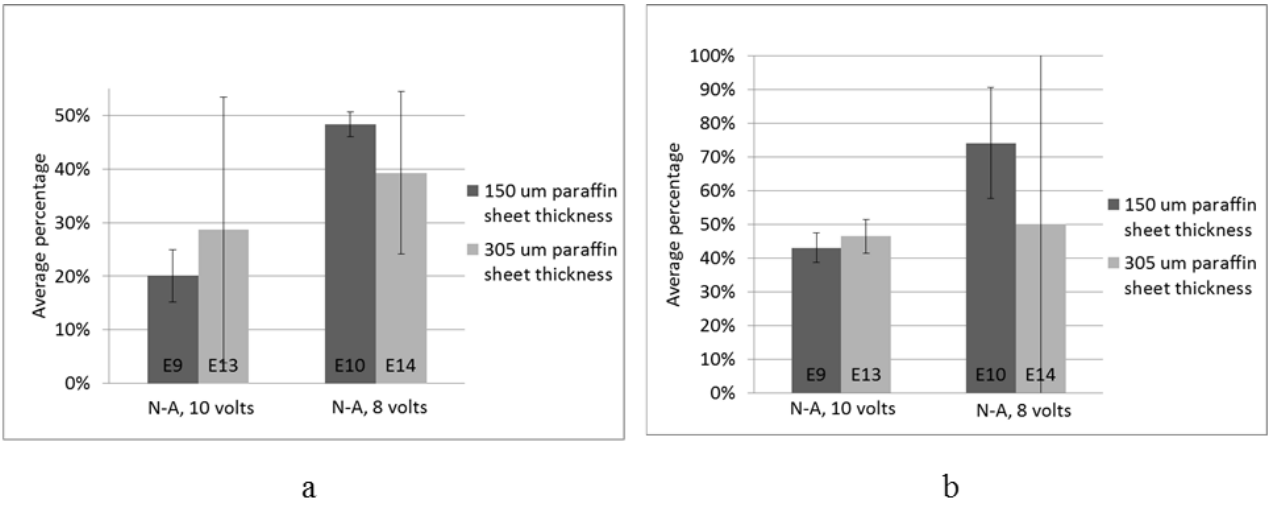

a b

Figure 4-12 Porogens distribution in relation to the applied voltage and different paraffin sheet thickness for F-C

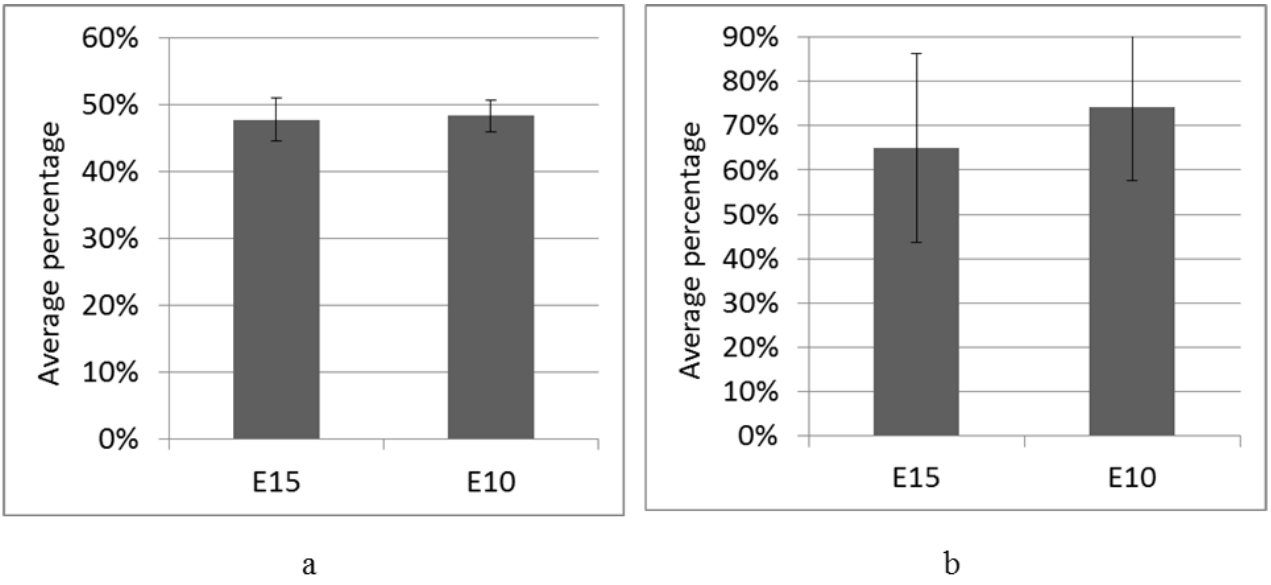

a b

Figure 4-13 Porogens distribution in relation to the working distance between the paraffin sheet and substrate

4.2.2 Additive manufacturing

To study the effect of selectively encapsulating sacrificial porogen during the binder jet AM process, four categories of the samples were designed. Each category included 8 samples of 5mm width, 10 mm length and 2 mm thickness. Each design then was sliced into the 10 number of layers, with a layer thickness of 200 µm, in netfabb [netfabb GmbH, Germany]. Afterward, each group was additive manufactured by employing our custom design binder jet additive manufacturing [112] and Ti powder mixture introduced in chapter 3 (3.2.1).

Samples A, B and C included the porogen on their 8th layers by actuating the solenoid for 18 times (2 per location) and employing three different size of the meshes (F-A, F-B and F-C respectively, Table 2), N-A (Table 1) for the needle and 8 volts of voltage (Figure 6). As a control group, samples in group D were manufactured without embedding wax particles.

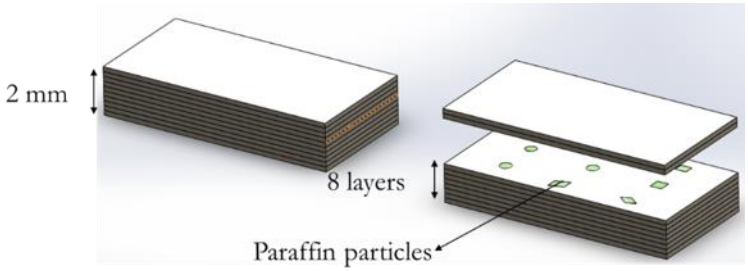

Figure 4-14 Schematic of the AM-made samples structures (A, B and C)

Based on the data from TGA (Figure 3-3), heat treatment steps of the AM-made samples were revised to include four main phases (Figure 3-3). In the first step, the temperature was raised up to 200°C and the samples were left for one hour at this temperature to initialize the decomposition of paraffin particles slowly. This step was added to prevent micro-cracks from forming in the structure due to the high rate of gas generation during wax decomposition. Afterward, the temperature raised up to 295°C in 30 minutes to continue the sintering process as described elsewhere[33].

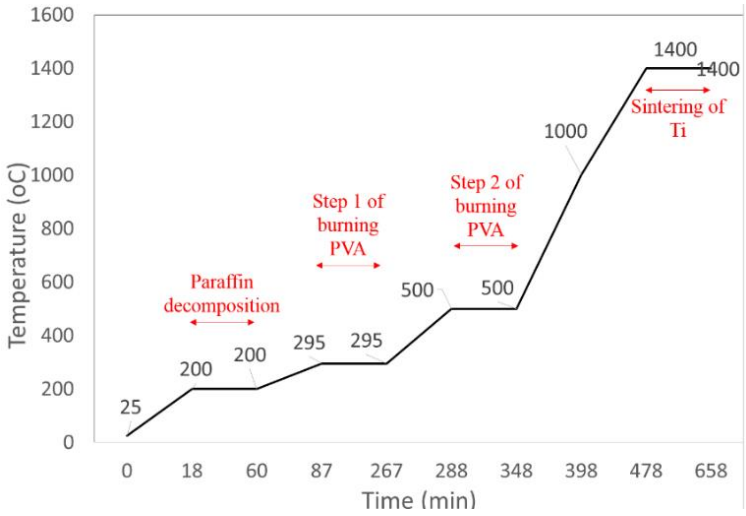

Figure 4-15 Revised heat treatment steps

4.2.3 **Porosity**

The porosity of the AM- made samples was measured by applying the Archimedes method[8] (Figure 4-16). ANOVA analysis of the variance did not suggest any remarkable variation between the samples: (35.5±1)% in D to (37.7±5)% in C.

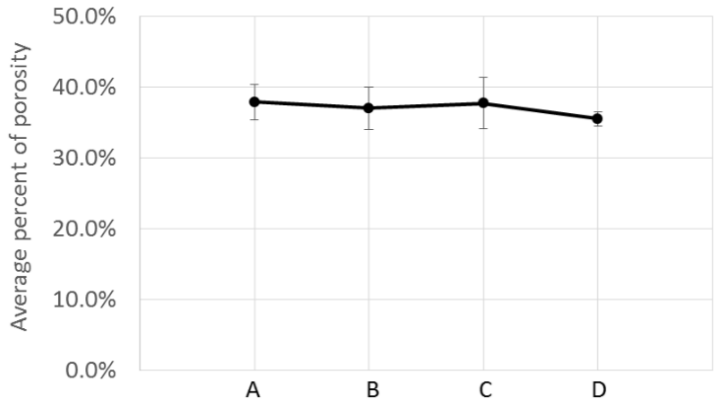

Figure 4-16 Porosity of the Ti samples with embedded porogen

4.2.4 **SEM**

To study the size of pores after removing porogen particles, as a function of porogen size and sintering protocol, a few samples with the same experimental setting as the additively manufactured samples (A, B and C) were created. In these specimens, after embedding porogens and pushing the particles inside the samples, the top surface of the samples was left uncovered. After sintering, the average diameter of the pores corresponding to the removal of paraffin was measured by employing scanning electron microscopy (SEM) [FEI Quanta Feg 250 ESEM, FEI, US] with 10 kv voltage. This data was used to compare the dimensional deviation between the porogen particles size and the size of cavities to investigate the possible shrinkage or expansion throughout paraffin removal.

Figure 4-17 shows the result of SEM for samples A, B and C after removing the porogen during the sintering process. Analyzing the data revealed a similar range for the size of the cavity (Table 4-4) which indicated no shrinkage or expansion as a result of wax elimination.

[8] The experiment steps and related equation have be detailed in chapter 3 (3.2.4)

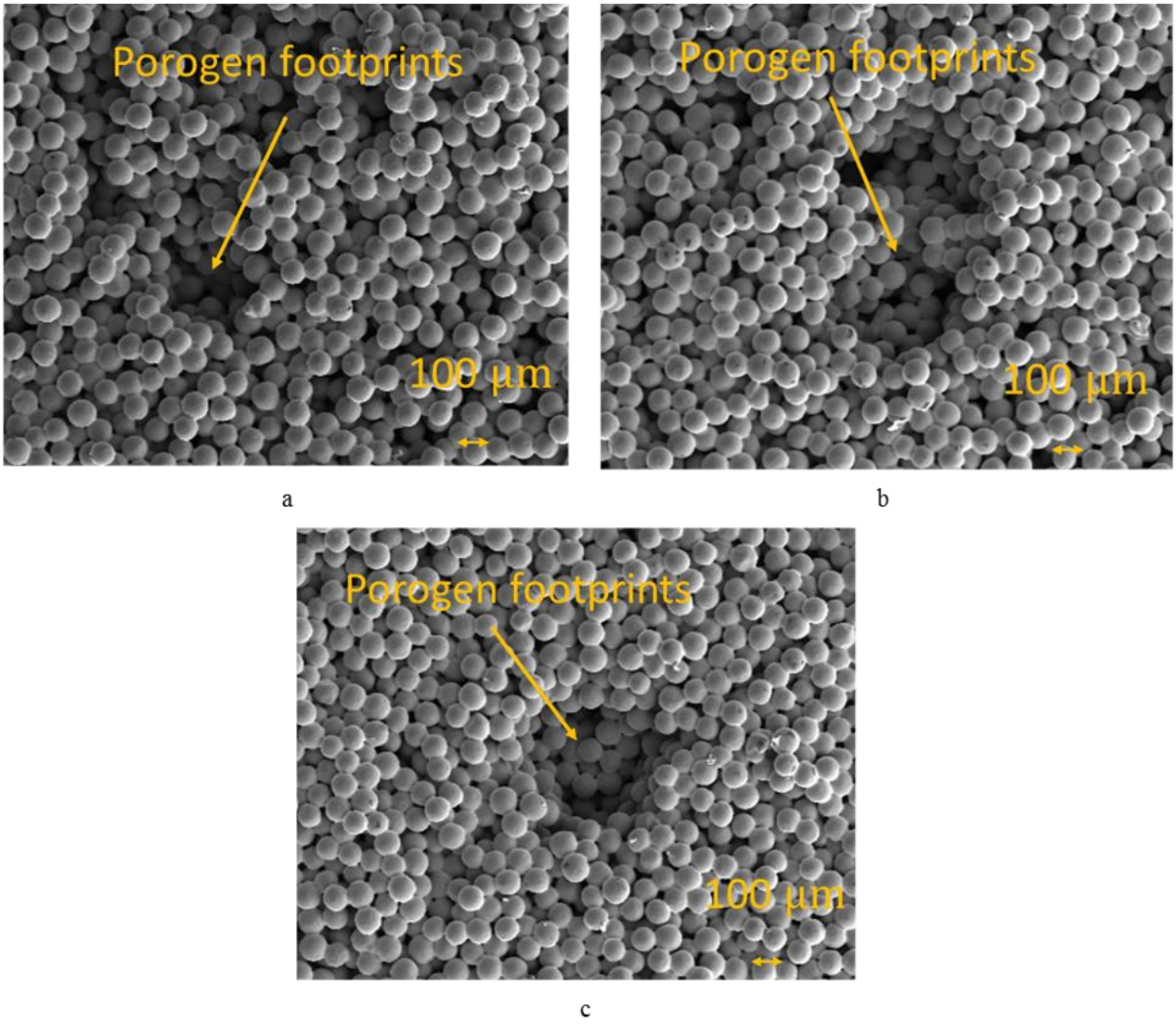

Figure 4-17 Result of the SEM for samples A, B, and C for magnification of x30

Table 4-4 The average size of pores after removing paraffin

Mesh	Average size of pores(mm)	Percent of the dimensional deviation
F-A	0.37±0.10	1%
F-B	0.42±0.09	4%
F-C	0.47±0.09	2%

4.3 **Discussion**

In this article, a system for embedding the sacrificial porogen at selective locations of the AM-made samples was proposed and studied. To analyze the performance of the first prototype of the system, before including in our custom design binder jetting system, 15 experiments were designed. These tests investigated the

effect of system inputs, including mesh size and structure, solenoid voltage, needle diameter, working distance and the ribbon thickness of the sacrificial material. The shape, average size, and number of particles, as well as their distribution on the substrate were determined.

The ranges of porogens' size from each mesh type were achieved as follows: (0.36±0.03) µm-(0.46±0.08) µm, (0.53±0.02) µm-(0.60±0.03) µm and 0.47±0.02 µm-(0.55±0.00) µm, for F-A, F-B, and F-C, respectively (Figure 4-7). This range of the data is comparable with the mesh size presented in Table 4-2. In addition, observation of the shape of particles indicated a close similarity to the morphology of the meshes (Figure 4-5) and porogen particles (Figure 4-6). Therefore, it was concluded that mesh structural properties have a direct influence on the similar properties in particles. Analyzing the data in this step did not reveal any distinguishable evidence for the effect of other test parameters on the porogen particles' morphology. The range of porogen size, which was achieved, is comparable with the human Trabecular Separation (Tb. Sp) in cancellous bones [113], [114], [115].

Based on the results for the number of porogens presented in Figure 4-8, experiments conducted by employing F-B showed the greatest repeatability in results (average standard deviation= 0.2) in comparison to others (average standard deviation= 0.5). This result can be correlated to the size of meshes and fibers. Comparing the result of experiments performed by employing F-B and F-A indicated more robustness in data when F-B was selected. This trend in data can be attributed to the higher diameter of fibers in F-B (0.37 µm) than in F-A (0.18 µm) which can provide better material support by increasing the structural integrity of the meshes although F-B has a bigger mesh size (Table 4-2) [116]. Combination of the effect of these two parameters resulted in the poorest outcome by applying F-C.

According to Figure 4-8, increasing the diameter of the needle, by increasing the applied force to the sheet of material [117], has a direct effect on the average number of particles and standard deviation, specifically for F-A (3.3±1.7) and F-C (3.4±0.9). The same trend can be observed in the variation of voltage. Figure 4-9 shows that increasing the ribbon thickness can decrease the number of porogens, a finding which is correlated with the increase in the bonding force between the layers of loaded wax.

For particle distribution, the result of experiments revealed that increasing the voltage and diameter of the needle, by generating the excessive force and momentum on the sheet of the material, can increase the possibility of particle separation from the unfavorable locations of the sheet ("off range" area), (Figure 4-10). The high range of standard deviation in each experiment can be attributed to the open loop operation of the system and lack of the visual feedback in the system. This caused difficulty in controlling the exact location of the needle when it was landing on the sheet of the material. For instance, it may be suggested that the impact on the fibers, by transmitting the vibration throughout the ribbon, can enhance the likelihood

of particle separation from any possible crack, formed during the sheet preparation process. However, applying a small value of voltage (8volts) and needle size (N-A) improved the repeatability of data (lowest standard deviation of 0.1).

ANOVA single factor analysis of variance did not suggest any significant differences in the average number of particles landing within the 1mm distance from the needle. However, the data was more repeatable when F-B was employed (52±3)%-(80±12)%, which suggests the influence of mesh structural parameter as mentioned before. In addition, increasing the thickness of loaded wax material in E14 reduced the reliability of the results (Figure 4-12), due to the increase in weight of the loaded material, which exceeded the load-bearing capacity of the meshes.

The variation of the working distance between the ribbon and substrate did not reveal any significant differences in the particle distribution outcome (Figure 4-13). This trend in data can be attributed to the high adhesion force between the wax particles and substrate.

After integrating the PIM system with our binder jet 3D printer, four categories of Ti samples were additive manufactured, three of which included a layer with an embedded porogen. Porosity measurement of the Ti samples did not reveal any significant differences among the data (Figure 4-16). This trend is mostly correlated to the limited number of porogen per layer and number of layers with porogen (only one). Therefore, the difference can be detectable only by analyzing the microstructure of the samples by micro computational tomography (μCT) scan [112]. However, the standard deviation of the data in Sample C was higher than others (4%), which corresponded to the low range of the repeatability in the particles separation when F-C was employed.

Analyzing the size of the pores as a result of the porogen removal from Ti structure did not reveal any remarkable differences between the size of particles and produced cavities. This result suggests that the size of pores can be directly controlled by manipulating the size of the sacrificial porogen.

Analyzing the data from this study revealed the direct influence of the mesh structural properties on the porogen particles' morphology. Therefore tailoring the mesh design based on the application is suggested for future investigations. In addition, increasing the diameter of the fiber indicated the higher robustness in the result for particle distribution on the substrate. Thus, the proposed system is capable of carrying a wide range of materials, including the microparticles, therapeutic agents and so on to create functionally graded structures with variable properties. Depending on the application and type of the substances, this material can be loaded on paraffin or directly onto the meshes. From the system design point of view, for the next generation of the PIM, increasing the number of the needles and online coating of the meshes with the

material is suggested to improve the process speed and allow for embedding a higher number of the porogen per each layer during the AM process. In addition, including the vision feedback control to the system is suggested to manage the exact landing position of the needle on the ribbon of material to enhance the controllability of the location of the particle. The PIM system can also be applied as a stand-alone module for any further applications which require the microparticle size handling or micro sampling of brittle materials [118].

4.4 Conclusion

In this article, a novel system and methodology were proposed to embed sacrificial porogen materials on each layer during the binder-jet AM process. First, several experiments were conducted to investigate the effect of input parameters of the first prototype of systems. Analyzing the data suggested that employing the smaller size of the needle (0.28 mm diameter) and applying the lower amount of voltage (8 volts), as well as employing a mesh with better structural properties (F-B) can enhance the repeatability of the results. The results of experiments revealed a direct influence of the mesh size and shapes on the similar features of particles (0.36±0.03)µm-(0.55±0.00) µm.

In the next step, four categories of the samples were additive manufactured to study the effect of encapsulating paraffin particles inside the titanium samples. Porosity measurement by applying the Archimedes method did not suggest any significant differences (35.5±1)% - (37.7±5)% among the samples, which correlates to the limitation in sensitivity of the applied equipment and method for distinguishing the microporosity. In addition, dimensional deviation analysis of the pores after removing porogens indicated a close similarity between the pore size and porogen dimension.

The proposed system and methodology has the potential to be combined with other AM methods or employed as a stand-alone system for different purposes such as micro sampling of brittle materials.

5 Material process development for the fabrication of heterogeneous titanium structures with selective pore morphology by a hybrid additive manufacturing process

5.1 Introduction

The study of natural cellular solids has been a tremendous source of inspiration for structural design in science and technology with some of the applications including the aerospace and automotive industries as well as the field of biomedical [4], [5]. In the design and production step, the integration of close and open cells accompanied with controlled cell morphology provide essential criteria for determining the properties of cellular solid structures [4], [119]. Among different methods, additive manufacturing (AM) has generated a remarkable interest in the fabrication of functionally graded structures due to the feasibility of tailoring product properties through incorporating complex design and topology as well as multiple materials [120], [121].

Incorporating the closed-cells as one way to define the mechanical strength and porosity has been recognized as one of the challenges, particularly in powder bed AM processes such as binder jetting, with respect to the de-powdering step [61]. Different methods have been studied to address this shortcoming in the material selection and preparation step, the control of process parameters and post-processing steps. Some of the examples include applying bimodal powder [122], variable binder saturation level [22], layer thickness [112], and heat treatment [123] which is one of the common post-processing steps for binder jetting method. However, due to the difficulty related to control of pore sizes and distributions of close cells in any of these techniques, the final structure demonstrates a stochastic spread of these parameters.

As one way to overcome the issue, integrating an extra module in the binder jetting system to enable encapsulating a sacrificial material (porogen) at selected locations of the specimen has been proposed and studied by our group [61], [73]. The sacrificial substance can be either a solid particle or a liquid polymer which will be solidified later. This material will be removed from the main structure in the post-processing step (e.g. heat treatment [61]). The focus of this article is in the second method, which includes a hybrid AM system integrating binder jetting of the main material and material extrusion of a sacrificial polymer. The system was first proposed by Vlasea and et.al [10], [32] to structure samples out of the calcium polyphosphate (CPP) powder particles with embedded polymer micro tracks. Next, in the heat treatment steps proposed for sintering of CPP [34], polymer tracks decomposed and resulted in the formation of microchannels.

In addition to its thermal decomposition behavior, the polymer must demonstrate some essential criteria to be applied in the process, from dispensing step to the interaction with powder substrate. To dispense the polymer successfully throughout the nozzle, the liquid must perform the shear thinning behavior while the rheology is being measured [124]. Different studies have addressed the analytical [125] as well as numerical analysis [126] to predict the morphology of the droplets in dispensing via applying different actuation methods. As presented in these works, the geometrical features of the droplets are a function of different parameters correlated to material properties (viscosity and interfacial features), design aspects of the system such as needle size and dispensing distance, as well as dispensing method [127]–[129]. Another critical factor in the shape of the liquid track is roughness of the substrate, which is particularly important on the micro scale (our study) and sub-microns [130].

The viscosity of the polymers can be tailored through molecular weight as well as adding a second component to the mixture [131]. In addition, the polymer composition influences other physical properties such as interfacial forces [132] which are effective in both the dispensing step and the quality of the final structure. Based on our preliminary studies, controlling of the polymer composition can eliminate the rate of failure in the green parts by protecting them from cracking or delamination. The interfacial interaction between the polymer and powder substrate directly influences the quality of the AM-made samples through control of liquid permeation inside the porous media. Since most UV curable resins demonstrate some level of shrinkage during polymerization, reduction of surface area between liquid material and powder substrate can decrease the effect of shrinkage stress and maintain the quality of powder surface [133], [134]. Among various proposed models for estimation of the liquid infiltration rate in a porous medium, the Washburn model was selected in this study. This model correlates the rate of infiltration to the liquid viscosity, the liquid surface tension, the contact angle between the liquid and porous media, and the substrate roughness obtained through determination of pores size [135]–[137].

Moreover, to establish a sufficient integrity between a layer of powder with embedded polymer droplets and the next layer (s), a proper level of adhesion is required between solidified polymers track and the liquid binder, injected at each layer to adhere the layers of powder [27]. Thus, the work of adhesion and the contact angle between the cured polymer and liquid binder were determined to estimate the wettability.

The chemical composition of the selected polymer must display a decomposition trend compatible with proposed sintering protocol of the powder in use for the binder jetting system. This ensures the complete removal of embedded polymer pattern without any trace of the residual left in the final product, which is specifically critical if the goal is to introduce it in biological environments and interfaces [61].

In addition to polymer properties and its interaction with both powder substrate and liquid binder, the binder jetting process parameters as well as the design of the samples, control the quality of the final product. Some of these parameters include layer thickness and binder saturation level, with respect to the binder jetting system, as well as polymer tracks design and distribution within the layers and throughout the volume of samples.

In this study, four categories of UV curable materials with variable concentrations were prepared consisting of the elements similar to those proposed previously [73]: ethoxylated (10 bisphenol-A diacrylate) combined with cellulose acetate butyrate [32]. Next, the dispensability of each batch of material as well as their interfacial interaction with porous powder bed, constructed from titanium (Ti) powder, and liquid binder (Zb 60) were determined. A series of experiments were developed to define the correlation between dispensing parameters and materials composition. Moreover, thermogravimetric analysis (TGA), with the heating steps simulating the sintering conditions of titanium [61], was performed to ensure the compatibility of the decomposition behavior of the developed material with our proposed heat treatment protocol [112]. Later, some of the samples were sintered to estimate the possible deviation in the size of formed cavities and micro rearrangement in Ti powder, when the sacrificial material was eliminated.

After selecting the most suitable polymer composition that meets the proposed requirements, several tests were devised to determine the influence of process parameters (layer thickness, binder injection frequency) as well as the design on the quality of Ti green samples. To study the design criteria, a droplet pattern was selected with variation in the number and distribution on each layer as well as the alternating the sequence of the layers with deposited polymer patterns in the titanium AM-made specimens. The success in this step was achieved when no displacement in the layers of Ti was observed.

5.2 Materials, methods, and results

5.2.1 Materials preparation

To study the effect of polymer blend properties, four different categories of material were proposed for the material extrusion system (Table 5-1). All of the compounds include the variable compositions of the bisphenol-A ethoxylated diacrylate (BAE) [Ebecryl 150, Cytec, NJ, USA] and cellulose acetate butyrate (CAB) powder (M_n 12,000) [Sigma-Aldrich, Oakville, Canada]. To enhance the viscosity of monomer (BAE), CAB was diluted in acetone and then added to the monomer. A photoinitiator powder (1 wt.%), Phenylbis (PI) (2,4,6-trimethylbenzoyl) phosphine oxide (Irgacure 819) [Sigma-Aldrich, Oakville, Canada] was added to each batch to improve the UV curability of the mixture and to initiate the polymerization step. The substances were mixed at room temperature for 30 minutes to ensure the homogeneity of the blends [32]. The mixtures then were used in the nozzle deposition system for extrusion.

Table 5-1 Four categories of the polymer blend

Material	BAE (%)	CAB (%)	Acetone (%)
A	56	13	31
B	61	15	23
C	56	20	23
D	61	18	20

A powder, combining titanium (Ti) and polyvinyl alcohol (PVA) was prepared to be employed in the binder jetting AM system. The size, concentration, preparation steps, and properties of the powders have been explained in3.2.1.

5.2.2 Evaluating the sacrificial polymer surficial interaction with the Ti substrate and the Zb60 binder

The primary studies revealed a correlation among the polymer permeation inside the porous Ti substrate, influencing surface area, and the quality of samples which is affected by the shrinkage caused by the polymerization step and solvent (Acetone) evaporation [138][139][140]. Figure 5-1 shows two samples with a similar substrate and liquid dispensing pattern but different polymeric compositions. The warp in the specimen "a"is distinctly observable (Figure 5-1-a).

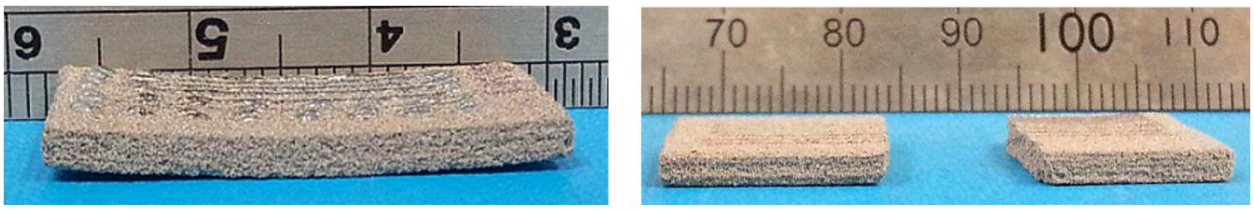

a b

Figure 5-1 Effect of polymer infiltration on the AM-made titanium samples quality. a) shows a delamination in the sample and b) shows an acceptable quality (sample was cut for SEM)

Among various proposed models for estimation of the liquid infiltration rate in a porous medium, the Washburn model was selected in this study. This model correlates the rate of infiltration to the liquid viscosity, the liquid surface tension, the contact angle between the liquid and porous media, and the substrate roughness obtained through determination of pores size [135]–[137]. Based on this model (Equation (5-1)), the square of the liquid permeation depth inside the substrate (x^2) over time (t) is a function of the liquid properties such as viscosity (μ), surface tension (γ), contact angle (θ), and pore radius (r) [141], [142]. In this study, the proportion of (x^2/t) is denoted as an infiltration rate number (IR). The pore radius of 54 μm, similar to what was obtained in our previous work [112], was assumed in the calculation of IR.

$$IR = \frac{x^2}{t} = \frac{\gamma . \cos\theta}{\mu} * r \qquad (5\text{-}1)$$

To measure the viscosity of the material listed in Table 5-1, a high shear viscometer [BROOKFIELD CAP 2000, Brookfield AMETEK, MA, USA] was employed. In each experiment, the rotational speed was increased from the minimum of 80 RPM, due to the system specifications, to a maximum of 600 RPM, and then the shear rate was calculated by the equation provided in the device manual. Due to the remarkable variation in the range of viscosity for materials C and D (Table 5-1), compared to others, two different sizes of the disk were selected to measure the viscosity. Thus, a different range of shear rate was obtained for C and D. Figure 5-2 demonstrates the viscosity of polymer blends. Due to the difference in the range of calculated shear rate, the viscosity of samples C and D are shown in a separate graph (b).

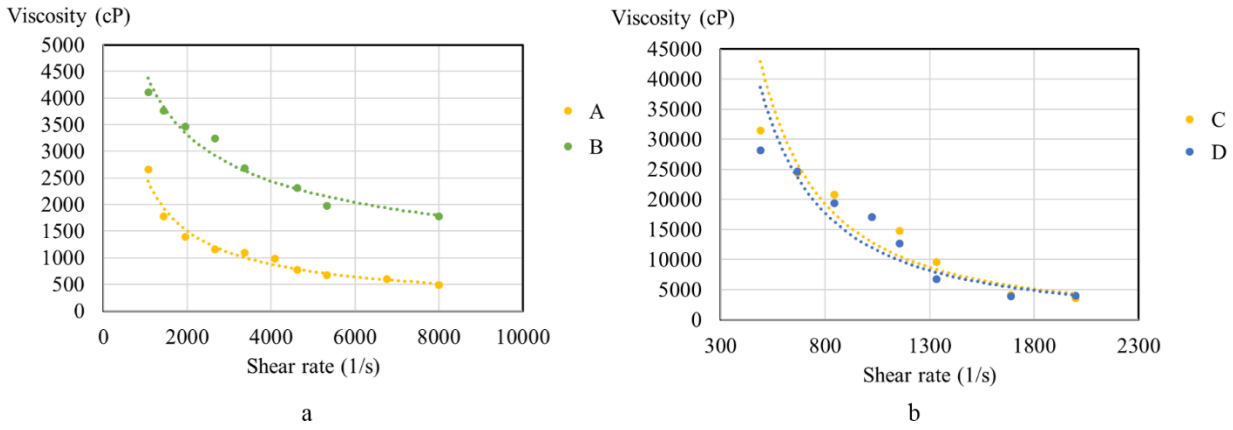

Figure 5-2 Viscosity of the proposed polymeric blends.

To measure the surface tension, the axisymmetric drop shape analysis profile (ADSA-P) technique was used to analyze the data from the pendant drop set-up. The accuracy of this technique first was tested using a drop of pure water [143]. For each measurement, a small amount of liquid was injected using a hanging syringe to form a drop and then images of the drop were captured using a monochromic high-resolution camera. This step was performed on the polymeric blends in addition to the Zb60 liquid binder. The methodology of the measurements and instruments are described elsewhere [144]–[146].

The shape and dimensions of the menisci of the captured images were compared with the theoretical drop profile based on the Laplace equation of capillarity to obtain the interfacial tension of the polymer samples [147], [148]. The contact angle between the polymers and the Ti substrate was measured by creating a small droplet of the polymers on the pre-AM made Ti substrate and analyzing the captured images[9].

[9] In the described steps, the PI powder was omitted from the final composition due to the non-UV protective environment and the small portion of this material in the final combinations.

The average and standard deviations of permeation parameters are presented in Table 5-2. Due to the limitation in the minimum rotational speed of the viscometer, the viscosity in the zero shear rate (or a close approximation) could not be obtained through the experiments. Therefore, to avoid the extrapolation in the viscosity graphs, the viscosity of the materials was approximated at a shear rate of 1000 (1/s) in this table to calculate infiltration rate (IR). As shown in the table, the infiltration rate in material C (0.03 m^2/s) is less than the others.

Table 5-2 Interfacial parameters of the polymer blends and their effect on the infiltration rate

Material	Viscosity, μ (cp)	Surface tension, γ (mJ/mm^2)	Contact angle (θ)	IR number (m^2/s)
A	2656.3	48.5±1.5	96.4±5.6	0.11
B	4114.6	53.5±1.1	117.4±8.0	0.32
C	31397.5	59.0±0.5	108.1±1.1	0.03
D	28131.5	56.5±4.3	120.8±2.7	0.06

The infiltration profile of each polymeric sample was also studied through scanning electron microscopy (SEM) [ULTRA Plus, Zeiss, Germany], with 10 kV voltage. The images were obtained from the AM-made green Ti samples cross-section with a deposited polymer pattern on top. Figure 5-3 illustrates the SEM images of the cross-section of polymer pattern on Ti porous substrates. As shown, the polymers permeation inside the porous media in the case of material C is remarkably lower than the others due to the minimum calculated infiltration rate.

Furthermore, in order to investigate the interaction between the cured polymer and the liquid binder, the work of adhesion between the cured polymer and liquid binder was determined. Thus, each batch of the polymeric material (including PI) was spin coated on a glass surface and then exposed to a UV light source [365 μm, 4 watts, UVP, Edmund optics, NJ, USA] for the polymerization step. Subsequently, the contact angle between ZB60 and coated surface was measured to verify the adhesion between polymers and binder.

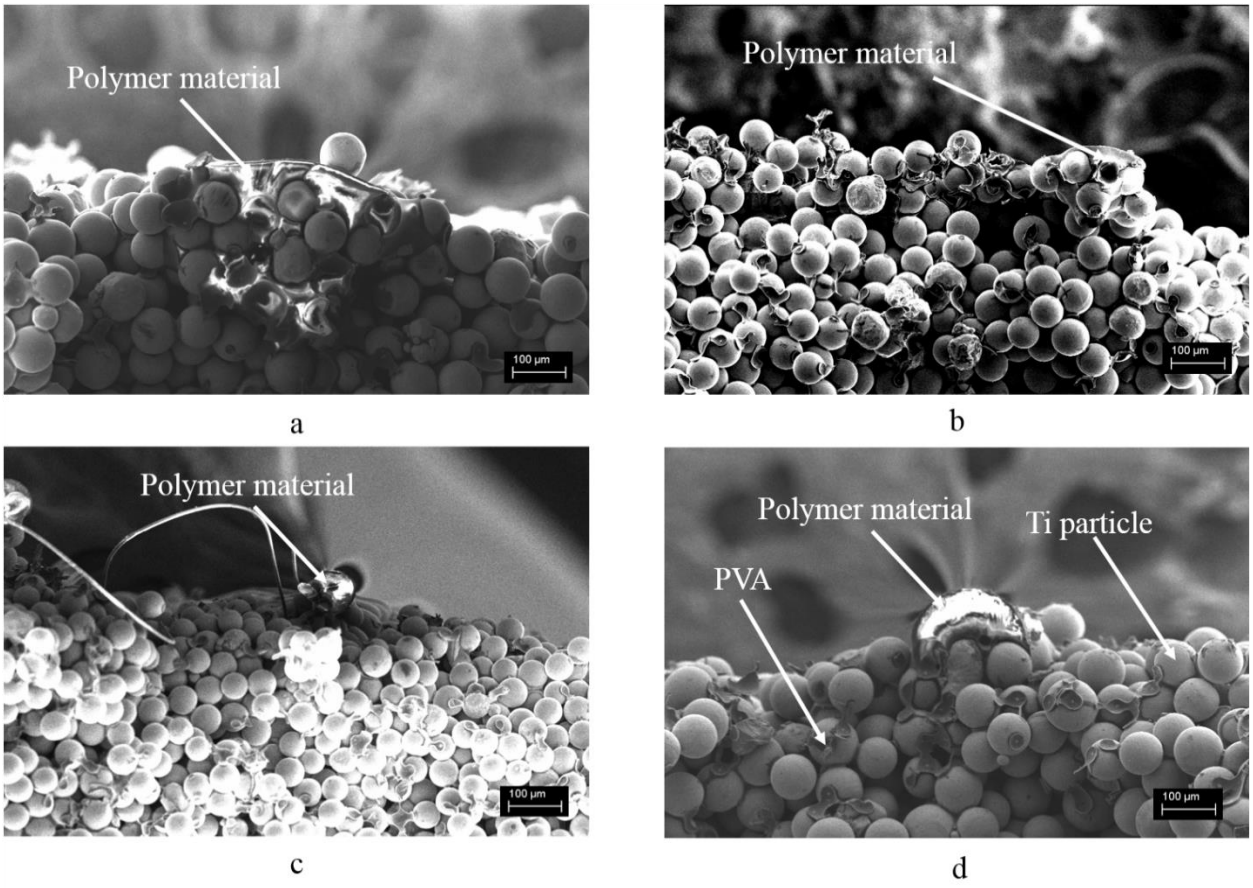

Figure 5-3 SEM images of the cross-section of the proposed polymeric pattern on the AM-made Ti substrate. Each figure annotation represents the similar polymeric batch

Prior to this step, the surface tension of Zb60 was also measured using a pendant drop measurement set-up. Determination of the interfacial tension between the binder and the polymer-coated substrates required the use of Young's equation (Equation (5-2)) accompanied with a proper choice of the equation of state. The Neumann's equation of state [147] (Equations(5-3)) is used for calculation of substrate surface energy and interfacial tension

$$\gamma_l \cos\theta = \gamma_s - \gamma_{sl} \quad \textbf{(5-2)}$$

$$\gamma_{sl} = \gamma_l + \gamma_s - 2\sqrt{\gamma_l \gamma_s}\, e^{-\beta(\gamma_l - \gamma_s)^2} \quad \textbf{(5-3)}$$

where γ_l is the liquid surface tension, γ_s is the cured polymer surface tension, γ_{sl} is the solid-liquid (polymer-binder) interfacial tension, and $\beta = 0.0001247(m^2/mJ)^2$. The interfacial terms are illustrated in Figure 5-4.

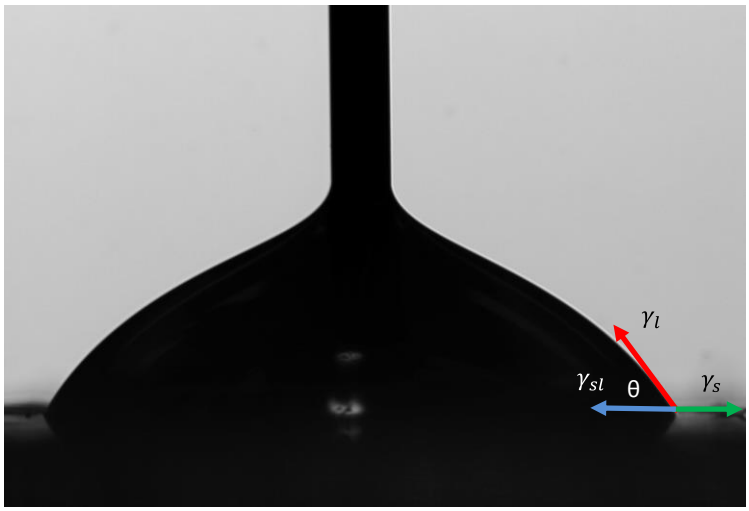

Figure 5-4 Schematic representation of surface/interfacial tensions between a binder drop and polymer-coated glass substrate

Following the measurement and calculation of the parameters, the work of adhesion was obtained from the following equation [149]:

$$W_{sl} = \gamma_l + \gamma_s - \gamma_{sl} \quad \textbf{(5-4)}$$

Table 5-3 presents the results of measurement for the surficial interaction between cured polymers and liquid binder (Zb60). As shown in the table, the maximum work of adhesion was obtained between material C and binder (91.9 mJ/m^2).

Table 5-3 Surficial interaction between binder and cured polymer

Sample	Zb60 contact angle (°)	Polymer surface energy (mJ/m^2)	Polymer-Zb60 interfacial energy (mJ/m2)	Polymer-Zb60 work of adhesion (mJ/m^2)
A	69.9±2.3	30.7	11.1	76.8
B	55.3±1.0	38.4	5.9	89.7
C	52.6±0.5	39.8	5.1	91.9
D	53.3±1.2	39.5	5.3	91.4

5.2.3 Characterization of the sacrificial polymer morphology deposited on the Ti substrate

In this study, a ULTIMUS ™ V high precision dispenser [EFD A NORDSON Company, MA, USA] was integrated with our custom designed binder jet AM system, as a nozzle dispensing module. Since the system actuates the dispensing by applying pneumatic pressure, the liquid flow can be determined through alternating this parameter as well as needle size, dispensing time and the viscosity of the polymers [128].

Therefore, eight sets of experiments were developed to study the role of these parameters (Table 5-4). As shown, only material and pressure were subjected as the experiments' variables. Our preliminary studies showed that a needle with 150 µm internal diameter provided a proper repeatability in the droplet morphological features compared to the smaller size needle (100 µm). In addition, alternating the dispensing time only was a significant parameter when increased to 1sec or more. The minimum value (0.1 sec) which has been shown to provide the acceptable result was selected to enhance the speed of the manufacturing process.

Table 5-4 Experiments set up for the dispensed polymeric droplet geometrical measurement

Experiment	Material	Needle diameter (µm)	Pressure (kPa)	Dispensing time (sec)
E1	A	150	10	0.1
E2	A	150	30	0.1
E3	B	150	10	0.1
E4	B	150	30	0.1
E5	C	150	10	0.1
E6	C	150	30	0.1
E7	D	150	10	0.1
E8	D	150	30	0.1

The dispensing distance between the nozzle and substrate is another important factor to control the size of droplets and preserve the integrity of the substrate. All the experiments were conducted with a dispensing distance of about 150 µm, which was the minimum distance feasible to avoid damaging the powder substrate. Next, the dimensional features of droplets were measured [Dino- Lite digital microscope, Taiwan] with respect to the variation in pressure and material viscosity. An example of the pattern for material A is shown in Figure 5-5.

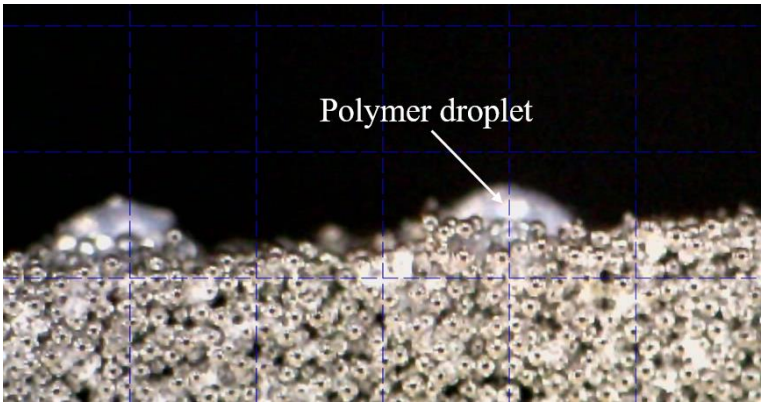

Figure 5-5 An example of photopolymer droplets pattern on the porous Ti substrate (material A)

Figure 5-6 shows the result of the designed experiments (Table 5-4) of the polymer droplets morphological features, for diameter and height of (0.29 ± 0.03) mm-(0.93 ± 0.06) mm and (0.12 ± 0.02) mm-(0.30 ± 0.08) mm, respectively. Considering this figure and the statistical analysis by employing the ANOVA method, a statistical significance in the geometrical properties of the samples was observed (p-value < 0.05).

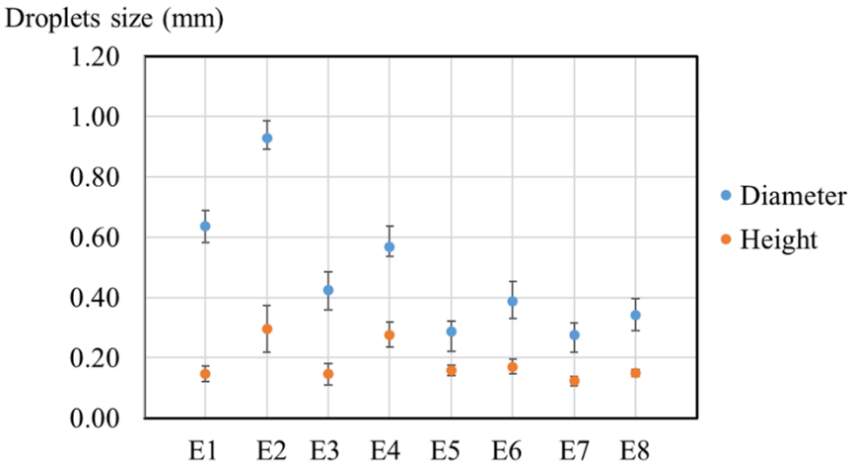

Figure 5-6 Morphological parameters of the dispensed parameters as function of pressure and material

5.2.4 Encapsulating the sacrificial polymer inside Ti layers: study of the effect of binder jetting process parameters

From our preliminary studies, we postulated the effect of following parameters on the quality of the AM-made samples with encapsulating polymer: the offset between the droplets (d), layer thickness (T), the number of the layers needed to cover the previous layers encapsulated with polymer (n), also known as buffer layers; and the number of the binder injections (m) from print head [ImTech 610, OR, USA] required to properly adhere the current layer of Ti to the next one. Figure 5-7 details the three steps of manufacturing from dispensing the droplets (a) to binder injection (b) and then spreading the next layer(s) of the powder (c).

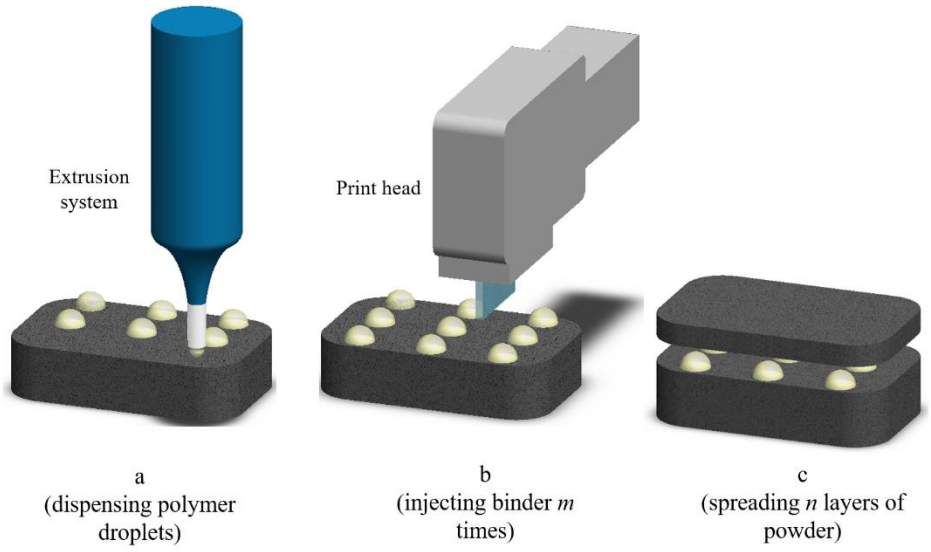

Figure 5-7 Process sequence and parameters identification in encapsulating the photopolymer inside the Ti layers

Figure 5-8 demonstrates an example of a successful sample (a) versus a sample with a defect (b) corresponding to the shift of layers.

Figure 5-8 Effect of the binder jetting process parameters on the quality of AM-made titanium samples with the embedded sacrificial polymer. a) presents a successful sample versus b) with a shift in layers

Therefore, a set of experiments involving the alteration of these variables was devised (Table 5-5). In these experiments, dispensing parameters similar to those in experiment 6 (E6) in Table 5-4 were employed.

The quality of the AM samples with the encapsulated sacrificial polymer is shown in Table 5-5. The successful trials are marked by “Ok” versus the defective samples, which have been indicated by “X”. As shown in this table, achieving a successful sample requires a minimum of 400 µm as a buffer between the layers with the encapsulated polymer. In addition, it was observed that the acceptable quality was achieved when the binder was injected twice (m = 2).

Table 5-5 Experiments set up for the AM quality control of the samples including the encapsulated polymer

Experiment	d (mm)	T (µm)	n- buffer layers	m (binder injection)	Quality control
AM1	1.5	200	1	2	X
AM2	1.5	200	2	2	Ok
AM3	1.5	200	2	3	X
AM4	1.5	200	4	2	Ok
AM5	1.5	150	1	2	X
AM6	1.5	150	2	2	X
AM7	1.5	150	4	2	X
AM8	1.5	150	4	3	X
AM9	1	200	2	2	Ok
AM10	1	150	2	2	X

5.2.5 Polymer thermal decomposition behavior and dimensional deviation

To assure the compatibility of decomposition trend in a polymer with proposed Ti sintering protocol [33], thermogravimetric analysis (TGA) was performed on material C. A similar study was conducted on the monomer (BEA) to investigate the effect of incorporating CAB on the thermal properties of the polymer blend. The analysis was divided into two steps with the first stage in the air (up to 295ºC) and second in a nitrogen environment (up to 800ºC). The heating rate details have been explained elsewhere [61]. The result of the TGA for both monomer and polymer in batch C is shown in Figure 5-9. As shown in this figure, both curves have a very similar trend specifically after increasing the temperature from 500°C. In addition, the specimen weights reduce dramatically after 400°C in the non-oxygen environment.

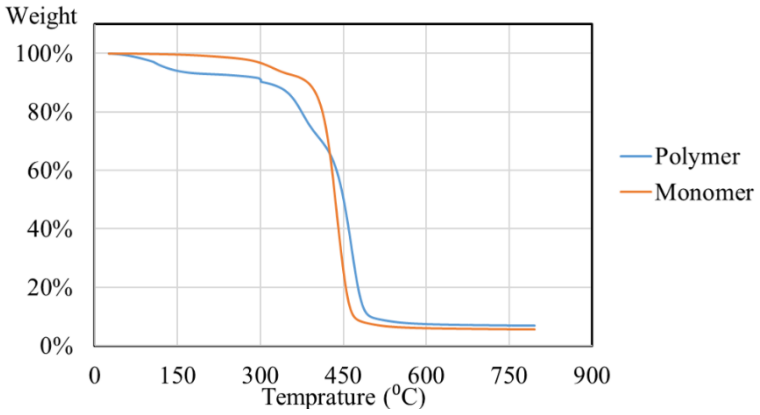

Figure 5-9 Result of the TGA for the polymeric blend C compare to the monomer

Next, one of Ti samples from droplets pattern characterization step (5.2.3) with material C droplets deposited on the surface was sintered to investigate the range of dimensional deviation in the cavities

resulted from polymer decomposition. The sintering included three main steps. First, the temperature increased up to 295°C in air environment; then Argon flow replaced the air and the temperature rose to 1400°C in three stages [112]. The diameter of cavities, after decomposing the polymer, was measured by analyzing the images from the stereo microscope [Leica A60S, Leica Microsystems, ON, Canada] and SEM images [FEI Quanta Feg 250 ESEM, FEI, US] with 10 kV voltage. This data then was compared with the size of the dispensed droplets.

The average achieved for the diameter of the cavities that resulted from decomposition of the material C droplets (E6, Figure 5-6) was (0.38 ± 0.04) mm (Figure 5-10). This data presented 1% of the dimensional deviation from the average diameter of polymer (0.39 ± 0.07) mm.

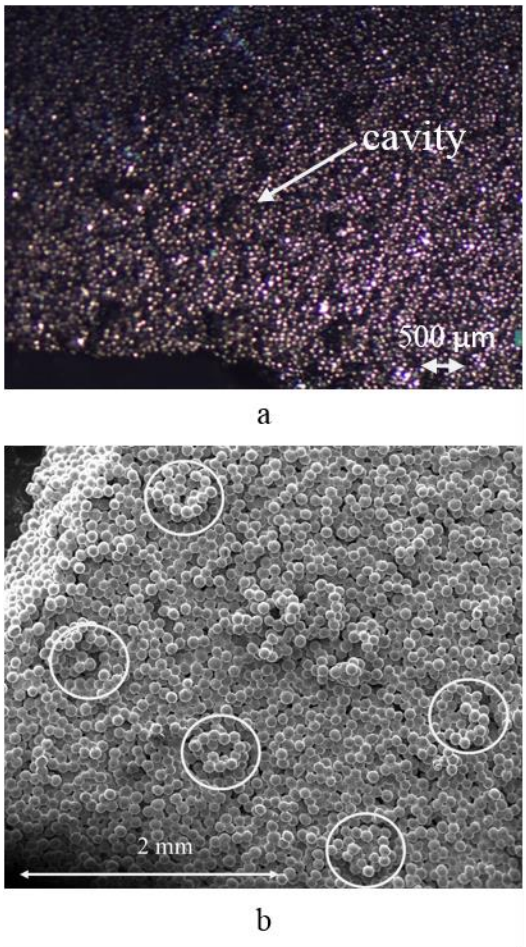

Figure 5-10 The cavities resulted by decomposition of material C droplets during the sintering process. a) shows the results captured from the stereo microscope and b) presents the higher magnification SEM image of the same samples with cavities marked by white circles

5.3 Discussion

This study has focused on developing a proper sacrificial polymeric material for the employment in a hybrid AM system (binder jetting and material extrusion) to fabricate titanium heterogeneous architectures through selectively adding and then decomposing the polymer in the post-processing step. The effect of the polymer composition and its properties, relevant to our study, was measured including rheological, interfacial and thermal decomposition behavior. The study also assessed the role of dispensing parameters on the geometry of polymer droplets as well as binder jet process parameters on the quality of the AM-made titanium samples with the encapsulated polymer.

To select the best candidate to maintain the integrity of Ti green parts from the list proposed in Table 5-1, viscosity and surface tension of polymers as well as their contact angle with Ti substrate were measured. As shown in Figure 5-2, the trend in the viscosity variation with respect to the shear rate classified the material as shear thinning, thus suggesting the feasibility of dispensing the polymers [124]. The range of viscosity suggested significant differences among the material batches, which is due to an increase of the thickening segment (CAB) [150]. The highest range was observed in samples C and D (with 20 wt. % and 18 wt. % CAB, respectively). Next, when the surface tension of materials (Table 5-1) was measured, a similar trend was observed in the average of surface tension when CAB percentage increased. This resulted in the variation in the range of 48.5 ± 1.5 mJ/mm^2 to 59.0 ± 0.5 mJ/mm^2, respectively (Table 5-2). From this data, one can conclude a direct correlation between the concentration of CAB and the increase of the surface energy of the material in the defined range of CAB weight fraction and therefore the wettability of Ti substrate.

A similar conclusion was drawn from studying the range of contact angle between polymers and Ti porous substrate, which suggests the higher wettability (lower contact angle) between material C and Ti substrate [130]. As mentioned earlier, although micro-roughness on the surface of substrates is an important factor which affects the wettability [151], the effect of this parameter was not included in the measurement. A statistical significance was observed through ANOVA analysis performed on each of the properties in Table 5-2 as a single factor (p-value < 0.05).

Next, the data measured from this step was introduced in the Washburn model (Equation (5-1)) demonstrating the minimum polymer infiltration rate for material C (0.03 m^2/s) which corresponds to the highest viscosity (31397.5 cp) and surface tension (59.0 mJ/mm^2). This result suggests that material C is more appropriate in our application context, as it can limit the effect of shrinkage stress induced during UV curing of the polymer [133], only to the Ti particles surrounded the droplet and located on the surface of the substrate. It should be noted that due to the limitation of the measurement methods, such as difficulty

in obtaining the viscosity at zero shear rate, surface roughness, and applied analytical model, this step was performed only to evaluate the polymer infiltration more qualitatively. Future studies can be proposed to increase the accuracy of data by alternating measurement instruments and advancing the model. In addition to employing the Washburn model, SEM imaging was performed on the cross-section of Ti substrate and the polymer materials, which corroborates a similar conclusion. Therefore, a better sample quality was obtained when category C was applied even when continuous polymer tracks (lines) were deposited (Figure 5-1-b).

Assessment of the interaction between the cured polymers and liquid binder revealed a better adhesion between batch C and Zb60, with 91.9 mJ/m^2 work of adhesion and a contact angle of 52.6°. This data suggests a better adhesion and wettability between these two phases and, thus a more appropriate integrity between the layers of Ti in green step can be expected [22], [27].

When the morphology of the polymers' pattern was evaluated in the dispensing step, a dramatic reduction in the size of drops from employing material C and D was observed while the backpressure was constant. The same trend was achieved in the data when the only variation in the dispensing pressure was studied. Both outcomes among the data were predictable, since increasing the pressure and decreasing the viscosity of the fluid can enhance the flow-ability throughout the nozzle, thus resulting in a bigger droplet size [125], [127]. In addition, the ANOVA single factor analysis of variance indicates a significant statistical variation with respect to each of the input parameters. Moreover, the range of diameter (0.29 ± 0.03) mm to (0.93 ± 0.06) mm suggested a close similarity with the human trabecular bone separation [113]–[115], which suggests our proposed approach and material as a proper candidate in the synthesis of bone substitutes. However, the height of the samples demonstrated a smaller range of (0.12 ± 0.02) mm to (0.30 ± 0.08) mm in experiment E7 and E2; respectively and with respect to the range of contact angle [152].

Figure 5-9 shows the thermal decomposition behavior of the material C and monomer in correlation with temperature and types of atmosphere. The graphs indicate a dramatic decomposition rate in both materials around 400°C in a nitrogen environment. A comparative evaluation of the results demonstrates a slight decrease in the onset decomposition temperature of material C due to incorporating CAB particles [153], [154]. By comparing this result with our developed sintering protocol for Ti [112], one can conclude that the proposed polymeric blend is a suitable candidate as a sacrificial material in our system and for further applications. Since no residue will be left after the titanium sintering process (increasing temperature up to 1400 °C), the final porous structure with controlled heterogeneity could be a promising candidate in the context of biomedical applications [49].

The analysis of the size of cavities, which resulted from sintering an AM-made Ti sample with deposited droplets of material C on the surface (Figure 5-10) revealed a shrinkage of 1%. This result suggests that the control of the size of pores through alternating the input parameters is feasible. Further studies could be suggested to evaluate other geometrical dimensions of embedded cavities inside the Ti structure with more precise methods such as micro-computerized tomography (μCT) scanning.

As shown in Figure 5-10, although material C displayed the minimum rate of infiltration among others, still some micro-deformation can be observed on Ti surface. The rearrangement of Ti particles is attributed to the polymerization shrinkage stress as well as variation in solidification time between the section of polymers placed on the Ti surface and the one permeated the substrate. However, as shown in this figure the arrangement has been limited to only one particle in the radial direction which formed a ring encompassing the cavity. This corroborates our previous conclusion, from materials permeability, on the suitability of material C for our application.

From the results obtained in the previous steps, material C was selected to investigate the effect of binder jetting system parameters on the quality of samples with the encapsulated polymer. As shown in Table 5-5 for a successful bond between Ti layers with polymer droplets included and the rest of specimen, a minimum of 400 μm gap filled with the main powder material (Ti) is required before embedding polymer on the next layer of powder. From the data presented in Figure 5-6 for the height of droplets (0.17 ± 0.02) mm in the experiment E6, one can conclude that the first buffer layer (200 μm) is essential to cover the polymer pattern. Encapsulating the polymer on this layer, by creating the excessive binder saturation within the layers, also resulted in a shift between the layers (AM1, Table 5-5) and deformation in the green part. Thus, incorporating the second buffer layer in the design of samples was crucial to eliminate this problem. Moreover, the proper number of binder injection ($m = 2$) led to the sufficient adhere between the binder-polymer-Ti combination as well as and Ti-binder-Ti [84]. It can be concluded that increasing the quantity of *m* (number of binder injection on polymer-Ti layers), enhances the likelihood of the layer sliding by decreasing the friction between the wet substrate and the newly spread dry one.

The results of this study revealed the direct influence of mass fraction of CAB additive on the effective properties of polymer mixtures for our applications. Although the material was characterized for successful additive manufacturing of heterogeneous structures from Ti powder with a certain particle size, the similar material can be applied to other studies with variation in the type or size of the powder. Particularly because the material can be decomposed at a temperature less than 400°C, which is much lower than the sintering temperature of metals or ceramics applied in binder jetting or another method of AM and the relevant high dimensional accuracy (only 1 % error in the dimension of pores). This characteristic will provide an

opportunity for creating micropores and cavities or it will suggest that incorporating small sections of other material inside the main powder matrix to create composite structures is feasible. Both ideas are under investigation by the authors. The application of the analytical model in this research can also be extended to other studies in the context of additive manufacturing when there is a possibility of liquid and porous media interaction such as selective laser melting or sintering.

5.4 Conclusion

In this article, four polymeric blends material which combined a variable concentration of bisphenol-A ethoxylated diacrylate and cellulose acetate butyrate powder were introduced as a potential sacrificial material in the binder jetting-nozzle dispensing hybrid AM system. The material (C) containing the maximum concentration of CAB powder (20 %) demonstrated the minimum rate of infiltration (0.03 m^2/s), from the Washburn model, inside the porous Ti substrate, suggesting a better manufacturing quality by limiting the polymer – particles interface to reduce the effect of shrinkage stress. A study of the effective binder jetting manufacturing parameters, when integrated with nozzle dispensing to fabricate the heterogeneous Ti samples, revealed the direct influence of the layer thickness and binder saturation level (2 times binder injection) in maintaining the structural integrity of the AM-made specimens. The results demonstrated a minimum of 400 µm space, filled with the main samples material (Ti powder), was required to cover the layer with the encapsulated polymer. The thermal decomposition behavior of the material C in the non-oxygen environment and the structural stability (1% deviation in cavity size) suggested the suitability and compatibility of our approach for AM of cellular metal architectures.

6 Additive manufacturing of functionally graded titanium structures with selective closed-cells layout and controlled morphology

6.1 Introduction

Titanium (Ti) and its alloys are widely applicable due to outstanding properties such as corrosion resistance, relevant high strength per weight ratio, non-magnetic property, and high thermal resistivity [44]–[46]. Such properties have increased their demand in industrial (e.g. aerospace, automotive) [47], [48] as well as biomedical applications, such as load-bearing bone implants with promising biocompatibility [45]. However, an orthopedic practice, the solid Ti is still much stronger than the bone tissue, which suggests the fabrication of functionally graded cellular Ti to meet the similar mechanical/stiffness properties with surrounding tissue and eliminate the stress shielding effect [49].

Additive manufacturing (AM) methods have created the opportunity for fabricating the functionally graded cellular solids with tailored mechanical and cell morphological features in each segment of samples based on the application [155][156]. From different AM methodologies, binder jetting has been one of the most promising candidates in the fabrication of bio-substitutes due to the ease of incorporating porosity into structures, employing different types of powders, powder recycling, cost of the system, etc. [157], [84].

Cellular solids, in general, can be classified into different categories in terms of cell types and distributions [158]. Although incorporating open cells into a structure provides the advantage of bone tissue ingrowth and interconnection, closed-cells are essential to tailor the mechanical properties of the implant [3]. The first can be obtained by incorporating open channels with variable design and feature sizes into the architecture of samples [155], [159]. The second type of cells can be structured by manipulating the manufacturing parameters, powder size, shape and composition (in powder-bed AM), etc. [33], [112]. To surpass the obstacle for creating the variation in closed-cells morphology and distribution, different approaches have been suggested, including the use of bimodal powder in the binder jetting AM method [27], [94]. In this method, the powder is composed of the main material and a smaller percentage of a sacrificial element (porogen) which will be removed from the samples through a post-processing step. In addition to the manufacturing parameters such as layer thickness and binder saturation level [22], the pore size will be a function of the size and fraction of the sacrificial elements [33], and porosity is distributed more sporadically throughout the AM-made layout. As a result, integrating the periodic closed-cells with control layout inside the part is not feasible.

Encapsulating the sacrificial material on selective locations of each layer has been suggested by the multi-scale additive manufacturing group [10] to overcome the obstacle. One approach is to embed the wax solid particles, separated from a sheet of paraffin [61]. In the other technique, a hybrid binder jetting and material extrusion system is introduced for encapsulating a sacrificial photopolymer within the structure [10], [32].

In this study, a binder jetting approach in conjunction with material extrusion is employed to manufacture heterogeneous Ti structures with periodic closed-cells and tailored morphology. Overall porosity of the samples was provided by applying a powder-bed AM method and employing a bimodal powder composition. Moreover, to locally enhance this parameter throughout the samples, sacrificial photopolymer droplets [74] were dispensed on the designated layer of Ti to create a gradient in the corresponding layers as well as the entire architecture. The polymer is composed of bisphenol-A ethoxylated diacrylate (BAE) and cellulose acetate butyrate (CAB). Later, the droplets were decomposed in the gravity-based sintering step, which resulted in the formation of controlled cavities.

Eight groups of specimens were devised; three of which incorporate the effect of droplets size, droplets number and distribution throughout the Ti parts. One category was designated to integrate the combination of the encapsulated polymer as well as variation in layer thickness to study the role of inhomogeneous hierarchical pore distribution. Since the previous study [74] demonstrated the necessity to increase the binder saturation level to attain the proper integrity in the parts when the polymer was dispensed on a layer, the last four control samples were designed to mimic the parts without encapsulating the polymer.

After manufacturing, the dimensional deviation of the parts as a function of the heat treatment [74] step was measured. Then, the porosity of the samples was determined by applying the Archimedes approach in addition to analyzing the data from micro-computerized tomography (μCT). Then, the mechanical strength of the Ti cellular structures was investigated through defining the Young's modulus and the Yield stress. A formula was proposed to predict the porosity of the samples after removing the polymer via the data obtained from the control samples. A similar approach was followed when the stiffness of the parts as a function of layer thickness, binder saturation level, and polymer removal was studied. Lastly, scanning electron microscopy (SEM) was conducted to evaluate the quality of sintering compared to previous works.

6.2 Materials, methods, and results

6.2.1 Additive manufacturing of specimens

To investigate the effect of encapsulated photopolymer inside the layer of Ti, eight experiments were devised. Each experiment included eight cylinders with 8 mm height and 5 mm diameter, which were designed and then sliced to the proper number of layers in solid works [SolidWorks Corp., Concord, MA] and netfabb [netfabb GmbH, Germany], respectively. The design of the samples were conducted where the

role of input variables such as size of droplets (d), number of droplets per layer (m), number of Ti buffer layers locating between two consecutive layers of Ti with included polymer droplets (n), layer thickness (Th) and level of binder saturation throughout the samples (Table 6-1) were taken into account.

Table 6-1 Detail of the design of the samples with encapsulated polymer

Sample	Pressure (kPa)	Number of droplets per layer (m)	Number of the buffer layers (n)	Layer thickness (µm)
S1	30	16	4	200
S2	10	16	4	200
S3	30	9	2	200
S4	30	9 (in 200 µm section)	4 (in 200 µm section)	200 / 80

Samples S1 to S4 incorporate the different sizes, numbers, and configurations of the droplets into the specimen. Figure 6-1-a shows the building sequence of these samples. As shown in the figure, the first four layers with a layer thickness of 200 µm were created with the binder jetting system. In the second step, depending on the design, the proper number of polymer droplets was dispensed on the Ti layer.

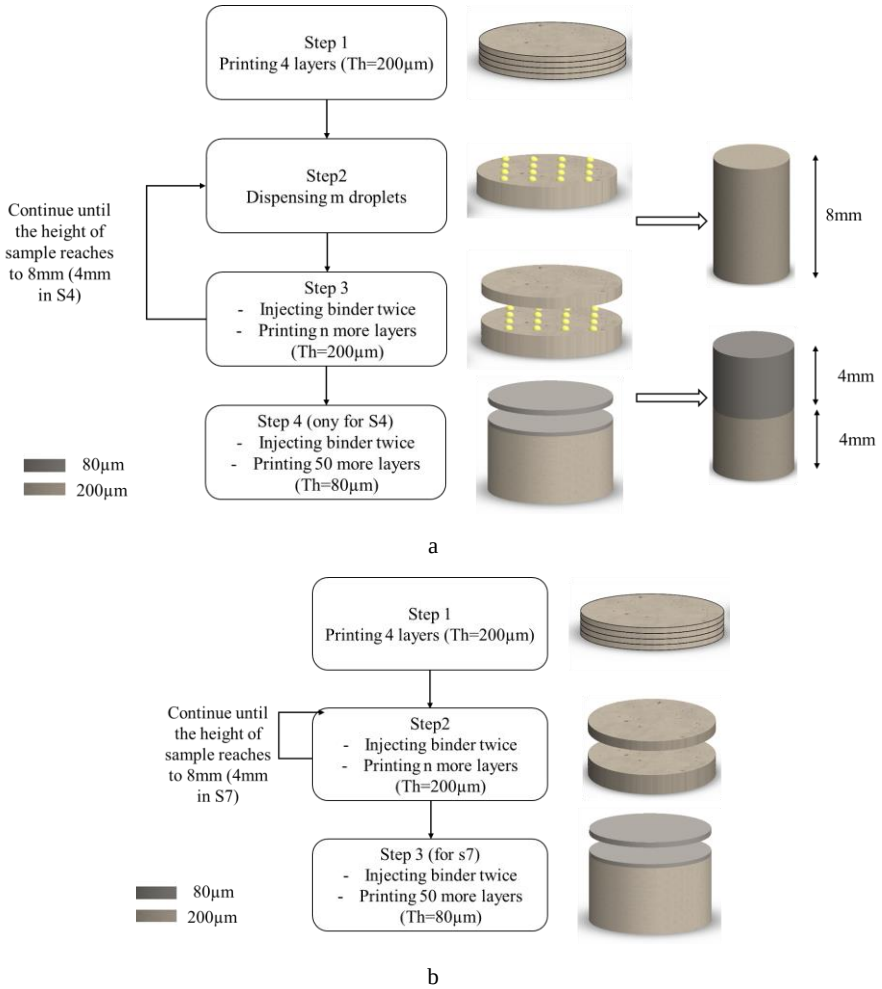

Figure 6-1 The sequence of Additive Manufacturing of the samples. a) shows the sequence of S1 to S4 and b) demonstrates the control samples

This step was followed by injecting the binder twice to provide the sufficient adhesion to the next layer of Ti [74]. After the spread of the *n* buffer layers, the same sequence was repeated from the second step in order to complete the AM of the Ti samples with the target height. Figure 6-2 shows the layout of the droplets based on the number of the drops per layer (*m*).

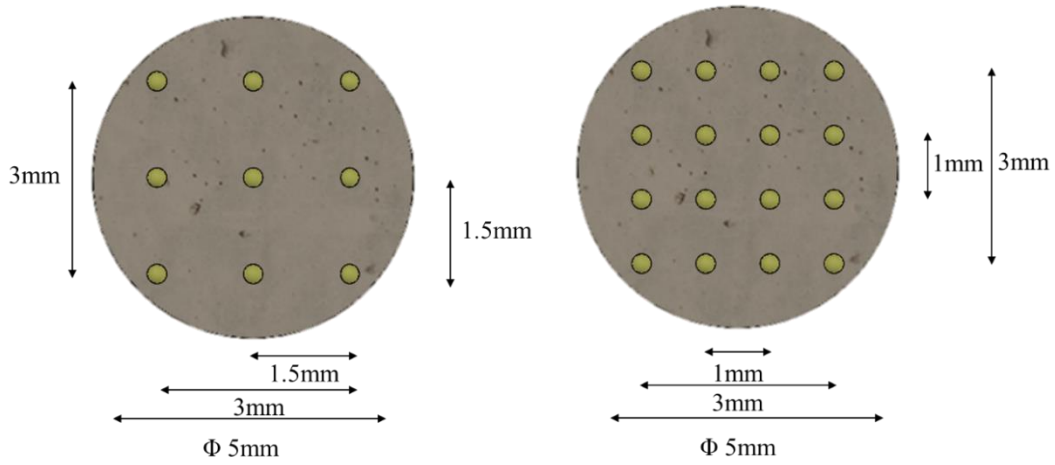

Figure 6-2 Polymer droplets distribution on Ti substrates. Right image shows the distribution for m = 9 and left shows the layout for m= 16 (Table 6-1)

The influence of the layer thickness variation accompanied with the effect of polymer encapsulation on the properties of S4 was studied, when the top half of the samples were AM-made by decreasing the layer thickness to 80 µm. In this sample, the polymer was embedded only on the 200 µm layers and between every four layers with a sequence similar to that demonstrated in Figure 6-1-a.

To eliminate the role of variation in the layer thickness as well as selectively increasing the binder saturation levels at certain layers, samples S5 to S8 were developed as control samples (Table 6-2 and Figure 6-1-b). Samples S5 to S7 were designed to mimic the similar fabrication process as S1, S3, and S4; respectively, and without including the polymer. In addition, S8 was made with the single layer thickness of 200 µm and by injecting binder only one time per each layer.

Table 6-2 Detail of the design of the control samples

Sample	Number of extra binder injection per layer (p)	Number of the buffer layers (n)	Layer thickness (µm)
S5	2	4	200
S6	2	2	200
S7	2 (in 200 µm section)	4 (in 200 µm section)	200 / 80
S8	0	0	200

Later, the green samples were cleaned and placed inside a MTIV high-temperature tube furnace [GSL-1500X-50, Richmond, CA] to complete the two steps sintering. The details of the heat treatment protocol have been described elsewhere [112].

6.2.2 Effect of sintering on the dimensional deviation of samples

The effect of sintering on the geometrical features of the samples was studied through the steps detailed in section 3.2.3. The result is shown in Table 6-3. A range of (3.4 ± 1.7)%, in S3, to (6.9 ± 1.5)%, in S4, was obtained for the diameter. The shrinkage in height of the samples varied from (2.8 ± 0.9)% (S3) to (5.7 ± 0.8)% (S5).

Table 6-3 The average of dimensional deviation in samples after sintering

Sample	Diameter Shrinkage (%)	Height Shrinkage (%)
S1	5.1±1.3	4.6±0.7
S2	4.6±1.9	4.7±0.4
S3	3.4±1.6	2.8±0.9
S4	6.9±1.5	5.1±0.5
S5	5.6±1.8	5.7±0.8
S6	3.8±1.7	4.7±0.8
S7	4.9±1.5	5.1±0.5
S8	5.1±1.4	5.6±0.4

When the data for all the samples was evaluated by ANOVA (Table 6-4), the p-value < 0.05 was achieved for both diameter and height. The same trend was observed when only samples S1 to S4 were compared. However, in the case of S5 to S8, with selective variation in the binder saturation level and the layer thickness, only the deviation in height was noticeable.

Table 6-4 The range of p-value from ANOVA single factor analysis of the variance (the significant variation among the inputs data is highlighted)

Inputs	Diameter shrinkage	Height shrinkage	Porosity	Young modulus	Yield stress
S1 to S8	< 0.05	< 0.05	< 0.05	< 0.05	< 0.05
S1 to S4	< 0.05	< 0.05	> 0.05	> 0.05	< 0.05
S1 & S2	> 0.05	> 0.05	< 0.05	< 0.05	> 0.05
S1 & S3	< 0.05	< 0.05	> 0.05	> 0.05	< 0.05
S1 & S4	< 0.05	< 0.05	< 0.05	> 0.05	> 0.05
S5 to S8	> 0.05	< 0.05	< 0.05	< 0.05	< 0.05
S5 & S6	> 0.05	> 0.05	> 0.05	> 0.05	> 0.05
S5 & S8	> 0.05	> 0.05	> 0.05	> 0.05	> 0.05

6.2.3 Porosity measurement

The porosity of the Ti samples after removing the sacrificial photopolymer during heat treatment was determined by applying the Archimedes method (ASTM B311 [96] & C373 [97]). The detail of the experiments is presented in section 3.2.4. Figure 6-3 shows the porosity of the samples measured by the Archimedes method. As shown in this figure, the minimum porosity of (33.6±1.5)% (S7) and maximum of (41.8±2.4)% (S1) were achieved by analyzing the data from this method. Table 6-4 demonstrates the notable statistical variation between the porosity of the samples while comparing the results for (S1 and S2), (S1 and S4), (S5 to S8) and all the samples (S1 to S8) together as an input for ANOVA analysis.

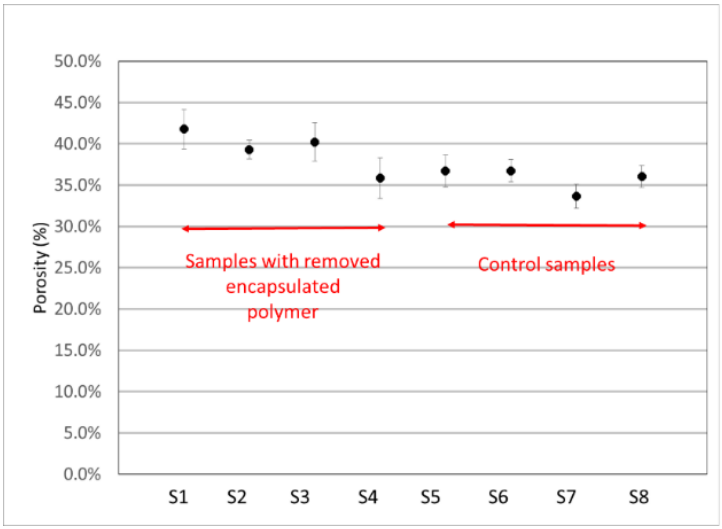

Figure 6-3 Porosity of the samples measured by the Archimedes method

Moreover, the porosity of samples S1 to S4 was estimated ($P_{expected}$) by employing the data obtained from the porosity of samples S5 to S8 and by applying the following equation:

$$P_{expected} = P_{raw} + \left(\frac{V_{polymer}}{V_{solid}}\right) \quad \text{(6-1)}$$

where $V_{polymer}$ is the overall volume of the polymer droplets calculated by considering their diameter, 0.3 mm (at 10 kPa-pressure) and 0.4mm (at 30 kPa-pressure) [74], and their number per sample based on the design of the part. In this step, the volume of each single droplet was estimated by the volume of a hemisphere. V_{solid} represents the volume of the solid cylinder with 8 mm height and 5 mm diameter. P_{raw} is the average porosity of the samples with similar manufacturing properties minus the effect of polymer and based on the results of the measurement (S5 to S7).

As shown in Table 6-5 the error margin of 3.8% (S3) to 7.6% (S1) resulted when the porosity of S1 to S4 obtained from Equation (6-1) was compared with the results obtained by the Archimedes method.

Table 6-5 Comparing the porosity of the samples S1 to S4 from theory and experimental data

Sample	$P_{expected}$ (%)	$P_{measurement}$ (%)	Error (%)
S1	38.6	41.8	7.6
S2	37.5	39.3	4.6
S3	38.7	40.2	3.8
S4	34.1	35.8	4.9

6.2.4 Micro CT scan analysis

To investigate the pores' morphology, distribution and effect on the microporosity of the samples after removing polymer, four categories (S1, S3, S4, and S8) were chosen for micro CT scan (µCT). Samples S1 and S3 were selected to study the role of pore numbers and layouts. Sample S4 includes the effect of layer thickness variation and selectively embedded pores. In addition, sample S8 was studied as a control specimen. One sample from each of the four categories was subjected to the X-ray µCT on SCANCO Medical µCT 100 system [SCANCO Medical AG, Switzerland] with ~ 6 W (90 KVp, 66 µA) and 0.1 mm copper filter. Then the 3D reconstructions were obtained by applying a spatial resolution of 5 µm/voxel.

A customized model developed by Expanse Microtechnologies [Expanse MicroTechnologies Inc., Canada] was employed to analyze the data. To reduce the computational load and by considering the symmetrical design of S1, S3, and S8, only half the height of the samples (4 mm) was analyzed. However, S4 was analyzed throughout the full height (8 mm). In addition, the masked images were cropped to a size representing 4.5 mm × 4.5 mm (Figure 6-4). From the results of analysis the pore size, distribution and porosity were determined. The pore diameter was defined as the largest sphere that could fit within the pore.

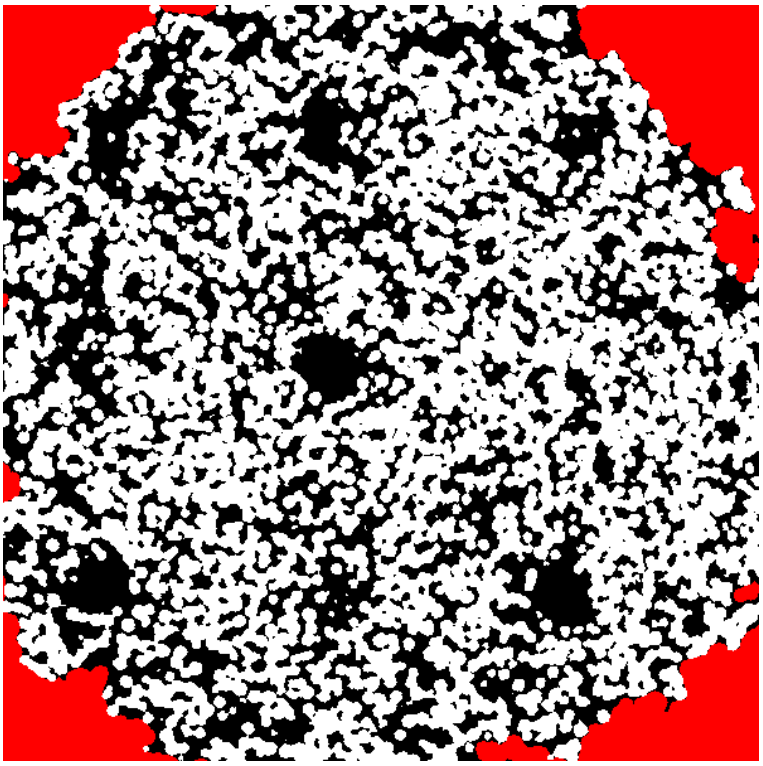

Figure 6-4 Masked and cropped image (4.5 mm × 4.5 mm)

The average diameter of the pores (mean value) throughout the designated height and the associated standard deviation (stdv) were calculated. To demonstrate the variation range for this parameter with respect to the height, the minimum pore size and maximum pore size were calculated in each section, as follows: (min pore = mean - stdv) and (max pore = mean + stdv), respectively (Figure 6-5). As shown, the selectively encapsulating of the sacrificial polymer has resulted the peak formation in the max pore graphs. The number of peaks corresponds to the number of layers with embedded polymeric droplets based on the samples design (see Figure 6-1, Table 6-1 and Table 6-2).

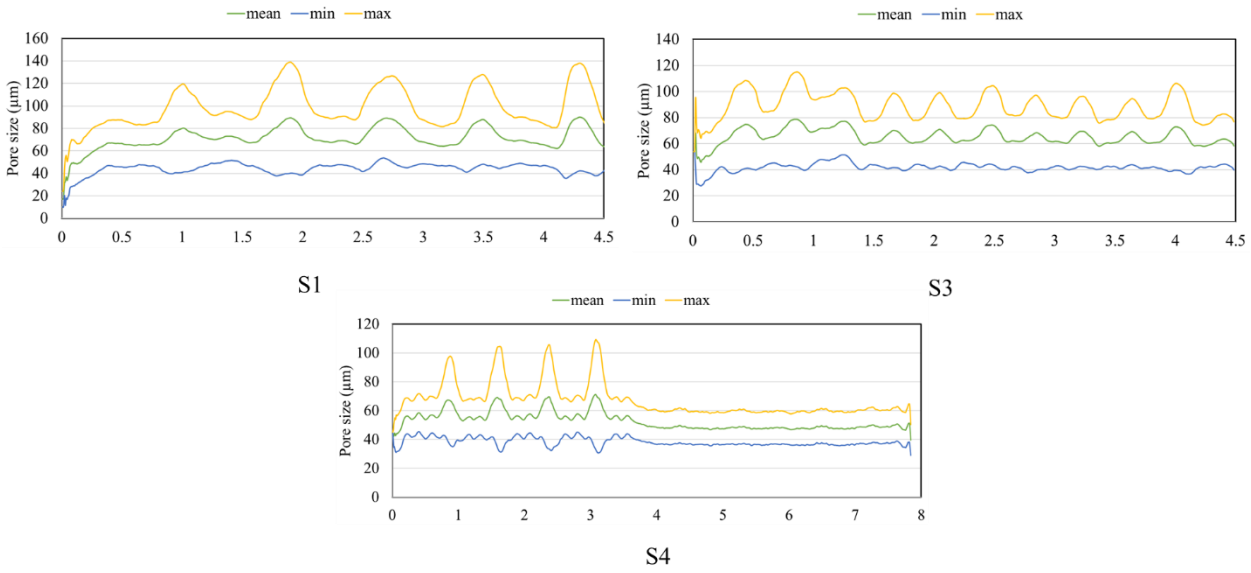

Figure 6-5 Pores distribution as function of the height of the sample

The porosity distribution with respect to the height and the average porosity of the samples are presented in Figure 6-6 and Table 6-6, respectively. As shown in this table the domain of (35.8±4.3)% to (40.8±3.0)% for the average porosity of the specimens was obtained.

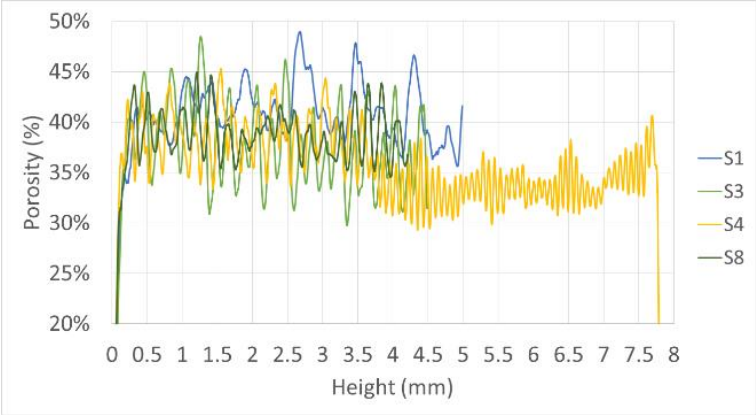

Figure 6-6 Porosity variation through the height of the samples

Table 6-6 Comparing the porosity of the samples from Archimedes method and analyzing the µCT scan data

Sample	$P_{\mu CT}$ (%)	$P_{Archimedes}$ (%)
S1	40.8±3.0	41.8±2.4
S3	37.9±4.0	40.2±2.3
S4	35.8±4.3	35.8±2.4
S8	38.7±2.4	36.1±1.3

Figure 6-7shows the isotropic view of the 3D rendering of the pore network model for S4. The bottom gray section represents the part of the sample which was manufactured by applying 80 µm for layer thickness.

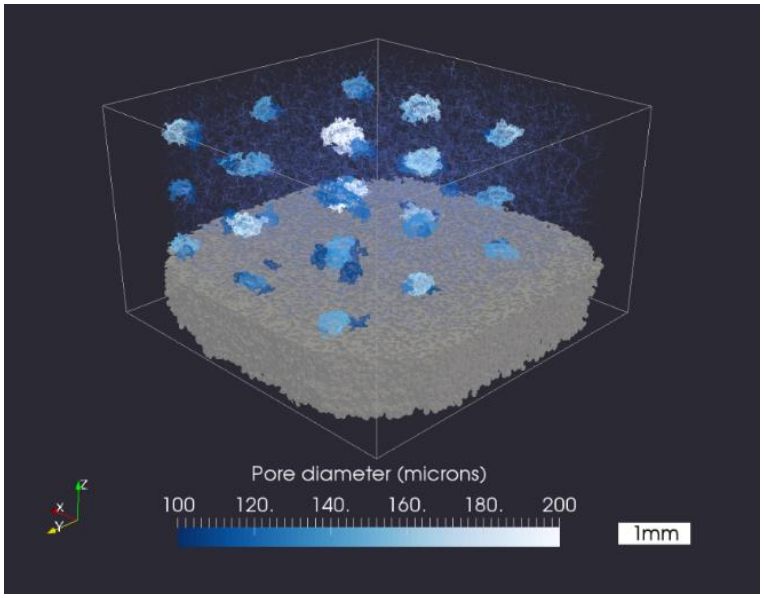

Figure 6-7 3D rendering of the pore network for sample S4

6.2.5 Mechanical compression test

To investigate the mechanical strength of the samples through measuring the Young's modulus (E) and Yield stress (0.2% stress), seven samples from each category were subjected to the compression test. The test setup is explained in chapter 3 (3.2.5). The results are shown in Figure 6-8 and Figure 6-9, respectively. Samples S2 and S3 demonstrate the minimum value for the average of Young's modulus and Yield stress, respectively. The maximum value for the similar parameters was obtained in S7. The range of p-value when different combinations of the samples were imported to the ANOVA analysis is shown in Table 6-4.

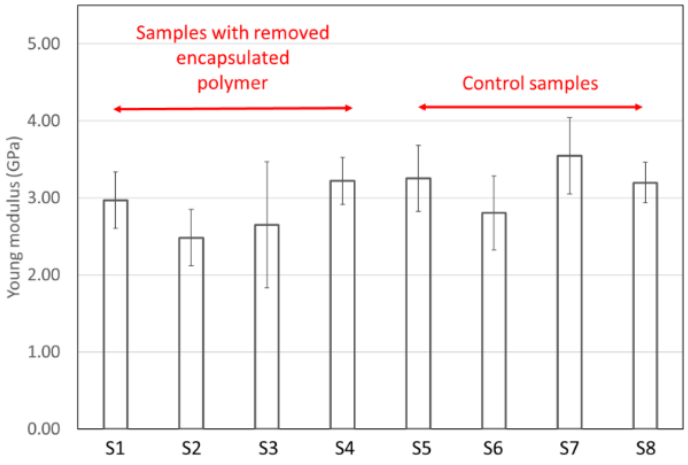

Figure 6-8 The Young's modulus of the samples

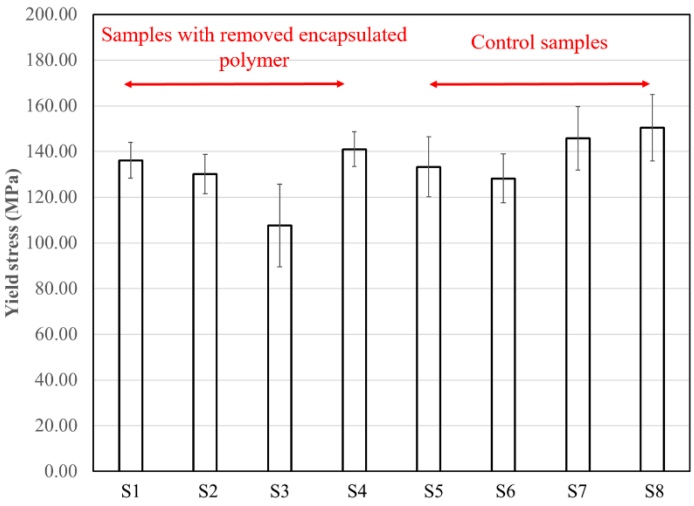

Figure 6-9 The Yield stress (0.2% stress) of the samples

To explore the effect of a variable layer thickness, incorporated close cells from polymer decomposition and variation in binder saturation level, the stiffness of S4 and S7 was calculated by deploying Equation (3-6) [112]. Where E_B is the Young modulus of AM-made samples while using a layer thickness of 80 µm (3.4 GPa), obtained from our previous study [112], and E_A represents the Young modulus of S3 and S5 for estimating the stiffness of S4 and S7, respectively.

When the stiffness of S4 and S7 calculated from the proposed correlation in Equation (3-6) was compared with the compression data, a deviation of 7.5 % and 6.2 % for S4 and S7, respectively was observed (Table 6-7).

Table 6-7 Comparing the stiffness of the samples S4 to S7 from theory and experimental data

Sample	E_{em} (GPa)	$E_{measurement}$ (GPa)	Error (%)
S4	3.0	3.22	7.5
S7	3.3	3.55	6.2

6.2.6 Structural analysis through scanning electron microscopy (SEM)

To observe the fracture region occurred during the compression test, SEM analysis was performed using a SEM [ULTRA Plus, Zeiss, Germany] with 10 KV voltage. Figure 6-10 illustrates the SEM images of the sintered samples before and after being subjected to the compression test. A similar quality and range of sinter necks as in our previous work [112] were obtained (Figure 6-10-a). Figure 6-10-b demonstrates the failure initiation from the sinter necks between particles.

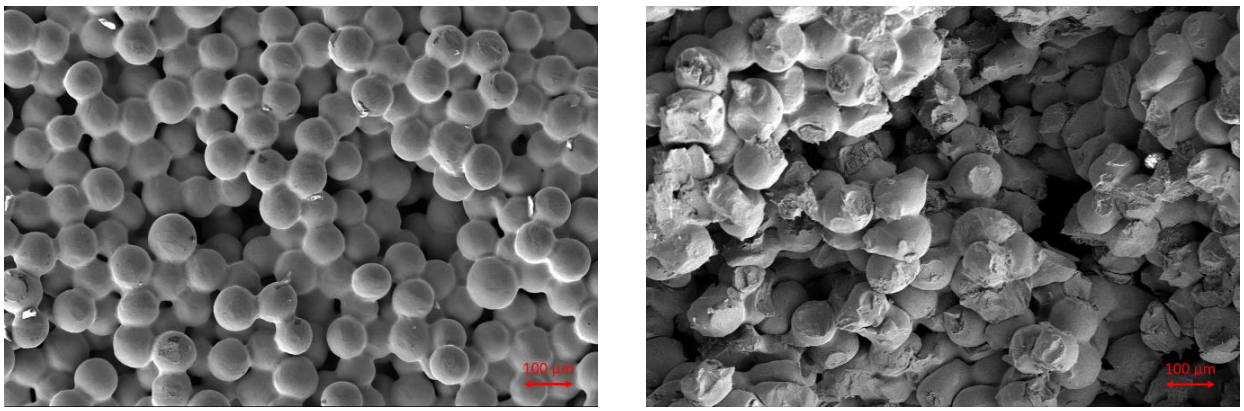

a b

Figure 6-10 SEM of the samples. a) shows the quality of the sinter neck and b) the failure points during the compression test

6.3 Discussion

This article has presented the results of mechanical and structural properties of cellular Ti structures with selective pore morphology and distribution throughout the parts. The cellular structures were manufactured by a combined process including binder jetting AM of Ti powder, and material extrusion AM of the sacrificial polymer droplets at the designated layers with a selective layout to enhance the porosity per locations. Eight categories of samples (S1 - S8) were designed. In the first three groups, the influence of the droplets size, number, and distribution was investigated. Sample S4 incorporates the combination of embedding periodic cells in addition to the variation in layer thickness to explore the role of dramatic change of porosity selectively through a single part. Samples S5 to S8 were studied as control samples to replicate parts made by the binder jetting AM process without any added sacrificial polymer and variable

layer thickness. These specimens were characterized in terms of geometrical deviation, porosity, and mechanical strength.

The shrinkage analysis in geometrical features of specimens shows the range of (3.4±1.7)% to (6.9±1.5)% in diameter and (2.8±0.9)% to (5.7±0.8)% for height (Table 6-3). Comparison between the samples with sacrificial polymer and the control samples showed a decrement in the height shrinkage. It may have been attributed to the fact that the existence of the polymer droplets reduces the number of Ti particle contacts and, therefore, it decreases the possibility of sinter neck formation in the direction of printing [161]. In addition, a viscous liquid before decomposition may apply counterpart wetting and capillary forces on the Ti particles, reducing the contact force and the final sinter necks. This hypothesis can corroborate the minimum shrinkage obtained in S3 by incorporating 21 layers with embedded polymer throughout the sample. A similar conclusion was drawn when ANOVA was conducted on the pair of S1 and S3 (Table 6-4). Combining this factor with the variation in the layer thickness resulted in a higher level of shrinkage in height of S4 (5.1±0.5)% compared to the rest of the batches including only the effect of polymer decomposition (S1 to S3). Studying the results for S5 to S8 categories demonstrates the significant role of variation in the layer thickness rather than selectively increasing the binder saturation level. The higher standard deviation in the diameter could be affected by the direction in which the samples were placed inside of the furnace, similar to the 3D printing layout, which increased the probability of gas escaping from the top and side of the samples. The results are comparable with the previous study, in which, a similar powder combination and binder jetting system were used [112].

The porosity of the samples measured by the Archimedes method, revealed a range of (33.6±1.5)% - (41.8±2.4)% (Figure 6-3), which demonstrated about 10% increase when the result was compared with the previous work of Sheydaeian and et. al on the effect of layer thickness variation [112]. In addition, 6% to 16% of increment in the porosity of the specimens with tailored closed-cells was obtained when the data is compared with the same results in S8. ANOVA single factor analysis of variance revealed a notable statistical difference among the specimens' porosity in general due to the effect of sacrificial polymer removal (Table 6-4). When the effect of the size of droplets was investigated (comparing S1 and S2 with 176 droplets), a p-value < 0.05 was achieved. However, for the cases in which the size of the droplets are similar but there is a variation in the droplets layout throughout the structures (S1 with 176 droplets, and S3 with 189 droplets), the difference was not significant. A similar trend was observed when an expected porosity (Table 6-5) was determined from Equation (6-1), since it was expected that the porosity was enhanced by 1.9 %, 0.8 % and 2.0 % in samples S1, S2, and S3, respectively. S4 demonstrated the lower level of porosity compared to the first three samples, as a result of the dramatic variation in the layer thickness (200 µm to 80 µm) [112]. As presented in Table 6-6, the range of calculated error between the

result of the experiment and mathematical calculation was < 5%, except in S1 (7.6%). This reveals the potential of employing the suggested analytical equation in this article as a method to estimate the porosity of the samples in the design stage by considering the role of each manufacturing parameter. The overall range of porosity in the samples after polymer removal is in close similarity to some of the data reported in the literature for the successful case of biomedical applications [49], [162], [104].

To evaluate the influence of selective control of binder saturation level on the designated layer of the samples, ANOVA analysis was conducted on the control samples (Table 6-5). However, the result showed a significant statistical difference between S5 to S8, but when only S5 or S6 was compared with S8, a p-value > 0.05 was achieved. This finding demonstrates that regardless of the binder injection level [163], only the sacrificial polymer can be a remarkable source of tailoring porosity variation in the designed samples when the layer thickness is constant.

The average porosity of samples S1, S3, S4, and S8 achieved from analyzing the µCT scan data demonstrates the similar trend in the variation of this parameter when compared with the data from the Archimedes method (Table 6-6). In addition, the difference between the ranges of the data from each method was less than 5%. The range of the pore size from analyzing the µCT scan data was notably varied when the peak of the max pore graphs for each sample was compared with the diameter of the droplets 0.39±0.07 µm from a previous study [74]. However, the better similarity with the reported data for the height of the polymer drops, from our previous study, (0.17 ± 0.02) µm was observed [74]. This trend in data corresponds to the pore size analysis method which was employed in this study: defining the pore diameter as the largest sphere that could fit within the pore, considering the non-spherical shape of the droplets. Although the distribution of the pores (Figure 6-5) and porosity (Figure 6-6) very well matched the similar parameters with respect to the design of the samples.

From the mechanical compression test, the range of Young's modulus and the Yield stress was determined as follows: 2.48±0.37 GPa –3.55±049 GPa and 107.65±18.14 MPa –145.75 ± 13.85 MPa, respectively (Figure 6-8 and Figure 6-9). The obtained data falls within the range similar to bone mechanical properties [164]. The mechanical properties of the specimens incorporating tailored closed pores revealed the significant range of decrement as follow: 7% to 22% in the Young's modulus and 3% to 28% in the Yield stress. The study of statistical variation between the data revealed a significant deviation (Table 6-4) in both parameters due to incorporating the effect of selective porosity and variation into layer thickness when S1 to S8 were studied. As presented in this table, the range of p-value < 0.05 for the Young's modulus was observed when S1 and S2 were compared. This finding can be supported by observing the same trend in the porosity of the mentioned specimens. The Yield stress appeared to have more sensitivity, when the

results of the analysis were compared to S1 to S4, with notable differences when the size of the droplets varied (S1 and S2). One can conclude that, although selectively increasing the porosity, by alternating the size of droplets, may not significantly affect the stiffness of the samples with large pores while reducing the strength of the samples and increasing the likelihood of the samples' failure [165]. The same conclusion can be derived when S1 and S3 are compared. The analytical estimation for the Young's modulus of sample S4 and S7, obtained by incorporating the data in Equation (3-6) [112], provides an error margin of 6.2% - 7.5% (Table 6-7). This, therefore, suggests the relevance of the proposed method for predicting the stiffness of the samples in the design stage based on the experimental data.

The SEM of the heat-treated samples denotes a sintering quality in terms of the sinter neck size similar to the previous studies (Figure 6-10-a). In addition, studying the failure region of the samples, after subjecting to the compression test, identifies the Ti powder sinter necks as a point of crack formation initiation (Figure 6-10-b) [166].

This study was focused on the impact of the selectively encapsulating the sacrificial photopolymer and then eliminating it from the final Ti samples throughout the heat treatment step, on the architectural features and mechanical properties of the specimens. The results of investigation suggest substantial differences in all those parameters when the polymer was involved in the manufacturing of the samples compared to the control samples. Moreover, the selective increase of the binder saturation level on the designated layer did not reveal any remarkable role in controlling the samples' properties. The addition of the polymer to the samples provided the pore size and distribution gradient within the samples which makes this method relevant in the context of bio-fabrication. Integrating the variable powder size, layer thickness, and sintering temperature, as well as the proposed method, can improve the implant architecture to mimic the exact bone structure and mechanical properties.

Future studies could be focused on incorporating these findings into the design of the heterogeneous cellular samples with tailored properties based on the application.

6.4 Conclusion

In this article, eight categories of Ti samples were additively manufactured, four of which included the polymer droplets deposited on the designated layers to increase the porosity locally, and four others studied as control samples. The assessment of the porosity of the samples through the Archimedes method revealed data ranging from (33.6±1.5)% to (41.8±2.4)% with more statistical sensitivity in the data with input parameters: the number and size of droplets as well as their distribution layout. Analyzing the µCT scan data demonstrates a close similarity between the porosity resulted from this method with the Archimedes approach. In addition, the maximum size of the pores with respect to the height of the samples presents the

proper number of the peaks in each part and at the corresponded layers with the embedded polymer. From the mechanical compression test, the Young's modulus and the Yield stress was obtained as follows: 2.48±0.37 GPa-3.55±0.49 GPa and 107.65±18.14 MPa-145.75±13.85 MPa, respectively. The porosity and stiffness of the specimens determined from the analytical equation show a 5 % discrepancy with the experimental results. The method presented here can be relevant in a vast range of applications when structures with selective closed-cells are applicable such as the manufacture of lightweight structures and orthopedic substitutes.

7 A new approach for fabrication of titanium-titanium boride periodic composite via hybrid additive manufacturing and pressure-less sintering

7.1 Introduction

Metal matrix composites (MMC) have become relevant on a widely diverse area of applications due to incorporating unique metallic properties into the structures which are enhanced with reinforcement elements [167][168]. To manufacture a successful MMC structure through in-situ processing, certain criteria must be satisfied in each step: material selection, material composition (reinforcement volume fraction), particle size, fabrication setup, and so on [169]. Among the wide range of MMC examples, titanium matrix composites (TMC) have been studied extensively in various industries, some of which include: aerospace, automotive, and biomedical [170]. The popularity of this group of composites is mainly attributed to the Ti properties such as high strength to weight ratio, thermal and oxidation resistance, and bio-compatibility, all in which are fortified through the addition of the filler properties: high thermal resistivity, wear, and fatigue resistance [171].

From several reinforcement materials introduced in Ti matrix, titanium di-boride (TiB_2) has displayed the most promising results with regard to stability in the chemical reaction between Ti and TiB_2, in addition to similarity in their thermal expansion coefficient [170], increasing mechanical stability. Some of the notable properties of TiB_2 include a high melting point, a high stiffness to density ratio, and hardness [172]. The chemical reaction between Ti and TiB_2 results in the formation of titanium boride (TiB) crystal [173]. The success in the synthesis step is influenced by sintering conditions [173], [174], the volume fraction of ceramic (TiB_2) [175], as well as the particles size [174]. The impact of each parameter on the growth of TiB has been studied thoroughly, by validating the morphology (whisker, plate, and cluster) and grain size [170]. Each of these parameters controls the properties of TMC such as stiffness, hardness, thermal conductivity, creep performance, etc. [175]. Although the majority of the studies in the literature have focused on Ti-TiB composites as an essential candidate for industrial applications, few studies demonstrated promising results in the biocompatibility of the composite while used in orthopedic implants and coatings [176]–[178].

Introducing additive manufacturing (AM), which is based on fashioning 3D objects through layer-by-layer construction, has created a promising path towards the fabrication of structures with complexity in topology and variation in materials. In recent years, the development of commercialized and open-source multi-materials 3D printers has been pushing the boundaries even further. Incorporating the vast range of materials selectively distributed within the architectures has resulted in a variety of designs and novel

applications [51]–[59]. Some of the methods proposed to facilitate manufacturing of multi-material as well as composite architectures include material extrusion [11], jet printing [12], stereolithography [13], and ultrasonic consolidations [14][15].

In powder-bed AM, structuring the multi-material object has been addressed by applying different methods based on the type of process. One way to enhance the structural properties is through applying bimodal powder containing matrix and reinforcement powder [16]–[20]. However, this approach for the fabrication of MMC can only be benefited from the AM ability to structure a complex geometry but from controlling the materials layout point of view, it is similar to that offered by other conventional methods. In the binder jetting method, injecting multiple liquid binders [60], in addition to retrofitting a system for selectively encapsulating solid particles [61] of two or more materials, has been suggested. In the present study, a binder jetting system in conjunction with material extrusion [10], [62] is employed to propose a new method for manufacturing TMC structures. TMC structures are composed of Ti matrix, which is manufactured through binder jetting, and TiB_2 reinforcement, which is encapsulated periodically within the matrix all in a single step processing.

To incorporate the ceramic (TiB_2) in matrix architecture, a highly loaded acrylic based ceramic-resin composite was developed. Manufacturing of ceramic resin has been widely applicable in the additive manufacturing of ceramic structures where the most studies have focused on their properties and applications in stereolithography [179]–[182]. The resin must demonstrate certain properties such as high volume fraction of ceramic, proper range of viscosity, UV curability, low shrinkage during curing maintaining dimensional accuracy, etc. [182]. In a material extrusion system, dispensability of the material is another factor which can be controlled by adjusting the viscosity [74].

The resin in this study consisted a UV curable polymer combing bisphenol-A ethoxylated diacrylate and cellulose acetate butyrate, which maintains the viscosity required to facilitate the dispensability of the resin [74]. TiB_2 powder particles were loaded in the proposed polymer and ceramic resin was applied in the material extrusion system to encapsulate ceramic resin droplets periodically within the Ti matrix. The heat treatment step was incorporated into Ti- TiB_2 composite processing. This combination not only promotes the solid-state sintering between matrix particles but also facilitates the chemical reaction between Ti and TiB_2, yielding to the TiB formation. Our previous study revealed a low decomposition temperature (400°C) for the polymeric elements of resin, which suggests that the polymer and its residual carbon are fully removed from the Ti- TiB_2 reaction zone due to a comparable higher sintering temperature of composite (> 1000 °C) [74].

To fabricate the samples, two different reinforcement volume fractions as well as two sintering protocols [61], [174] were selected. To this end, six categories of samples were designed and manufactured by the proposed system. Among the different methods of sintering proposed in the literature [170], pressure-less sintering (known as gravity sintering too) was selected due to the design and limited integrity of green samples collected from the binder jetting AM approach. The sintering protocols were differed based on the highest sintering temperatures: a maximum of 1200 °C [174], and a maximum of 1400 °C [112].

Several characterization steps were conducted to investigate the influence of the variable input process parameters (volume fraction, sintering temperature) on the physical properties. X-ray diffraction (XRD) accompanied with scanning electron microscopy (SEM) was performed to evaluate the formation and quality of TiB_w crystals in samples that went under the heat treatment protocols. In addition, dimensional deviations of the samples were calculated for each sintering protocol. The effect of the same variable and of the volume fraction of the reinforcement were studied through the porosity assessment performed by the Archimedes method and micro computational tomography (µCT), and mechanical strength of composite samples. Moreover, two analytical equations were proposed to correlate porosity and stiffness of the designed composites to the process input variables of the interest (temperature and volume fraction).

7.2 Materials, methods, and results

7.2.1 Matrix material

The matrix material has been detailed in chapter 3 (3.2.1).

7.2.2 Highly loaded ceramic resin

To prepare the reinforcement, a ceramic resin was developed from 67 wt.% of titanium di-boride (TiB_2) particles [powder, < 10 µm, Sigma-Aldrich, Oakville, Canada] loaded on a UV curable polymeric liquid to facilitate the material extrusion process. Figure 7-1 shows the SEM image of a sample of the purchased TiB_2 powder. The polymeric part of the resin included 19 wt.% bisphenol-A ethoxylated diacrylate (BAE) [Ebecryl 150, Cytec, NJ, USA], 2 wt.% cellulose acetate butyrate (CAB) [Sigma-Aldrich, Oakville, Canada], acetone and 2 wt. % Phenylbis (PI) (2,4,6-trimethylbenzoyl) phosphine oxide (Irgacure 819) [Sigma-Aldrich, Oakville, Canada]. Next, the resin was prepared by mixing all compounds for 30 minutes. The previous study showed the dramatic rate of decomposition for the proposed acrylic polymer near 400 °C [74]. The low decomposition temperature promised a complete removal of the polymer from final TMC structures subjected to a high-temperature heat treatment.

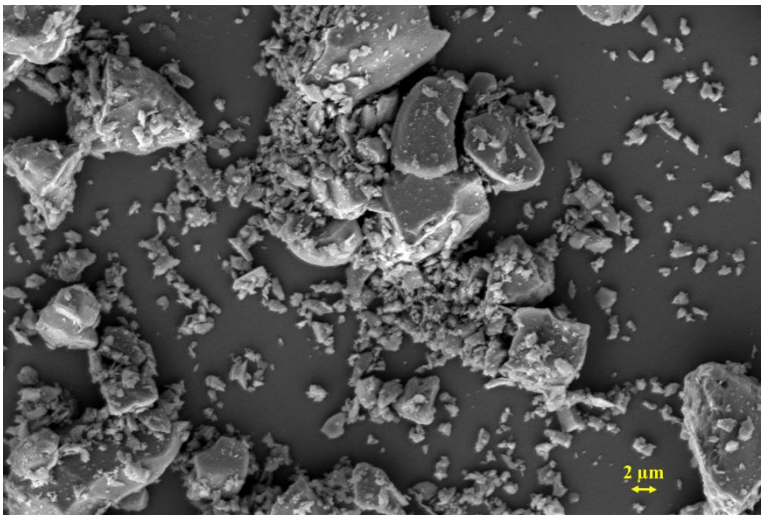

Figure 7-1 SEM images of the purchased TiB2 particles

Prior to loading the TiB_2 resin on the material extrusion system, ULTIMUS ™ V high precision dispenser EFD [NORDSON Company, MA, USA], the dispensability of the developed resin was investigated through studying the shear thinning behavior of the liquid. Therefore, the viscosity of the material mixture was measured by employing a high shear viscometer [BROOKFIELD CAP 2000, Brookfield AMETEK, MA, USA] (Figure 7-2) through the steps detailed elsewhere [74].

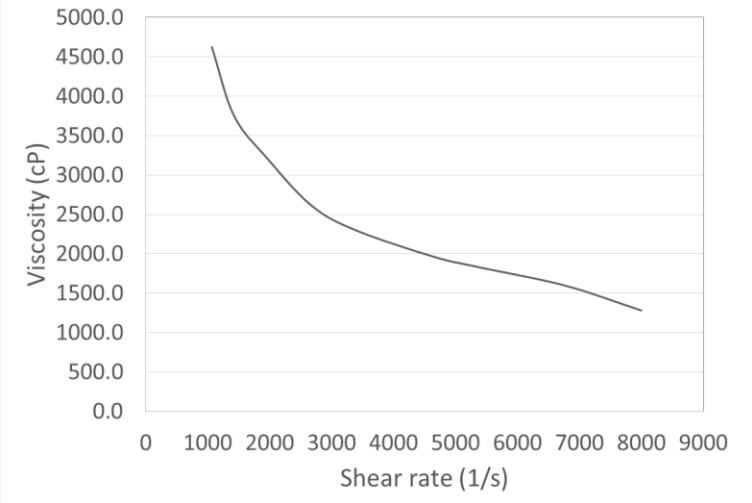

Figure 7-2 Viscosity of the highly loaded ceramic resin

7.2.3 Additive manufacturing of specimens

For additive manufacturing of composite structures, the six groups of samples each including eight specimens were first devised. The matrix was designed in cylindrical geometry 5 mm in diameter and 8 mm in height [SolidWorks Corp., Concord, MA], to follow ASTM E9-09 [95] for the compression test. Then, the morphology of the ceramic resin droplets was evaluated as a relevant factor for selecting

appropriate layer thickness [74]. Therefore, the resin was loaded on the extrusion system and droplets were injected on a Ti substrate by applying the following system input parameters: 200 µm needle, 200 kPa pressure and 0.1 sec for dispensing time (Figure 7-3). Comparing the droplets morphology (average diameter = 0.48±0.07 µm and height = 0.23±0.04 µm) with those in our previous studies [62], [74] suggests a layer thickness of 200 µm as an appropriate selection.

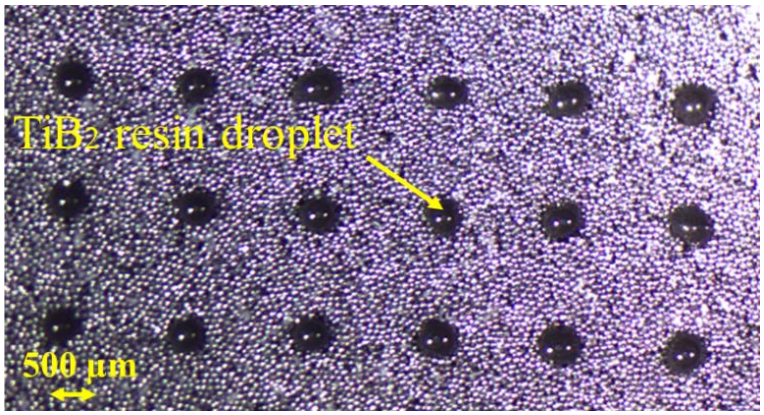

Figure 7-3 Test sample demonstrating the ceramic resin pattern after polymerization on Ti substrate

Table 7-1 Design description for the composite samples

Sample	Number of droplets per layer (m)	Number of the buffer layers (n)	Maximum sintering temperature
T1	9	2	1400
T2	9	4	1400
T3	-	-	1400
T4	9	2	1200
T5	9	4	1200
T6	-	-	1200

In the design of the TMC samples (Table 7-1), the influence of ceramic volume fraction was investigated by dispensing a fixed number of droplets (nine) at the designated Ti layer and varying the layers layout and distribution within the parts (Figure 7-4). The reinforced layers were incorporated into the design as follows: dispensing the resin on every 2 layers (Figure 7-4-a), dispensing it on every 4 layers (Figure 7-4-b), and standard samples with an only matrix material (T3 and T6). Ti layers with no reinforcements are referred to as buffer layers in Table 7-1. Figure 7-4-c shows the layout of the ceramic droplets dispensed on the designated layers of matrix.

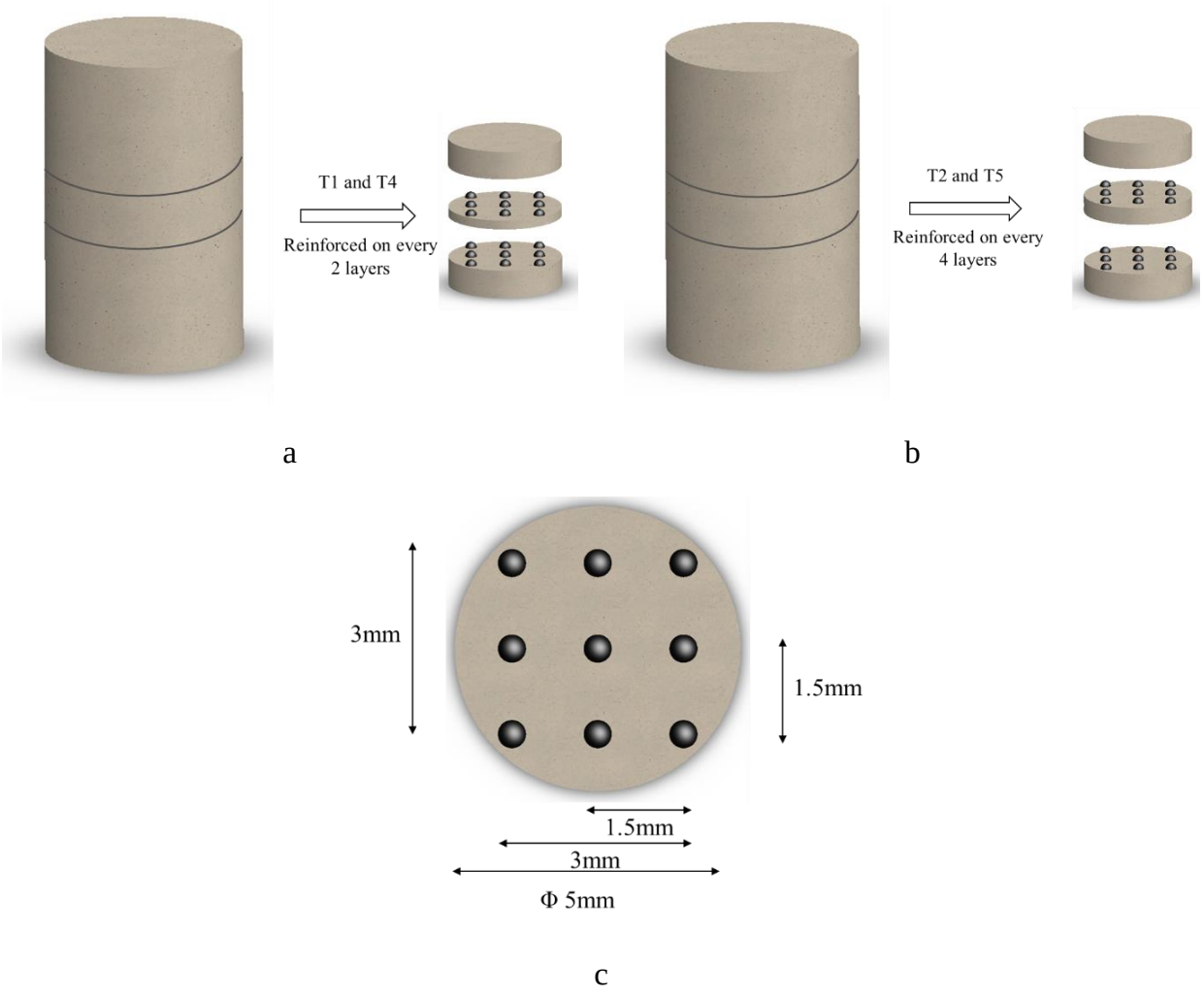

Figure 7-4 Schematic of the design of the TMC composite samples with different ceramic volume fraction (a and b) and the ceramic droplets layout

In the manufacturing steps, the first 4 layers of the samples were structured through binder jetting. Then, in the layers designated for the encapsulating resin, TiB_2 resin droplets were extruded and the binder (Zb60) was injected twice [74]. After this step, a proper number of buffer layers, based on the design (Table 7-1), was added to the parts by the AM system. Afterward, steps 2 and 3 were repeated continuously to structure the cylinders with 8 mm in height. The details of AM setups have been explained elsewhere [62]. Figure 7-5 shows an example of AM of a Ti layer embedded with TiB_2 resins droplets.

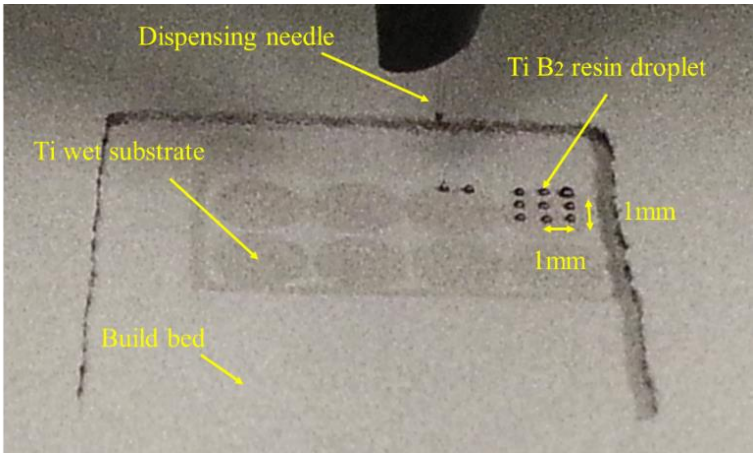

Figure 7-5 Sample of additive manufacturing one layer of composite with loaded ceramic resin droplets

To approximate the volume fraction of ceramic in the design of composite samples, the volume of the droplets was calculated by calculating a volume of a hemisphere with 500 µm diameter (Figure 7-3). The average of 4% and 2% was obtained when droplets were embedded in every 2 layers (T1 and T4) and every 4 layers (T2 and T5), respectively.

7.2.4 Effect of sintering protocol on chemical composition of matrix-ceramic reaction zone

In addition to the volume fraction of TiB_2, the influence of the sintering protocol on the formation of TiB-whisker (TiB_w), by emphasizing the maximum temperature, was incorporated as another input parameter into the process (Table 7-1). Therefore, two different sintering curves were proposed (Figure 7-6). The first part of both graphs (up to 1000°C, heating rate 10°C/min) was designed to meet the required steps for removing the organic elements from the structure and initiating the sintering step [33]. Next, in the first graph, the temperature was raised up to 1200°C [174] and samples were left at this temperature for three hours. In the second proposed heat treatment process, the temperature was raised from 1000°C to 1400°C allowing the specimens to continue the solid-state sintering at the same temperature for three hours, similar to our previous work [74]. The sintering process was performed in a MTV high-temperature tube furnace [GSL-1500X-50, Richmond, CA]. In the both sintering curves, the heating rate was set at 5°C/min after 1000°C and the sintering was performed in the Argon environment to protect the samples from oxidation. After sintering, samples were left in the furnace to complete the cooling step in an Argon atmosphere and thus preventing the oxidation.

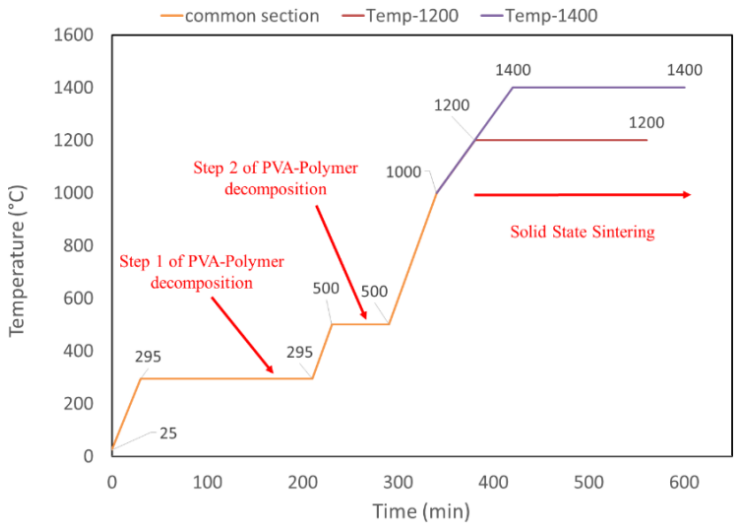

Figure 7-6 Proposed pressure-less sintering protocols

The formation of TiB crystalline structures was studied through X-ray diffraction (XRD) on the test samples (Figure 7-3) after applying the sintering protocols. The analysis was performed on a D8 DISCOVER diffractometer system [BRUKER, USA]. The same test was also conducted on both Ti and TiB_2 powder particles, supplied from manufacturers, as a reference to detect and compare the peaks associated with Ti or TiB_2 crystals. To distinguish the trace of each element in the corresponding peaks, the results of the study were compared with the data reported in the literature [173], [183], [184]. In addition, the volume fraction of formed TiB as a function of the sintering temperature was evaluated based on the direct comparison X-ray method [185].

Figure 7-7 shows the results. Due to the difference in the range of intensity of each measurement, the results were normalized in demonstrating the data for 2θ ranging from 25º to 50º, since the results were not significant for the rest of the angle spectrum. The associated peaks indicate the formation of TiB crystal marked in Figure 7-7. As shown, the sample sintered at 1400°C (Figure 7-7-b) demonstrated the higher intensity in the TiB peaks. In both cases, the Ti peaks are also observable.

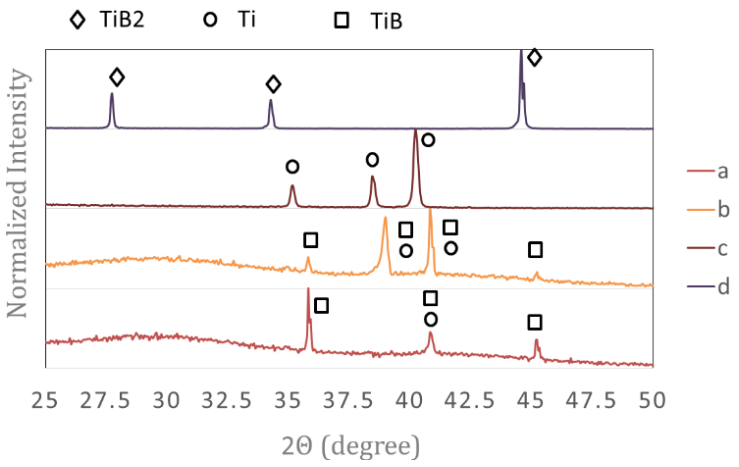

Figure 7-7 X-ray diffractometer results for different sintering temperature (a-1200ºC, b-1400ºC) and purchased powders (c: Ti and d: TiB_2)

The microstructure of the additive manufactured samples was studied through scanning electron microscopy (SEM) [ULTRA Plus, Zeiss, Germany], with 10 kV voltage, and the following parameters were evaluated: formation, growth and size of TiB_w, as well as the sintering quality of the three main elements (Ti, TiB_2, TiB_w) in the matrix-ceramic interface. To perform this step, the sintered specimens (Table 7-1) were broken into pieces by subjecting them to the mechanical compression test (Figure 7-8).

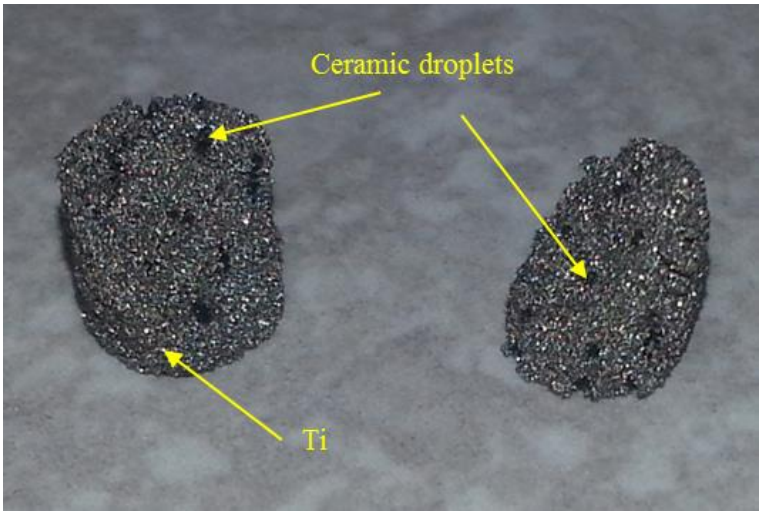

Figure 7-8 One of the composite samples broken for SEM analysis

Figure 7-9 shows the microstructure of the reaction zone in the samples subjected to different sintering protocols (Figure 7-6). The qualitative analysis of the SEM figures suggests a higher intensity for the formation of TiB_w for those samples sintered up to 1400ºC.

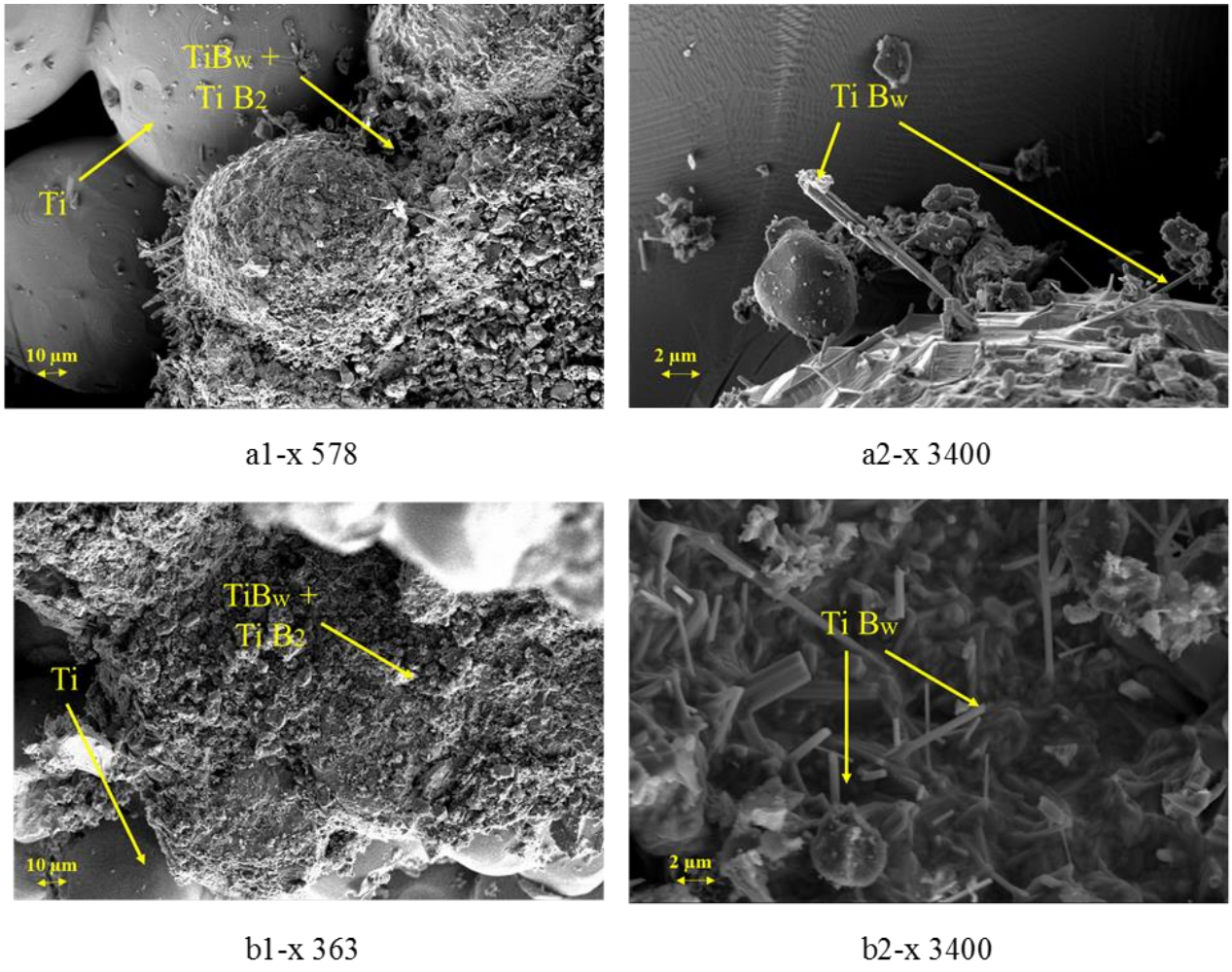

Figure 7-9 SEM images of Ti-TiB_2 reaction zone as a function of sintering temperature. a1 and a2) at 1200°C, b1 and b2) at 1400°C

7.2.5 Effect of sintering on the dimensional deviation of samples

The effect of sintering on the geometrical features of the samples was studied through the steps detailed in section 3.2.3. The following range of dimensional deviations for the TMC samples was obtained: (1.4±0.8) % - (2.7±0.9) % in diameter and (1.3±0.5) % - (5.6±0.8) % in height (Table 7-2). ANOVA analysis did not show any significant difference in the diametrical shrinkage. However, shrinkage in height of the samples revealed a notable variation in the data with regard to the temperature. The same trend was observed in the case of comparing T1 to T3 (a different processes parameter and similar sintering protocol).

Table 7-2 Dimensional deviations of the composite samples

Sample	Diameter Shrinkage (%)	Height Shrinkage (%)
T1	2.7±0.9	4.3±0.5
T2	2.0±1.1	5.6±0.8
T3	2.5±0.6	5.0±0.3
T4	1.7±1.3	2.1±0.7
T5	1.4±0.8	1.8±1.0
T6	1.9±0.4	1.3±0.5

A similar analysis was performed on the test samples (Figure 7-3) to investigate the influence of temperature and polymer removal on the geometrical features of the ceramic droplets. Measurement of the ceramic patterns' geometrical features dispensed on the test samples (Figure 7-3), before and after heat treatment, demonstrated an average shrinkage of 4.7% and 16.5% in diameter, 1.0% and 17.5% in height when different sintering temperatures were applied: 1200ºC and 1400ºC, respectively.

7.2.6 Porosity measurement

The porosity of the Ti samples after removing the sacrificial photopolymer during heat treatment was determined by applying the Archimedes method (ASTM B311 [96] & C373 [97]). The detail of the experiments is presented in section 3.2.4. The porosity of samples measured by the Archimedes method demonstrated a minimum porosity of (28.3±1.4) % in T1 and a maximum of (38.3±2.0) % in T6 (Figure 7-10).

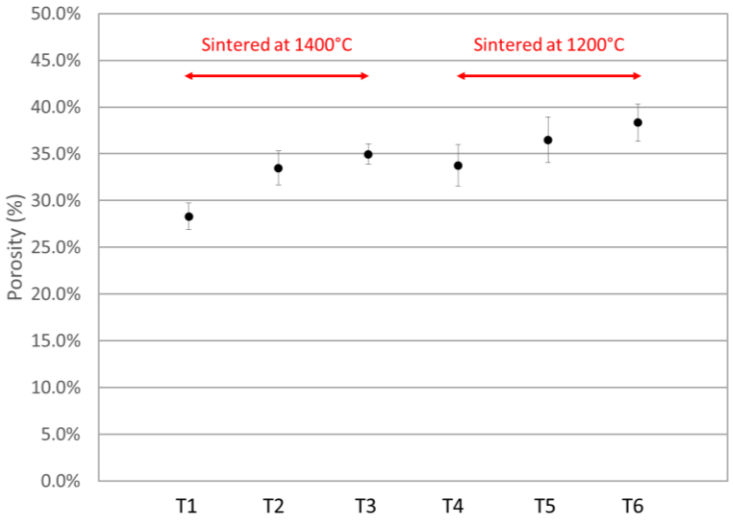

Figure 7-10 Porosity of the samples measured by the Archimedes method

To evaluate the role of manufacturing parameters as well as the sintering protocol, ANOVA analysis was performed; it revealed the significant influence of both parameters on the porosity.

To evaluate the effect of encapsulating TiB_2 resin, Equation (7-1) was proposed. It correlates the porosity of TMC structured ($P_{expected}$) with the porosity of the control samples ($P_{standard}$), sintered with the same protocol as the TMC parts, and with the volume fraction of resin (V_{resin}). The porosity of T1, T2, T4 and T5 was determined from this equation and compared with the similar data obtained from the Archimedes method.

$$P_{expected} = P_{standard} - V_{resin} \quad \textbf{(7-1)}$$

Applying this equation indicates an error margin of (0.6% - 9.6%) between the porosity measured from the experiment ($P_{Archemidus}$) and the proposed equation ($P_{expected}$), among the selected samples with encapsulated TiB_2 ceramic resin (Table 7-3).

Table 7-3 Comparing the porosity of the samples achieved from the Archimedes, Equation 5 and µCT

Sample	$P_{expected}$	$P_{Archemidus}$	Error ($P_{expected}$, $P_{Archemidus}$)	$P_{µCT}$	Error ($P_{µCT}$, $P_{Archemidus}$)	Droplet density (µCT)
T1	31.0 %	28.3 %	9.6 %	32.7 %	13.5 %	5.6 %
T2	32.9 %	33.5 %	1.7 %	34.6 %	3.2 %	2.9 %
T4	34.4 %	33.8 %	1.8 %	NA	NA	NA
T5	36.3 %	36.5 %	0.6 %	40.8 %	10.5 %	3.3 %

For µCT, one specimens from category T1, T2 and T5 was selected to investigate the effect of ceramic volume fraction and sintering temperature on the micro-structure. The samples were imaged using a Versa 520 [Zeiss, Germany] nano-scale X-ray computed tomography (nano-CT) instrument at 120 kV and 3.81 µm voxel resolution. The average porosity and the porosity distribution as a function of the height were evaluated. In addition, one specimen from each test sample was prepared for the nano-CT to observe the 3D interface of ceramic and matrix powders. The setup was as follow: 700 nm voxel resolution and 40 kV.

Overall porosity of the samples calculated from µCT demonstrates the range of 3.2% to 13.5% of error when the results were compared with the Archimedes data (Table 7-3). In addition, from assessing the µCT data, the effect of incorporating ceramic droplets into the design of the samples on the specimen's densification was obtained (Figure 7-11).

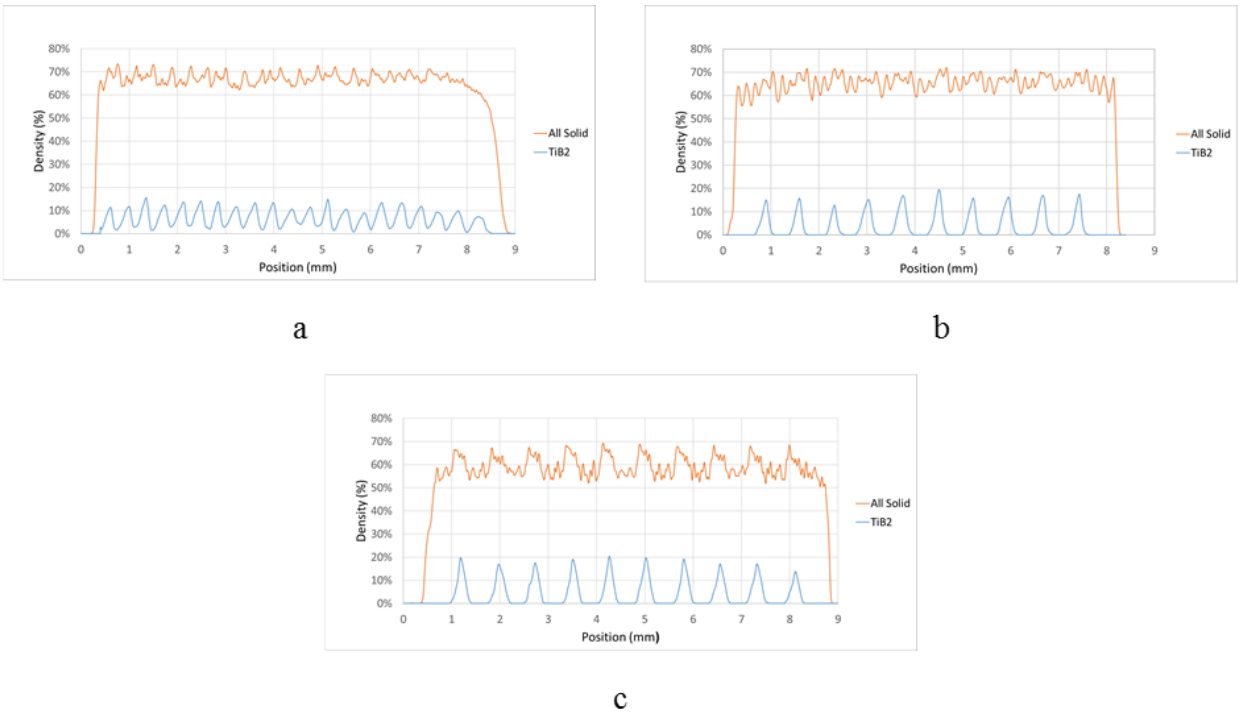

Figure 7-11 Distribution of density of solid section (Ti + ceramic) and ceramic itself from analyzing µCT data. a) T1, b) T2 and c) T3.

Evaluating the results revealed that the average droplet density (volume fraction) varies from 2.9% to 5.6% (Table 7-3). Figure 7-12 shows a 3D construction of the ceramic drop and matrix from nano-CT.

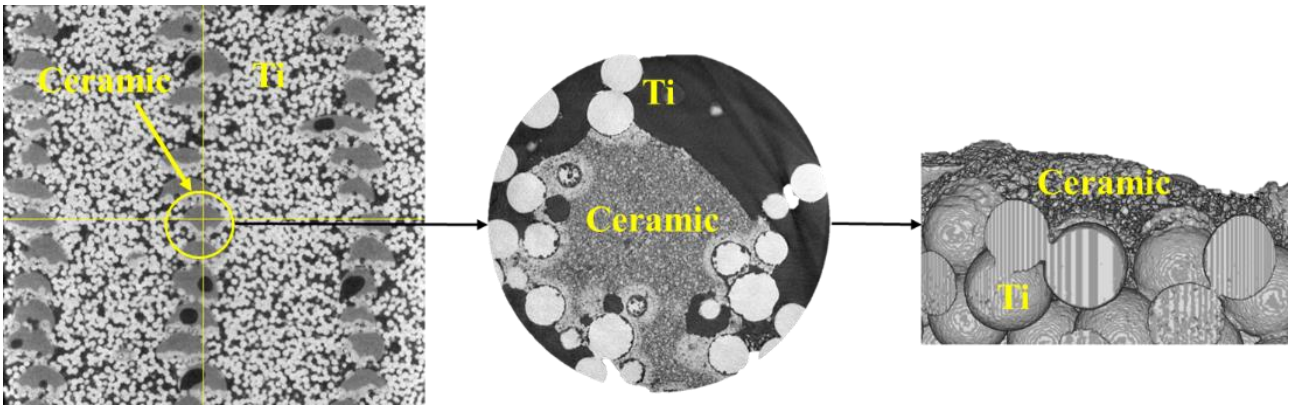

Figure 7-12 A sample of 3D image construction of matrix and ceramic reinforcement form nano-CT

7.2.7 Mechanical tests

From each category, seven samples were selected and subjected to the compression test by employing a compression test. The test setup is explained in chapter 3 (3.2.5). Figure 7-13 and Figure 7-14 the range of Young's modulus and Yield stress of the specimens in Table 7-1, respectively. As shown, the stiffness and mechanical strength of the samples were enhanced in the reinforced samples with TiB_2 droplets. From

ANOVA analysis, a significant variation of the Young's modulus of samples was suggested when all specimens and those sintered at the same temperature were compared. While in the case of the Yield stress this trend was observed only when all samples were compared.

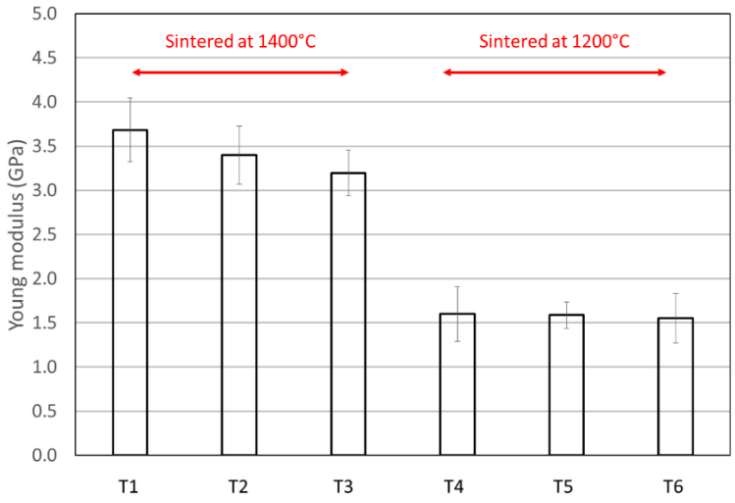

Figure 7-13 The Young modulus of the samples

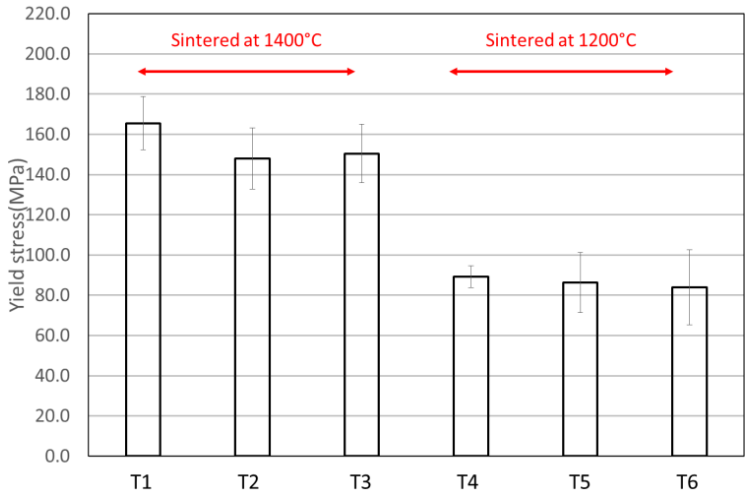

Figure 7-14 The Yield stress of the samples

In addition, the hardness of the test samples (Figure 7-15) was measured using the indentation test by selecting Vickers indenter [Nanovea-M1 indentation - US]. Prior to the experiment, each sample was prepared according to ASTM B 933-16 [186]. In each sample, three to five points from Ti substrate and ceramic patterns were selected and the experiments were conducted with the following setting: a maximum load of 3 N with the rate of 6 N/min for loading-unloading, approaching the speed of 3 µm/min, and 20 µN for the contact load.

Figure 7-15-b demonstrates the result of the Vickers hardness test on the test samples based on the sintering temperature and the material (Ti, ceramic). As shown, the maximum temperature directly influences the results in both the metallic and ceramic sections of the specimens with p-value < 0.05 from ANOVA. The trace of the indenter tip on the ceramic pattern is seen in Figure 7-15-a.

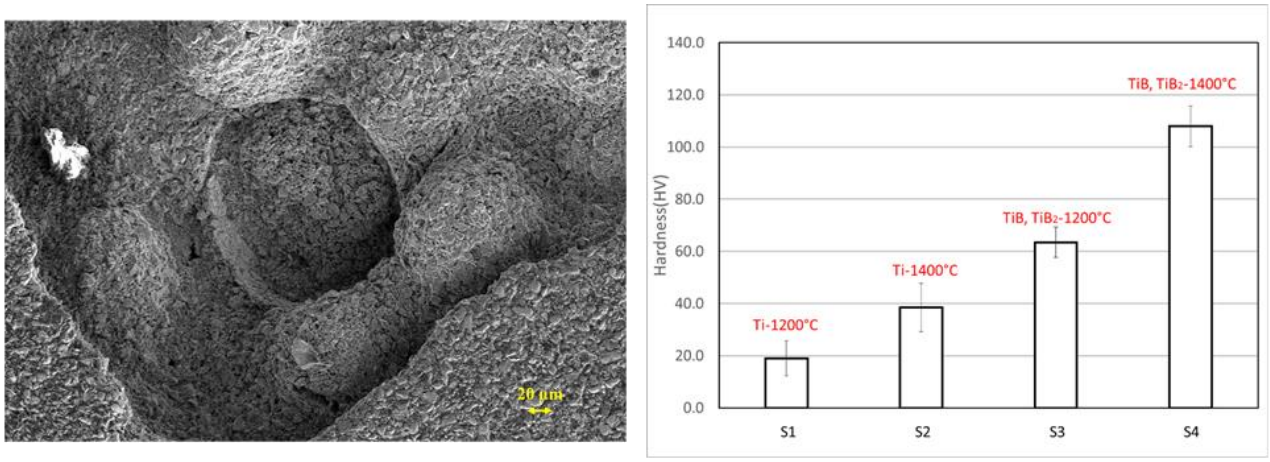

Figure 7-15 The Vickers hardness of the test samples (Error! Reference source not found.**). a) shows the trace of indenter tips on the ceramic patterns b) demonstrates the results of hardness tests for each material and based on sintering temperature**

Equations (7-2) and (7-3) were proposed to estimate the stiffness of the TMC samples in correlation with the design, volume fraction, and sintering protocol. Considering the composite system proposed in this work, the following equations were extracted to estimate modulus of elasticity in samples reinforced with every four layers (E1), and on every two layers (E2). In E1, the structure of composite can be divided into the 10 sections each made of three layers of Ti and one layer of Ti+composite while in E2, the structure combines 21 sections with one layer of matrix and one layer of matrix+ceramic in addition to the five extra layers of Ti distributed in the top and bottom sections of the sample (Table 7-1 and Figure 7-4 on the design of the samples)

$$E_1 = \frac{4E_m * E_c}{E_m + 3E_c} \qquad \textbf{(7-2)}$$

$$E_2 = \frac{47E_1 * E_m}{42E_m + 5E_1} \qquad \textbf{(7-3)}$$

In these equations, E_m is denoted the stiffness of Ti layers without reinforcement extracted from the Young's modulus of test samples, and E_c corresponds to the layers including Ti and ceramic resin. E_c was determined by applying Equation (7-4) [187].

$$E_c = E_r * V_r + E_m * (1 - V_r) \quad \textbf{(7-4)}$$

In this equation, *Er* is the stiffness of the resin droplets after sintering and extracted from the hardness test on the ceramic patterns. When Young's modulus of standard Ti samples from compression test and the Young's modulus of the ceramic patterns from the indentation was introduced to Equations (7-2), (7-3) and (7-4) as E_m and E_r , respectively the following error margins were achieved: T1: 27%, T2: 14%, T4: 38% and T5: 17% (Table 7-4).

Table 7-4 Comparing the stiffness of the composite samples from experiments and Equations 5-7

Sample	E_r (indentation) GPa	$E_{calculated}$ (E1, E2) GPa	$E_{experimental}$ GPa	Error (%)
T1	106	4.7	3.7	27
T2	106	3.9	3.4	14
T4	43	2.2	1.6	38
T5	43	1.9	1.6	17

7.3 Discussion

In this study, Ti-TiB_w metal matrix composites were structured by combining two methods of additive manufacturing: binder jetting and material extrusion. The binder jetting approach was employed to fabricate the main Ti matrix, while it was reinforced periodically through dispensing the highly loaded TiB_2 resin droplets by the material extrusion system. The specimens were subjected to different heat treatment protocols for sintering. Afterward, the influence of input parameters, including sintering temperature and volume fraction of TiB_2 on the specimen properties was investigated.

Analysis of the normalized data obtained from XRD displayed the formation of TiB resulting from the reaction between Ti powder and TiB_2 resin particles (Figure 7-7). As shown in this figure, the correlated peaks in the TiB formation have the highest relative intensity in Sample b (sintered up to 1400°C) compared to Sample a (sintered up to 1200°C). This finding reveals the direct correspondence between the sintering temperature and growth of TiB, as suggested in the literature [188]. The direct comparison method [185] corroborates a similar conclusion on the influence of the maximum sintering temperature and the TiB volume fraction while comparing the normalized intensities correlated to the similar phase peaks between Samples a and b (Figure 7-7).

Figure 7-9 illustrates the internal structure and powder morphology of some of the samples (Table 7-1) with a similar composite design and variation in the sintering temperature. The growth of TiB_w in the Ti-TiB_2 (resin droplet) reaction zone is identified in Figure 7-9 (a-2 and b-2). As seen in these figures, the colonies of TiB_w with shorter whiskers were produced at a low sintering temperature (1200°C) compared to sintering up to 1400°C [170]. Studying the growth direction showed the whiskers' tendency to grow from the surface of ceramic droplets to the nearest Ti particles in the metal-ceramic interface. In addition to Ti and TiB particles, the trace of TiB_2 can also be observed in Figure 7-9 by analyzing the middle section of resin droplets. However, the trace of TiB_2 was not detected in the XRD analysis which is attributed to the location of TiB_2 in the testing samples (Figure 7-3) as well as the limited depth of X-ray penetration compared to the droplets size (average diameter = 0.48±0.07 μm and height = 0.23±0.04 μm). The existence of TiB_2 particles in the SEM images can be explained by the relatively high ratio of the size of droplets and Ti powder particles in the reaction zone. This increases the concentration of TiB_2 and limits the Ti-TiB_2 interfacing required to produce TiB_w [173], [185], even when the overall volume fraction of the reinforcement element is very low (less than 4%) in the design of the samples. Therefore, the TiB_2 particles, which were more located in the middle section of the droplets, were only sintered to their surrounding TiB_2 particles.

The dimensional deviation of the sintered composite samples (Table 7-1) demonstrated a higher range of shrinkage in the height of samples compared to their diameter (Table 7-2). This result is attributed to the orientation of the samples in the manufacturing and heat treatment step [84]. In addition, as the sintering temperature was raised, the dimensional deviation between the height of green samples and the sintered ones increased as a direct influence of temperature in forming sinter necks between the powder particles [123]. ANOVA analysis revealed a higher variation among the data for the samples sintered at the higher temperature (1400 °C) with lower shrinkage in T1 infiltrated by ceramic resin on every two layers (higher TiB_2 volume fraction). One can conclude, although there is no significant variation among thermal properties of Ti and TiB_2 [175], that the existence of the droplets acted as a high-density spacer [62], [112] between each set of buffer layers and reduced the contact between the Ti layers. A Similar trend in the dimensional deviation of ceramic patterns as a function of temperature was observed with more noticeable variation in their diameter compare to the height. The findings can result from the difference in the height of the diameter ratio, which improves the rate of reaction in the radial direction.

The overall porosity ranging from (28.3±1.4)% to (38.3±2.0)% was obtained through the data obtained from the Archimedes method (Figure 7-10). As seen, a direct correlation between the temperature rise and the density of the specimens exists [123]. This finding is consistent with a similar trend observed in the geometrical features of the samples. Next, this result was studied through evaluating the effect of the

ceramic reinforcement volume fraction on the porosity in the specimens, which were sintered with a similar protocol. Comparing the data in the first section of the graph (sintered up to 1400ºC) revealed the direct influence of this parameter on the reduction of porosity by dramatic decrement (19.0%) when T1 and T3 were compared, while only small volume fraction of ceramic material (< 4%) was added to the matrix. However, this improvement in the structural integrity of the samples when the porosity of T2 and T3 was evaluated was smaller: 4.5% reduction for the samples with less than 2% of ceramic. From these results, one can conclude that an increase in the volume fraction not only enhances the density of structure in designated reinforced section of the matrix, but also it could suggest the formation of TiB_w as a result of boron spread through the matrix porous media in the sintering step. This may result in the possibility of sporadic TiB_w formation within the matrix, which creates more bonding between the dissimilar particles of the composite medium. A similar conclusion may draw when specimens in the second section of the graph (sintered at 1200ºC) are studied. ANOVA analysis corroborates our finding by demonstrating a significant variation among the data when all of the samples were compared as well as comparing the results for each section of Figure 7-10 to evaluate the influence of ceramic volume fraction.

Comparing the result of experiments for samples reinforced with TiB_2 resin and the data from Equation (7-1) revealed less than 10% difference among the data (Table 7-3). It should be noted that the porosity of the droplet itself in addition to the likelihood of TiB formation on random locations of the samples was not considered in the proposed equation because of the difficulty in the measurement of these factors, which can explain the discrepancies. Analyzing the data from μCT (Table 7-3) demonstrated a close likeliness among the results and the ones obtained for T1 and T2 from Equation (7-1). However, these data demonstrated the higher range of variation (3.2%-13.5%) when compared with the Archimedes which is mostly correlated to the difference in the number of specimens subjected to each test: eight per category in the Archimedes and one per category for the μCT.

Moreover, the average density of the droplets in the matrix structures revealed the range of (2.9%-3.3%), in specimens with embedded ceramic on every four layers, and 5.6% when Ti matrix was reinforced in a two-layer pattern. This funding presented a range of 1% variation with the initial estimation of the volume fraction of ceramic within the reinforced architecture. As shown in Figure 7-11, the density of the Ti layers with encapsulated ceramic increased up to 10% in each correlated peak.

The data from mechanical compression test revealed a range of 1.6±0.2 GPa to 3.7±0.4 GPa and 83.9 ±18.7 MPa to 165±13.2 MPa for the Young's modulus and Yield stress of the specimens, respectively. ANOVA analysis demonstrated significant differences among the results when all categories were analyzed, which shows the notable influence of the sintering temperature on the structural integrity and therefore the

mechanical strength of the parts [123]. In addition, as previously indicated, the data from analyzing SEM and XRD suggested that the temperature was directly associated with the volume fraction, size, and morphology of TiB_w which affects the enhancement of the corresponding mechanical properties [175]. When the influence of reinforcement volume fraction was evaluated for those samples in which a similar sintering protocol was applied, the stiffness of the samples demonstrated a higher sensitivity (p-value < 0.05) compared to their strength. Comparing the data in the first section of Figure 7-13 (1400ºC) revealed a notable improvement in the stiffness of the reinforced samples, even with adding a small percentage of TiB_2 ceramic: 15.2% in T1 (< 4% ceramic) and 6.4% in T2 (< 2% ceramic). The observed trend among the results supports a similar trend attained in the porosity of the specimens and what is suggested in the literature [170]. When samples in the second group (1200ºC) were studied, the enhancement in the similar mechanical property of the reinforced samples compared to the control one (T6) was observed as follow: 3.2% and 2.3% in stiffness of T4 and T5, respectively. The lower percentage of improvement is associated with the lower sintering temperature, which in addition to decreasing the integrity of Ti matrix, reduced the likelihood of TiB_w formation and growth, as mentioned previously.

As shown in Figure 7-15-b, the Vickers hardness of each material (matrix, ceramic) directly influenced through the increase in the sintering temperature. This is correlated to the effect of the temperature in the formation and the size of sinter necks as well as the increase in the possibility of TiB_w growth in the ceramic section of the graph [173]. The error margins of the data obtained from the experiments and proposed equations demonstrated the range of 14%-38%. This data suggests the further investigations are required in the different steps including the hardness test, sample preparation as well as employing numerical methods to predict the mechanical performance of the composites.

The method studied in this article and the obtained data suggest a practical way to engineer the periodic MMC composite structures with tailored properties, which can be obtained through the controllability of the morphology and layout in which the reinforcement material is incorporated. The substantial improvement in the properties of TMC specimens compared to the low volume fraction of ceramic corroborates the relevance of the applied method even when pressure-less sintering was selected in a lower range of temperature compared to what previously was suggested for the success of the reaction process [172]. A similar approach in addition to polymeric resin base can be applied to manufacturing other MMC with periodic structures from different materials.

Future work can focus on the development of TMC samples, with a different range of matrix particle size, reinforced with the variable volume fraction of developed highly loaded ceramic resin through alternating the size of droplets, a number of droplets per layer, different droplet arrangement, and number of layers

embedded with resin. The variation in each of these parameters can be resulted in the composite structures with tailored properties and based on the application. In addition, other ceramic materials or metal matrices can be proposed as the raw materials for the process.

7.4 Conclusions

This study has disclosed the development of a novel approach and material for fabricating Ti-TiB_w metal matrix periodic composite through the conjunction of binder jetting and the material extrusion AM methods. This study also proposed two pressure-less sintering protocols in addition to the two alternative composite designs in which the volume fraction of embedded ceramic was varied. The data revealed the direct influence of each of the input parameters on enhancing the relevant properties of samples, such as structural integrity and mechanical properties (e.g., strength, stiffness, and hardness). The increase in the sintering temperature (1400°C) resulted in the highest rate of success in the formation and growth of the TiB_w in Ti and TiB_2 interaction zone in addition to improving the structural integrity of Ti matrix through increasing the size of the sinter necks. When only the effect of ceramic volume fraction was compared among the specimens, a range of 1.6±0.2 GPa-3.7±0.4 GPa and 83.9±18.7 MPa-165±13.2 MPa for the Young's modulus and Yield stress of the specimens was achieved, respectively. The result indicated a significant improvement of 6.4% to 15.2% in the stiffness of composite compared to the similar property in the matrix, where a small fraction of reinforcement was only added: 2% and 4%, respectively.

Due to the substantial improvement in the properties of TMC specimens compared to the low volume fraction of ceramic, applied sintering method, and temperature; the proposed methodology may be a useful tool for the fabrication of composite structures requiring more complexity and control in the distribution and morphology of the reinforcement.

8 Conclusions and Future Work

8.1 Summary

Additive manufacturing has created a promising path for the fabrication of structures with complexity in the topology and variation in the material. In the recent years, the development of commercialized and open-source multi-materials 3D printers has been pushing the boundaries even further. This unique AM feature that allows us to selectively distribute a vast range of materials within the structures has resulted in a variety of designs and novel applications. One such an example is to architecture functionally graded structures and composite materials appropriate for many applications. Some essential requirements for the use of AM or other conventional methods with respect to the creation of heterogeneous structures are control of the size and distribution of the pores in each layer, the ability to create closed internal channels/voids, plus the feasibility of introducing multiple materials periodically within the architecture.

To attain the design criteria, studying different parameters involved in the process and selectively encapsulating materials within the designated layers during manufacturing were suggested and explored in this research.

From different process parameters, the effect of layer thickness and functional variation of binder saturation level were studied. Then a system for the selective encapsulation of solid particles within the layers of powder was proposed and developed. The performance of the system was evaluated as a potential method of manufacturing cellular titanium structures. Next, an application of a hybrid AM system, integrating binder jetting and material extrusion, was explored to form graded cellular solids. A proper polymeric sacrificial resin was developed to attain the green specimens' quality and dimensional accuracy in the morphology of the encapsulated pores. The statistical significance of employing this method was explored on the mechanical and structural properties of titanium structures.

Additionally, a novel approach for developing titanium matrix composites with the hybrid AM process was introduced. A highly loaded ceramic resin was designed and a pressure-less sintering protocol was adapted to the process. The quality of the composites with graded periodic reinforcements was determined and the results were discussed.

Based on the design and presented a range of the data, the proposed methodologies can be deployed as a design platform for fabrication of functionally graded structures with tailored porosity and mechanical properties according to the demand. Manufacturing bone substitutes is one of the area benefiting from the presented opportunities due to the similarity with the average properties of the cancellous bones to the

achieved results: (55-95) % porosity, 0.01 to 2 GPa for Young's modulus as well as 0.4 to100 MPa for yield stress [49], [50].

8.2 Thesis Conclusions

The following conclusions can be drawn from this study:

1. The variation in layer thickness affected the shrinkage and porosity more substantially than the samples mechanical properties, such as the modulus of elasticity and yield stress.

   The results showed that the properties of the samples which were 3D printed with a fixed layer thickness were more affected by the variation in this parameter compared to those which combined the three regions with a different layer thickness throughout the same samples.

2. A novel system and methodology were proposed to embed sacrificial porogen materials on each layer during binder-jet AM process. Analyzing the data from this study revealed the direct influence of the mesh structural properties on the porogen particles' morphology and the robustness of the results.

   Analyzing the data suggested that employing the smaller size of the needle and applying the lower amount of voltage, as well as employing a mesh with better structural properties can enhance the repeatability of the results. The results of experiments revealed a direct influence of the mesh size and shapes on the similar features of the particles.

3. Different blends of polymeric material with a variable concentration of bisphenol-A ethoxylated diacrylate and cellulose acetate butyrate (CAB) powder were introduced as a potential sacrificial material in the binder jetting-nozzle dispensing hybrid AM system.

   The material containing the maximum concentration of CAB powder (20%) demonstrated the minimum rate of infiltration (0.03 m^2/s), from the Washburn model, inside the porous Ti substrate, suggesting a better manufacturing quality by limiting the polymer – particles interface to reduce the effect of shrinkage stress. The direct influence of binder jetting process parameters such as layer thickness and binder saturation level on the quality of specimens was observed.

   The low temperature (400^{o}C) thermal decomposition behavior of the proposed polymer in the non-oxygen environment and the structural stability (1% deviation in the cavity sizes) suggested the suitability and compatibility of our approach for AM of cellular metal architectures.

4. The impact of the selectively encapsulating the proposed sacrificial photopolymer and then eliminating it from the final titanium samples throughout the sintering step was explored.

   A substantial difference in the porosity and mechanical properties was observed when the polymer was involved in the manufacturing of the samples compared to the control samples.

The porosity was increased between 6% to 16%, depending on the polymer layout in the structures. The measurement of the stiffness and yield stress suggested a range of 2.48±0.37 GPa to 3.55±0.49 GPa and 107.65±18.14 MPa to 145.75±13.85 MPa, respectively. These results suggested that the statistical significances occurred in the batches with periodic cells. The mechanical properties of the specimens with tailored closed pores revealed the significant range of decrement as 7 % to 22 % in the Young's modulus and 3% to 28 % in the Yield stress.

5. A new AM based methodology to fabricate titanium matrix composites with a focus on a Ti-TiB_w (titanium boride-whisker) matrix composite was proposed. The low-temperature pressure-less sintering method was introduced to facilitate the chemical reaction between the matrix and ceramic. The ceramic volume fraction and sintering protocol were studied as two main input variables in the design and fabrication steps.

   Evaluating the data suggested a higher possibility for formation and growth of TiB_w as the temperature elevated in the sintering step (1400°C). The ranges of 1.6±0.2 GPa to 3.7± 0.4 GPa and 83.9±18.7 MPa to 165±13.2 MPa for the Young's modulus and Yield stress of the specimens were obtained, respectively. The stiffness of the samples was enhanced significantly by increasing the temperature and volume fraction. In particular, those samples sintered up to 1400°C displayed 6.4% to 15.2% improvement in the stiffness, although only a small fraction of ceramic material was incorporated into the design: 2% and 4%, respectively. The similar trend of improvement in density of the porous matrix was observed (4.5%-19%).

8.3 Recommendations and future work

The following studies are recommended for the future investigations:

1. Future studies could focus on the effect of the wider range of the particle size and layer thickness with different configurations in addition to incorporating the different roller speeds into the structural and mechanical properties of the AM-made porous matrix to determine the sensitivity of the process to these parameters.
2. Due to the high sensitivity of the results in Chapter 5 to the structure of the meshes, tailoring the mesh design based on the application is suggested for future investigations. In addition, a wide range of materials can be suggested to be carried by the proposed PIM system including the microparticles, therapeutic agents and so on to create functionally graded structures with variable properties. This material can be loaded on paraffin or directly onto the meshes.

   For the next generation of the PIM, increasing the number of the needles and online coating of the meshes with the material can be suggested to improve the process speed and allow the embedding

of a higher number of the porogen per each layer during the AM process. In addition, including the visual feedback control to the system is suggested to manage the exact landing position of the needle on the ribbon of material to enhance the controllability of the particle locations. The PIM system can also be applied as a stand-alone module for any further applications which require the microparticle size handling or micro sampling of brittle materials.

3. Although the proposed sacrificial polymer was characterized for successful additive manufacturing of heterogeneous structures from Ti powder with a certain particle size, a similar material can be applied to other studies with variation in the type or size of the powder. Particularly because the material can be decomposed at a temperature less than 400°C, which is much lower than the sintering temperature of most metals or ceramics applied in binder jetting or other methods of AM, and the relevant high dimensional accuracy (only 1% error in the dimension of pores). Moreover, the application of the analytical model in this research can also be extended to other studies in the context of additive manufacturing when there is a possibility of liquid and porous media interaction such as selective laser melting.
4. The finding and results from analyzing the properties of cellular titanium structures resulted from decomposition of the graded polymer, can be employed as a database for further investigations. The future studies can use the data in the design step of the functionally graded structures to tailor the properties of the final product. Future studies could be focused on incorporating these findings into the design of the heterogeneous cellular samples with tailored properties based on the application.
5. Due to the substantial improvement in the properties of TMC specimens compared to the low volume fraction of the ceramic, applied sintering method, and temperature; the proposed methodology may be a useful tool for the fabrication of composite structures. Specifically the applications, which are requiring more complexity and control in the distribution and morphology of the reinforcement. Future work can focus on the development of TMC samples, with a different range of matrix particle sizes, reinforced with the variable volume fraction of developed highly loaded ceramic resin. The low decomposition temperature of the polymeric resin-base can suggest this material as a carrier of other types of ceramic powders or materials for multi-material hybrid AM of complex structures.
6. Increasing the number of experiments to identify the sensitivity of the process outputs to the input parameters of each study can be suggested. The results can be employed for creating a better and more autonomous manufacturing map in further applications.

Letters of Copyright Permission

JOHN WILEY AND SONS LICENSE TERMS AND CONDITIONS

Oct 10, 2017

This Agreement between University of Waterloo -- Esmat Sheydaeian ("You") and John Wiley and Sons ("John Wiley and Sons") consists of your license details and the terms and conditions provided by John Wiley and Sons and Copyright Clearance Center.

License Number	4205501083597
License date	Oct 10, 2017
Licensed Content Publisher	John Wiley and Sons
Licensed Content Publication	Journal of Biomedical Materials Research
Licensed Content Title	Effect of glycerol concentrations on the mechanical properties of additive manufactured porous calcium polyphosphate structures for bone substitute applications
Licensed Content Author	Esmat Sheydaeian,Mihaela Vlasea,Ami Woo,Robert Pilliar,Eugene Hu,Ehsan Toyserkani
Licensed Content Date	Jan 24, 2016
Licensed Content Pages	8
Type of use	Dissertation/Thesis
Requestor type	Author of this Wiley article
Format	Print and electronic
Portion	Full article
Will you be translating?	No
Title of your thesis / dissertation	Systems, materials, and methodologies for multi-material hybrid additive manufacturing functionally graded structures
Expected completion date	Oct 2017
Expected size (number of pages)	150
Requestor Location	University of Waterloo 200 University Ave. west Department of Mechanical and Mechatronics Waterloo, ON N2L3G1 Canada Attn: University of Waterloo
Publisher Tax ID	EU826007151
Billing Type	Invoice
Billing Address	University of Waterloo 200 University Ave. west Department of Mechanical and Mechatronics Waterloo, ON N2L3G1 Canada Attn: University of Waterloo
Total	0.00 USD

ELSEVIER LICENSE
TERMS AND CONDITIONS

Oct 10, 2017

This Agreement between University of Waterloo -- Esmat Sheydaeian ("You") and Elsevier ("Elsevier") consists of your license details and the terms and conditions provided by Elsevier and Copyright Clearance Center.

License Number	4205500626567
License date	Oct 10, 2017
Licensed Content Publisher	Elsevier
Licensed Content Publication	Additive Manufacturing
Licensed Content Title	On the effect of throughout layer thickness variation on properties of additively manufactured cellular titanium structures
Licensed Content Author	Esmat Sheydaeian,Zachary Fishman,Mihaela Vlasea,Ehsan Toyserkani
Licensed Content Date	Dec 1, 2017
Licensed Content Volume	18
Licensed Content Issue	n/a
Licensed Content Pages	8
Start Page	40
End Page	47
Type of Use	reuse in a thesis/dissertation
Portion	full article
Format	both print and electronic
Are you the author of this Elsevier article?	Yes
Will you be translating?	No
Title of your thesis/dissertation	Systems, materials, and methodologies for multi-material hybrid additive manufacturing functionally graded structures
Expected completion date	Oct 2017
Estimated size (number of pages)	150
Requestor Location	University of Waterloo 200 University Ave. west Department of Mechanical and Mechatronics Waterloo, ON N2L3G1 Canada Attn: University of Waterloo
Total	0.00 USD

ELSEVIER LICENSE
TERMS AND CONDITIONS

Oct 10, 2017

This Agreement between University of Waterloo -- Esmat Sheydaeian ("You") and Elsevier ("Elsevier") consists of your license details and the terms and conditions provided by Elsevier and Copyright Clearance Center.

License Number	4205500827815
License date	Oct 10, 2017
Licensed Content Publisher	Elsevier
Licensed Content Publication	Journal of Manufacturing Processes
Licensed Content Title	A system for selectively encapsulating porogens inside the layers during additive manufacturing: From conceptual design to the first prototype
Licensed Content Author	Esmat Sheydaeian,Ehsan Toyserkani
Licensed Content Date	Apr 1, 2017
Licensed Content Volume	26
Licensed Content Issue	n/a
Licensed Content Pages	9
Start Page	330
End Page	338
Type of Use	reuse in a thesis/dissertation
Intended publisher of new work	other
Portion	full article
Format	both print and electronic
Are you the author of this Elsevier article?	Yes
Will you be translating?	No
Title of your thesis/dissertation	Systems, materials, and methodologies for multi-material hybrid additive manufacturing functionally graded structures
Expected completion date	Oct 2017
Estimated size (number of pages)	150
Requestor Location	University of Waterloo 200 University Ave. west Department of Mechanical and Mechatronics Waterloo, ON N2L3G1 Canada Attn: University of Waterloo
Total	0.00 USD

ELSEVIER LICENSE
TERMS AND CONDITIONS

Oct 10, 2017

This Agreement between University of Waterloo -- Esmat Sheydaeian ("You") and Elsevier ("Elsevier") consists of your license details and the terms and conditions provided by Elsevier and Copyright Clearance Center.

License Number	4205500733100
License date	Oct 10, 2017
Licensed Content Publisher	Elsevier
Licensed Content Publication	Materials & Design
Licensed Content Title	Material process development for the fabrication of heterogeneous titanium structures with selective pore morphology by a hybrid additive manufacturing process
Licensed Content Author	Esmat Sheydaeian,Kaveh Sarikhani,Pu Chen,Ehsan Toyserkani
Licensed Content Date	Dec 5, 2017
Licensed Content Volume	135
Licensed Content Issue	n/a
Licensed Content Pages	9
Start Page	142
End Page	150
Type of Use	reuse in a thesis/dissertation
Intended publisher of new work	other
Portion	full article
Format	both print and electronic
Are you the author of this Elsevier article?	Yes
Will you be translating?	No
Title of your thesis/dissertation	Systems, materials, and methodologies for multi-material hybrid additive manufacturing functionally graded structures
Expected completion date	Oct 2017
Estimated size (number of pages)	150
Requestor Location	University of Waterloo 200 University Ave. west Department of Mechanical and Mechatronics Waterloo, ON N2L3G1 Canada Attn: University of Waterloo
Total	0.00 USD

Bibliography

[1] J. Sachlos, E and Czernuszka, “Making tissue engineering scaffolds work. Review on the application of solid freeform fabrication technology to the production of tissue engineering scaffolds,” *Eur. Cell. Mater.*, vol. 5, pp. 29–40, 2003.

[2] D. Tancred, B. McCormack, and A. Carr, “A synthetic bone implant macroscopically identical to cancellous bone,” *Biomaterials*, vol. 19, pp. 2303–2311, 1998.

[3] G. Ryan, A. Pandit, and D. P. Apatsidis, “Fabrication methods of porous metals for use in orthopaedic applications,” *Biomaterials*, vol. 27, no. 13, pp. 2651–2670, 2006.

[4] L. J. Gibson and M. F. Ashby, *Cellular Solids: Structure and Properties*. Cambridge University Press, 1999.

[5] J. Banhart, “Manufacture, characterisation and application of cellular metals and metal foams,” *Prog. Mater. Sci.*, vol. 46, no. 6, pp. 559–632, 2001.

[6] E. Sachlos and J. T. Czernuszka, “Making tissue engineering scaffolds work. Review: the application of solid freeform fabrication technology to the production of tissue engineering scaffolds.,” *Eur. Cell. Mater.*, vol. 5, pp. 29-39-40, 2003.

[7] S. C. Cox, J. a. Thornby, G. J. Gibbons, M. a. Williams, and K. K. Mallick, “3D printing of porous hydroxyapatite scaffolds intended for use in bone tissue engineering applications,” *Mater. Sci. Eng. C*, vol. 47, pp. 237–247, 2015.

[8] “Process for removing loose powder particles from interior passages of a body,” US5490882 A, 13-Feb-1996.

[9] a. Butscher, M. Bohner, S. Hofmann, L. Gauckler, and R. Müller, “Structural and material approaches to bone tissue engineering in powder-based three-dimensional printing,” *Acta Biomater.*, vol. 7, no. 3, pp. 907–920, 2011.

[10] S. Toyserkani, Vlase, “Systems and methods for additive manufacturing of heterogeneous porous structures and structures made therefrom,” WO2014110679 A1, 24-Jul-2014.

[11] Z. Quan *et al.*, “Additive manufacturing of multi-directional preforms for composites: Opportunities and challenges,” *Mater. Today*, vol. 18, no. 9, pp. 503–512, 2015.

[12] P. Sitthi-amorn, J. Lan, and W. Wang, “MultiFab : A Machine Vision Assisted Platform for Multi-material 3D Printing,” *ACM Trans. Graph.*, no. 34, p. 11, 2015.

[13] J. W. Choi, H. C. Kim, and R. Wicker, “Multi-material stereolithography,” *J. Mater. Process. Technol.*, vol. 211, no. 3, pp. 318–328, 2011.

[14] G. D. J. Ram, C. Robinson, Y. Yang, and B. E. Stucker, "Use of ultrasonic consolidation for fabrication of multi-material structures," *Rapid Prototyp. J.*, vol. 13, no. 4, pp. 226–235, 2007.

[15] R. J. Friel and R. A. Harris, "Ultrasonic additive manufacturing A hybrid production process for novel functional products," *Procedia CIRP*, vol. 6, no. 1, pp. 35–40, 2013.

[16] D. Bourell *et al.*, "CIRP Annals - Manufacturing Technology Materials for additive manufacturing," *CIRP Ann. - Manuf. Technol.*, vol. 1706, pp. 1–23, 2017.

[17] S. Vaucher, D. Paraschivescu, C. Andre, and O. Beffort, "Selective Laser Sintering of Aluminium-Silicon Carbide Metal Matrix Composites .," *Matrix*, vol. 199, pp. 1–8, 2002.

[18] B. Zhang, G. Bi, S. Nai, C. Sun, and J. Wei, "Optics & Laser Technology Microhardness and microstructure evolution of TiB 2 reinforced Inconel 625 / TiB 2 composite produced by selective laser melting," *Opt. Laser Technol.*, vol. 80, pp. 186–195, 2016.

[19] B. Almangour, D. Grzesiak, and J. Yang, "Rapid fabrication of bulk-form TiB 2 / 316L stainless steel nanocomposites with novel reinforcement architecture and improved performance by selective laser melting," *J. Alloys Compd.*, vol. 680, pp. 480–493, 2016.

[20] N. Kang, P. Coddet, Q. Liu, H. Liao, and C. Coddet, "In-situ TiB / near α Ti matrix composites manufactured by selective laser melting," *Addit. Manuf.*, vol. 11, pp. 1–6, 2016.

[21] Y. Shanjani and E. Toyserkani, "Material Spreading and Compaction in Powder-Based Solid Freeform Fabrication Methods: Mathematical Modeling," *Stress Int. J. Biol. Stress*, pp. 399–410, 2008.

[22] M. Vaezi and C. K. Chua, "Effects of layer thickness and binder saturation level parameters on 3D printing process," *Int. J. Adv. Manuf. Technol.*, vol. 53, pp. 275–284, 2011.

[23] W. Y. Yeong, C. K. Chua, K. F. Leong, and M. Chandrasekaran, "Rapid prototyping in tissue engineering: challenges and potential.," *Trends Biotechnol.*, vol. 22, no. 12, pp. 643–652, 2004.

[24] ASTM International, "F2792-12a - Standard Terminology for Additive Manufacturing Technologies," pp. 10–12, 2013.

[25] G. M. Utela B , Storti D , Anderson R, "A review of process development steps for new material systems in three dimensional printing (3DP)," *J. Manuf. Process.*, p. 9, 2008.

[26] S. B. Gibson I, Rosen D, *Additive Manufacturing Technologies*, 2nd ed. Springer, 2011.

[27] A. Butscher, M. Bohner, S. Hofmann, L. Gauckler, and R. Müller, "Structural and material approaches to bone tissue engineering in powder-based three-dimensional printing," *Acta*

Biomater., vol. 7, no. 3, pp. 907–920, 2011.

[28] M. Lanzetta and E. Sachs, “Improved surface finish in 3D printing using bimodal powder distribution,” *Rapid Prototyp. J.*, vol. 9, pp. 157–166, 2003.

[29] Y. Shanjani, J. N. Amritha De Croos, R. M. Pilliar, R. . Kandel, and E. Toyserkani, “Solid freeform fabrication and characterization of porous calcium polyphosphate structures for tissue engineering purposes,” *J. Biomed. Mater. Res. - Part B Appl. Biomater.*, vol. 93, pp. 510–519, 2010.

[30] Y. Shanjani, Y. Hu, R. M. Pilliar, and E. Toyserkani, “Mechanical characteristics of solid-freeform-fabricated porous calcium polyphosphate structures with oriented stacked layers,” *Acta Biomater.*, vol. 7, no. 4, pp. 1788–1796, 2011.

[31] Y. Shanjani, Y. Hu, E. Toyserkani, M. Grynpas, R. Kandel, and R. M. Pilliar, “Solid freeform fabrication of porous calcium polyphosphate structures for bone substitute applications: In vivo studies,” *J. Biomed. Mater. Res. - Part B Appl. Biomater.*, vol. 101 B, pp. 972–980, 2013.

[32] M. Vlasea, Y. Shanjani, A. Bothe, R. Kandel, and E. Toyserkani, “A combined additive manufacturing and micro-syringe deposition technique for realization of bio-ceramic structures with micro-scale channels,” *Int. J. Adv. Manuf. Technol.*, vol. 68, pp. 2261–2269, 2013.

[33] A. Basalah, Y. Shanjani, S. Esmaeili, and E. Toyserkani, “Characterizations of additive manufactured porous titanium implants,” *J. Biomed. Mater. Res. - Part B Appl. Biomater.*, vol. 100 B, no. 7, pp. 1970–1979, 2012.

[34] Y. Hu, Y. Shanjani, E. Toyserkani, M. Grynpas, R. Wang, and R. Pilliar, “Porous calcium polyphosphate bone substitutes: Additive manufacturing versus conventional gravity sinter processing - Effect on structure and mechanical properties,” *J. Biomed. Mater. Res. - Part B Appl. Biomater.*, vol. 102, pp. 274–283, 2014.

[35] M. Vlasea, E. Toyserkani, and R. Pilliar, “Effect of Gray Scale Binder Levels on Additive Manufacturing of Porous Scaffolds with Heterogeneous Properties,” *Int. J. Appl. Ceram. Technol.*, vol. 12, pp. 62–70, 2015.

[36] J. Moon, J. E. Grau, V. Knezevic, M. J. Cima, and E. M. Sachs, “Ink-jet printing of binders for ceramic components,” *J. Am. Ceram. Soc.*, vol. 85, pp. 755–762, 2002.

[37] J. Grafnetter, P. Coufal, E. Tesařová, J. Suchánková, Z. Bosáková, and J. Ševčík, “Optimization of binary porogen solvent composition for preparation of butyl methacrylate monoliths in capillary liquid chromatography,” *J. Chromatogr. A*, vol. 1049, no. 1–2, pp. 43–49, 2004.

[38] M. J. Mondrinos *et al.*, “Porogen-based solid freeform fabrication of polycaprolactone-calcium phosphate scaffolds for tissue engineering,” *Biomaterials*, vol. 27, no. 25, pp. 4399–4408, 2006.

[39] Z. Ma, C. Gao, Y. Gong, and J. Shen, “Paraffin spheres as porogen to fabricate poly(L-lactic acid) scaffolds with improved cytocompatibility for cartilage tissue engineering.,” *J. Biomed. Mater. Res. B. Appl. Biomater.*, vol. 67, no. 1, pp. 610–617, 2003.

[40] H. R. Lin, C. J. Kuo, C. Y. Yang, S. Y. Shaw, and Y. J. Wu, “Preparation of macroporous biodegradable PLGA scaffolds for cell attachment with the use of mixed salts as porogen additives,” *J. Biomed. Mater. Res.*, vol. 63, no. 3, pp. 271–279, 2002.

[41] P. X. Ma and J. W. Choi, “Biodegradable polymer scaffolds with well-defined interconnected spherical pore network.,” *Tissue Eng.*, vol. 7, no. 1, pp. 23–33, 2001.

[42] Y. Shanjani, J. N. A. De Croos, R. M. Pilliar, R. A. Kandel, and E. Toyserkani, “Solid freeform fabrication and characterization of porous calcium polyphosphate structures for tissue engineering purposes.,” *J. Biomed. Mater. Res. B. Appl. Biomater.*, vol. 93, no. 2, pp. 510–9, May 2010.

[43] N. Mohan, V. Gupta, B. Sridharan, A. Sutherland, and M. S. Detamore, “The potential of encapsulating ‘raw materials’ in 3D osteochondral gradient scaffolds,” *Biotechnol. Bioeng.*, vol. 111, no. 4, pp. 829–841, 2014.

[44] I. . Gorynin, “Titanium alloys for marine application,” *Mater. Sci. Eng. A*, vol. 263, no. 2, pp. 112–116, 1999.

[45] H. J. Rack and J. I. Qazi, “Titanium alloys for biomedical applications,” *Mater. Sci. Eng. C*, vol. 26, no. 8, pp. 1269–1277, 2006.

[46] J. E. G. González and J. C. Mirza-Rosca, “Study of the corrosion behavior of titanium and some of its alloys for biomedical and dental implant applications,” *J. Electroanal. Chem.*, vol. 471, pp. 109–115, 1999.

[47] R. R. Boyer, “An overview on the use of titanium in the aerospace industry,” *Mater. Sci. Eng. A*, vol. 213, no. 1–2, pp. 103–114, 1996.

[48] R. R. Boyer, “Titanium for aerospace: Rationale and applications,” *Adv. Perform. Mater.*, vol. 2, no. 4, pp. 349–368, 1995.

[49] B. Dabrowski, W. Swieszkowski, D. Godlinski, and K. J. Kurzydlowski, “Highly porous titanium scaffolds for orthopaedic applications,” *J. Biomed. Mater. Res. - Part B Appl. Biomater.*, vol. 95, no. 1, pp. 53–61, 2010.

[50] X. Wang *et al.*, “Biomaterials Topological design and additive manufacturing of porous

metals for bone scaffolds and orthopaedic implants : A review," *Biomaterials*, vol. 83, pp. 127–141, 2016.

[51] N. W. Bartlett *et al.*, "Robot Powered By Combustion," *Science (80-.).*, vol. 349, no. July, pp. 161–165, 2015.

[52] D. Espalin, D. W. Muse, E. MacDonald, and R. B. Wicker, "3D Printing multifunctionality: Structures with electronics," *Int. J. Adv. Manuf. Technol.*, vol. 72, no. 5–8, pp. 963–978, 2014.

[53] J. T. Muth *et al.*, "Embedded 3D printing of strain sensors within highly stretchable elastomers," *Adv. Mater.*, vol. 26, no. 36, pp. 6307–6312, 2014.

[54] S. Tibbits, "4D Printing," *Archit. Des.*, vol. 84, no. 1, pp. 116–121, 2014.

[55] J. Visser *et al.*, "Biofabrication of multi-material anatomically shaped tissue constructs.," *Biofabrication*, vol. 5, no. 3, p. 35007, 2013.

[56] N. Oxman, "Structuring Materiality: Design fabrication of heterogeneous materials," *Archit. Des.*, vol. 80, no. 4, pp. 78–85, 2010.

[57] V. Waran, V. Narayanan, R. Karuppiah, S. L. F. Owen, and T. Aziz, "Utility of multimaterial 3D printers in creating models with pathological entities to enhance the training experience of neurosurgeons.," *J. Neurosurg.*, vol. 120, no. February, pp. 489–92, 2014.

[58] A. S. Rose, J. S. Kimbell, C. E. Webster, O. L. A. Harrysson, E. J. Formeister, and C. A. Buchman, "Multi-material 3D models for temporal bone surgical simulation," *Ann. Otol. Rhinol. Laryngol.*, vol. 124, no. 7, pp. 528–536, 2015.

[59] F. Ning, W. Cong, J. Qiu, J. Wei, and S. Wang, "Additive manufacturing of carbon fiber reinforced thermoplastic composites using fused deposition modeling," *Compos. Part B Eng.*, vol. 80, pp. 369–378, 2015.

[60] B. M. & S. Y. Mohammad Vaezi , Srisit Chianrabutra, "Multiple material additive manufacturing – Part 1: a review," *Virtual Phys. Prototyp.*, vol. 8, pp. 19–50, 2013.

[61] E. Sheydaeian and E. Toyserkani, "A system for selectively encapsulating porogens inside the layers during additive manufacturing : from conceptual design to the first prototype," *J. Manuf. Process.*, vol. 26, pp. 330–338, 2017.

[62] E. Sheydaeian and E. Toyserkani, "Additive manufacturing of functionally graded titanium structures with selective closed-cells layout and controlled morphology," *Mater. Process. Technol.*, pp. 1–18, 2017.

[63] H. Sharif, “Development of a Novel Porogen Insertion System Used in Solid Freeform Fabrication of Porous Biodegradable Scaffolds with Heterogeneous Internal Architectures.” University of Waterloo, 22-Jan-2010.

[64] H. Kawamoto and K. Tsuji, “Manipulation of small particles utilizing electrostatic force,” *Adv. Powder Technol.*, vol. 22, no. 5, pp. 602–607, 2011.

[65] H. Kawamoto, “Manipulation of single particles by utilizing electrostatic force,” *J. Electrostat.*, vol. 67, no. 6, pp. 850–861, 2009.

[66] K. Takahashi, H. Kajihara, M. Urago, S. Saito, Y. Mochimaru, and T. Onzawa, “Voltage required to detach an adhered particle by Coulomb interaction for micromanipulation,” *J. Appl. Phys.*, vol. 90, no. 1, pp. 432–437, 2001.

[67] V. Vandaele, P. Lambert, and A. Delchambre, “Non-contact handling in microassembly: Acoustical levitation,” *Precis. Eng.*, vol. 29, no. 4, pp. 491–505, 2005.

[68] S. Hardt, *Microfluidic Technologies for minniaturized analysis systems*. 2007.

[69] K. K. B. Hon, L. Li, and I. M. Hutchings, “Direct writing technology-Advances and developments,” *CIRP Ann. - Manuf. Technol.*, vol. 57, no. 2, pp. 601–620, 2008.

[70] R. Fardel, M. Nagel, F. Nüesch, T. Lippert, and A. Wokaun, “Shadowgraphy investigation of laser-induced forward transfer: Front side and back side ablation of the triazene polymer sacrificial layer,” *Appl. Surf. Sci.*, vol. 255, no. 10, pp. 5430–5434, 2009.

[71] M. Kandyla, S. Chatzandroulis, and I. Zergioti, “Erratum to: Laser induced forward transfer of conducting polymers,” *Opto-Electronics Rev.*, vol. 19, no. 1, pp. 130–130, 2011.

[72] P. Serra, “Laser-induced forward Transfer: a Direct-writing Technique for Biosensors Preparation,” *J. Laser Micro/Nanoengineering*, vol. 1, no. 3, pp. 236–242, 2006.

[73] M. Vlasea and E. Toyserkani, “Experimental characterization and numerical modeling of a micro-syringe deposition system for dispensing sacrificial photopolymers on particulate ceramic substrates,” *J. Mater. Process. Technol.*, vol. 213, no. 11, pp. 1970–1977, 2013.

[74] E. Sheydaeian, K. Sarikhani, P. Chen, and E. Toyserkani, “Material process development for the fabrication of heterogeneous titanium structures with selective pore morphology by a hybrid additive manufacturing process,” *Mater. Des.*, pp. 142–150, 2017.

[75] L. J. Gibson, “Biomechanics of cellular solids,” *J. Biomech.*, vol. 38, no. 3, pp. 377–399, 2005.

[76] S. Z. G.J. Davies, “Review Metallic foams: their production, properties and applications,” *J. Mater. Sci.*, vol. 18, pp. 1899–1911, 1983.

[77] B. Kieback, A. Neubrand, and H. Riedel, “Processing techniques for functionally graded materials,” *Mater. Sci. Eng. A*, vol. 362, no. 1–2, pp. 81–105, 2003.

[78] W. Pompe *et al.*, “Functionally graded materials for biomedical applications,” *Mater. Sci. Eng. A*, vol. 362, no. 1–2, pp. 40–60, 2003.

[79] S. Wu, X. Liu, K. W. K. Yeung, C. Liu, and X. Yang, “Biomimetic porous scaffolds for bone tissue engineering,” *Mater. Sci. Eng. R*, vol. 80, pp. 1–36, 2014.

[80] A. B. Nover *et al.*, “Acta Biomaterialia Porous titanium bases for osteochondral tissue engineering,” *ACTA Biomater.*, vol. 27, pp. 286–293, 2015.

[81] H. Li, S. M. Oppenheimer, S. I. Stupp, D. C. Dunand, and L. C. Brinson, “Effects of Pore Morphology and Bone Ingrowth on Mechanical Properties of Microporous Titanium as an Orthopaedic Implant Material,” *Mater. Trans.*, vol. 45, no. 4, pp. 1124–1131, 2004.

[82] A. Gebhardt, *Understanding Additive Manufacturing*. München: Carl Hanser Verlag GmbH & Co. KG, 2011.

[83] F. Rengier *et al.*, “3D printing based on imaging data: review of medical applications,” *Int. J. Comput. Assist. Radiol. Surg.*, vol. 5, no. 4, pp. 335–341, 2010.

[84] E. Sheydaeian, M. Vlasea, A. Woo, R. Pilliar, E. Hu, and E. Toyserkani, “Effect of glycerol concentrations on the mechanical properties of additive manufactured porous calcium polyphosphate structures for bone substitute applications,” *J. Biomed. Mater. Res. Part B Appl. Biomater.*, pp. 1–6, 2016.

[85] M. Ziaee, E. M. Tridas, and N. B. Crane, “Binder-Jet Printing of Fine Stainless Steel Powder with Varied Final Density,” *Jom*, pp. 1–5, 2016.

[86] A. Mostafaei, J. Toman, E. L. Stevens, E. T. Hughes, Y. L. Krimer, and M. Chmielus, “Microstructural evolution and mechanical properties of differently heat-treated binder jet printed samples from gas- and water-atomized alloy 625 powders,” *Acta Mater.*, vol. 124, pp. 280–289, 2017.

[87] K. Lu and W. T. Reynolds, “3DP process for fine mesh structure printing,” *Powder Technol.*, vol. 187, pp. 11–18, 2008.

[88] M. Turker, D. Godlinski, and F. Petzoldt, “Effect of production parameters on the properties of IN 718 superalloy by three-dimensional printing,” *Mater. Charact.*, vol. 59, no. 12, pp. 1728–1735, 2008.

[89] B. V. J. Kruth, B. Vandenbroucke, and J. Kruth, “Selective laser melting of biocompatible metals for rapid manufacturing of medical parts,” *Rapid Prototyp. J.*, vol. 13, pp. 196–203, 2010.

[90] M. Agarwala *et al.*, “Direct selective laser sintering of metals,” *Rapid Prototyp. J.*, vol. 1, pp. 26–36, 2007.

[91] P. A. Kobryn and S. L. Semiatin, “The laser additive manufacturing of Ti-6Al-4V,” *J. Miner. Met. Mater. Soc.*, vol. 53, pp. 40–42, 2001.

[92] R. Paul and F. Gerner, “Effect of Thermal Deformation on Part Errors in Metal Powder Based Additive Manufacturing Processes,” *J. Manuf. Sci. Eng.*, vol. 136, pp. 1–12, 2016.

[93] J. Wang and L. L. Shaw, “Fabrication of Functionally Graded Materials Via Inkjet Color Printing,” vol. 3289, pp. 3285–3289, 2006.

[94] S. Farid *et al.*, “A review on powder-based additive manufacturing for tissue engineering : selective laser sintering and inkjet 3D printing A review on powder-based additive manufacturing for tissue engineering : selective laser sintering and inkjet 3D printing,” vol. 6996, 2016.

[95] ASTM Standard E9-09, “Standard Test Methods of Compression Testing of Metallic Materials at Room Temperature,” *Annu. B. ASTM Stand.*, vol. 3.01, no. 1, pp. 92–100, 2012.

[96] ASTM B-311, “Standard Test Method for Density of Powder Metallurgy (PM) Materials Containing Less Than Two Percent Porosity 1,” *ASTM Int. West Conshohocken*, pp. 1–5, 2008.

[97] W. Loop, S. Steel, B. Container, H. Source, and C. Tiles, “Standard Test Method for Water Absorption , Bulk Density , Apparent Porosity , and Apparent Specific Gravity of Fired Whiteware Products , Ceramic Tiles , and Glass Tiles 1,” pp. 1–4, 2015.

[98] J-P. Kruth P. Mercelis J. Van Vaerenbergh L. Froyen M. Rombouts, “Binding mechanisms in selective laser sintering and selective laser melting,” *Rapid Prototyp. J.*, vol. 11, pp. 26–36, 2013.

[99] J. Hinebaugh and A. Bazylak, “Pore Network Modeling to Study the Effects of Common Assumptions in GDL Liquid Water Invasion Studies,” *ASME 2012 10th Int. Conf. Fuel Cell Sci. Eng. Technol.*, pp. 479–484, 2012.

[100] Z. X. Zheng, W. Xia, and Z. Y. Zhou, “Experimental and numerical modeling for powder rolling,” *Rev. Adv. Mater. Sci.*, vol. 33, pp. 330–336, 2013.

[101] A. Budding and T. H. J. Vaneker, “New strategies for powder compaction in powder-based rapid prototyping techniques,” *Procedia - Soc. Behav. Sci.*, vol. 6, pp. 527–532, 2013.

[102] D. Ravi and D. J. Green, “Sintering stresses and distortion produced by density differences in bi-layer structures,” vol. 26, pp. 17–25, 2006.

[103] I. H. Oh, N. Nomura, N. Masahashi, and S. Hanada, “Mechanical properties of porous titanium compacts prepared by powder sintering,” *Scr. Mater.*, vol. 49, no. 12, pp. 1197–1202, 2003.

[104] M. Takemoto, S. Fujibayashi, M. Neo, J. Suzuki, T. Kokubo, and T. Nakamura, “Mechanical properties and osteoconductivity of porous bioactive titanium,” *Biomaterials*, vol. 26, no. 30, pp. 6014–6023, 2005.

[105] Z. O. U. Chun-ming, L. I. U. Yan, Y. Xin, W. Hong-wei, and W. E. I. Zun-jie, “Effect of sintering neck on compressive mechanical properties of porous titanium,” *Trans. Nonferrous Met. Soc. China*, vol. 22, pp. s485–s490, 2012.

[106] J. M. Taboas, R. D. Maddox, P. H. Krebsbach, and S. J. Hollister, “Indirect solid free form fabrication of local and global porous , biomimetic and composite 3D polymer-ceramic scaffolds,” vol. 24, pp. 181–194, 2003.

[107] S. Himran, A. Suwono, and G. A. L. I. Mansoori, “Characterization of Alkanes and Paraffin Waxes for Application as Phase Change Energy Storage Medium Characterization of Alkanes and Paraf ’ fin Waxes for Application as Phase Change Energy Storage Medium,” vol. 8312, no. July, 2016.

[108] G. Fang, Z. Chen, and H. Li, “Synthesis and properties of microencapsulated paraffin composites with SiO 2 shell as thermal energy storage materials,” *Chem. Eng. J.*, vol. 163, no. 1–2, pp. 154–159, 2010.

[109] S. Yang, K. F. Leong, Z. Du, and C. K. Chua, “The design of scaffolds for use in tissue engineering. Part I. Traditional factors.,” *Tissue Eng.*, vol. 7, no. 6, pp. 679–689, 2001.

[110] V. P. Shastri, I. Martin, and R. Langer, “Macroporous polymer foams by hydrocarbon templating,” *PNAS*, 1999.

[111] H. Tsuji, “Method for punching brittle material and punching die to be used therefor,” EP 1 078 721 A2, 2001.

[112] E. Sheydaeian, Z. Fishman, M. Vlasea, and E. Toyserkani, “On the effect of throughout layer thickness variation on properties of additively manufactured cellular titanium structures,” *Addit. Manuf.*, vol. 18, pp. 40–47, 2017.

[113] a. Laib, D. C. Newitt, Y. Lu, and S. Majumdar, “New model-independent measures of trabecular bone structure applied to in vivo high-resolution MR images,” *Osteoporos. Int.*, vol. 13, no. 2, pp. 130–136, 2002.

[114] J. S. Thomsen, E. N. Ebbesen, and L. Mosekilde, “Static histomorphometry of human iliac crest and vertebral trabecular bone: A comparative study,” *Bone*, vol. 30, no. 1, pp. 267–274, 2002.

[115] S. Boutroy, M. L. Bouxsein, F. Munoz, and P. D. Delmas, “In vivo assessment of trabecular bone microarchitecture by high-resolution peripheral quantitative computed tomography,” *J. Clin. Endocrinol. Metab.*, vol. 90, no. 12, pp. 6508–6515, 2005.

[116] T. Stylianopoulos, C. A. Bashur, A. S. Goldstein, S. A. Guelcher, and V. H. Barocas, “NIH Public Access,” vol. 1, no. 4, pp. 326–335, 2009.

[117] S. Huang, K. Xia, and F. Dai, “Dynamic Behavior of Materials, Volume 1,” vol. 1, pp. 157–163, 2011.

[118] S. Rasche and M. Kuna, “International Journal of Pressure Vessels and Piping Improved small punch testing and parameter identi fi cation of ductile to brittle materials,” *Int. J. Press. Vessel. Pip.*, vol. 125, pp. 23–34, 2015.

[119] A. Zargarian, M. Esfahanian, J. Kadkhodapour, and S. Ziaei-Rad, “Effect of solid distribution on elastic properties of open-cell cellular solids using numerical and experimental methods,” *J. Mech. Behav. Biomed. Mater.*, vol. 37, pp. 264–273, 2014.

[120] L. Yang, O. Harrysson, D. Cormier, H. West, H. Gong, and B. Stucker, “Additive Manufacturing of Metal Cellular Structures: Design and Fabrication,” *Jom*, vol. 67, no. 3, pp. 608–615, 2015.

[121] P. Sitthi-Amorn *et al.*, “MultiFab: A Machine Vision Assisted Platform for Multi-material 3D Printing,” *ACM Trans. Graph.*, vol. 34, no. 4, p. 129:1-129:11, 2015.

[122] Y. Bai, G. Wagner, and C. B. Williams, “Effect of Bimodal Powder Mixture on Powder Packing Density and Sintered Density in Binder Jetting of Metals,” *2015 Annu. Int. Solid Free. Fabr. Symp.*, p. 62, 2015.

[123] A. Basalah, S. Esmaeili, and E. Toyserkani, “On the influence of sintering protocols and layer thickness on the physical and mechanical properties of additive manufactured titanium porous bio-structures,” *J. Mater. Process. Technol.*, vol. 238, pp. 341–351, 2016.

[124] G. Kraut, L. Yenchesky, F. Prieto, G. E. M. Tovar, and A. Southan, “Influence of shear thinning and material flow on robotic dispensing of poly(ethylene glycol) diacrylate/poloxamer 407 hydrogels,” *J. Appl. Polym. Sci.*, vol. 134, no. 29, p. 45083, 2017.

[125] G. Deng and J. Zhong, “Analysis and modeling non-Newtonian fluid transferring process and dot formation in contact dispensing,” *High Density Microsyst. Des. Packag. Compon. Fail. Anal. 2005 Conf.*, no. 86, pp. 1–8, 2005.

[126] W. S. Rone, “Detc2011-4 Finite Element Modeling of a Microdroplet Generator With,” *Mechatronics*, no. iv, pp. 29–31, 2011.

[127] X. B. Chen, M. G. Li, and N. Cao, “Modeling of the fluid volume transferred in contact

dispensing processes," *IEEE Trans. Electron. Packag. Manuf.*, vol. 32, no. 3, pp. 133–137, 2009.

[128] X. B. Chen and J. Kai, "Modeling of positive-displacement fluid dispensing processes," *IEEE Trans. Electron. Packag. Manuf.*, vol. 27, no. 3, pp. 157–163, 2004.

[129] H. L. Tsai, W. S. Hwang, J. K. Wang, W. C. Peng, and S. H. Chen, "Fabrication of microdots using piezoelectric dispensing technique for viscous fluids," *Materials (Basel).*, vol. 8, no. 10, pp. 7006–7016, 2015.

[130] G. Bracco and B. Holst, *Surface science techniques*, vol. 51, no. 1. 2013.

[131] E. Eastwood, S. Viswanathan, C. P. O'Brien, D. Kumar, and M. D. Dadmun, "Methods to improve the properties of polymer mixtures: Optimizing intermolecular interactions and compatibilization," *Polymer (Guildf).*, vol. 46, no. 12, pp. 3957–3970, 2005.

[132] A. Schwarcz, N. Company, and D. Tape, "Surface Tension of Polymer Mixtures and Copolymers," *J. Polym. Sci.*, vol. 12, pp. 1195–1205, 1974.

[133] L. F. J. Schneider, L. M. Cavalcante, and N. Silikas, "Shrinkage Stresses Generated during Resin-Composite Applications: A Review.," *J. Dent. Biomech.*, vol. 2010, p. pii: 131630, 2010.

[134] H. Nagem Filho *et al.*, "Volumetric Polymerization Shrinkage of Contemporary Composite Resins," *J. Appl. Oral …*, vol. 15, no. 5, pp. 448–452, 2007.

[135] B. Lavi, A. Marmur, and J. Bachmann, "Porous media characterization by the two-liquid method: Effect of dynamic contact angle and inertia," *Langmuir*, vol. 24, no. 5, pp. 1918–1923, 2008.

[136] N. Fries and M. Dreyer, "An analytic solution of capillary rise restrained by gravity," *J. Colloid Interface Sci.*, vol. 320, no. 1, pp. 259–263, 2008.

[137] Erik O.Einset, "Capillary Infiltration Rates into Porous Media with Applications to silcomp Processing," *J. Am. Ceram. Soc.*, vol. 79, pp. 333–338, 1996.

[138] A. Moeck and R. Ag, "Shrinkage of UV Oligomers and Monomers," *Radtech Conf.*, pp. 5–9, 2014.

[139] Y. Jian, Y. He, T. Jiang, C. Li, W. Yang, and J. Nie, "Volume shrinkage of UV-curable coating formulation investigated by real-time laser reflection method," *J. Coatings Technol. Res.*, vol. 10, no. 2, pp. 231–237, 2013.

[140] R. Katsumata, S. Ata, K. Kuboyama, and T. Ougizawa, "Evaporation rate effect on starting point of shrinkage stress development during drying process in solvent cast polymer film,"

J. Appl. Polym. Sci., vol. 128, no. 1, pp. 60–65, 2013.

[141] E. O. Einset, "Capillary Infiltration Rates into Porous Media with Applications to Silcomp Processing," *J. Am. Ceram. Soc. Ceram.*, vol. 79, no. 2, pp. 333–338, 1996.

[142] A. Marmur, "Kinetics of penetration into uniform porous media: Testing the equivalent-capillary concept," *Langmuir*, vol. 19, no. 14, pp. 5956–5959, 2003.

[143] N. R. Pallas and Y. Harrison, "An automated drop shape apparatus and the surface tension of pure water," *Colloids and Surfaces*, vol. 43. pp. 169–194, 1990.

[144] K. Sarikhani, K. Jeddi, R. B. Thompson, C. B. Park, and P. Chen, "Effect of pressure and temperature on interfacial tension of poly lactic acid melt in supercritical carbon dioxide," *Thermochim. Acta*, vol. 609, pp. 1–6, 2015.

[145] K. Sarikhani, K. Jeddi, R. B. Thompson, C. B. Park, and P. Chen, "Adsorption of Surface-Modified Silica Nanoparticles to the Interface of Melt Poly(lactic acid) and Supercritical Carbon Dioxide," *Langmuir*, vol. 31, no. 20, pp. 5571–5579, May 2015.

[146] K. Sarikhani, R. Nasseri, V. Lotocki, R. B. Thompson, C. B. Park, and P. Chen, "Effect of well-dispersed surface-modified silica nanoparticles on crystallization behavior of poly (lactic acid) under compressed carbon dioxide," *Polymer (Guildf).*, vol. 98, pp. 100–109, 2016.

[147] Y. (Eds.). Neumann, A. W., David, R., Zuo, *Applied surface thermodynamics (Vol. 151)*. CRC Press: Taylor & Francis Group, 2010.

[148] A. Firooz and P. Chen, "Surface tension and adsorption kinetics of amphiphiles in aqueous solutions: the role of carbon chain length and temperature.," *J. Colloid Interface Sci.*, vol. 370, no. 1, pp. 183–91, Mar. 2012.

[149] J. N. Israelachvili, "Intermolecular and Surface Forces Third Edition," *Intermol. Surf. Forces*, p. 710, 2010.

[150] C. Academy and G. Rehage, "[~ia]b =," vol. 604, pp. 600–604, 1980.

[151] Hideo Nakae, Ryuichi Inui, Yosuke Hirata, and Hiroyuki Saito, "Effects of surface roughness on wettability," *Acta Mater.*, vol. 46, no. 7, pp. 2313–2318, 1998.

[152] D. Quéré and M. Reyssat, "Non-adhesive lotus and other hydrophobic materials," *Philos. Trans. A. Math. Phys. Eng. Sci.*, vol. 366, no. 1870, pp. 1539–1556, 2008.

[153] P. Wojciechowska, Z. Foltynowicz, and M. Nowicki, "Cellulose acetate butyrate nanocomposites synthesized via sol-gel method," *Polimery/Polymers*, vol. 58, no. 7–8, pp. 543–549, 2013.

[154] C. Xing *et al.*, “Mechanical and thermal properties of eco-friendly poly(propylene carbonate)/cellulose acetate butyrate blends,” *Carbohydr. Polym.*, vol. 92, no. 2, pp. 1921–1927, 2013.

[155] J. Parthasarathy, B. Starly, and S. Raman, “A design for the additive manufacture of functionally graded porous structures with tailored mechanical properties for biomedical applications,” *J. Manuf. Process.*, vol. 13, no. 2, pp. 160–170, 2011.

[156] T. B. Kim, S. Yue, Z. Zhang, E. Jones, J. R. Jones, and P. D. Lee, “Additive manufactured porous titanium structures: Through-process quantification of pore and strut networks,” *J. Mater. Process. Technol.*, vol. 214, no. 11, pp. 2706–2715, 2014.

[157] S. Meteyer, X. Xu, N. Perry, and Y. F. Zhao, “Energy and material flow analysis of binder-jetting additive manufacturing processes,” *Procedia CIRP*, vol. 15, pp. 19–25, 2014.

[158] H. N. G. Wadley, “Cellular metals manufacturing,” *Adv. Eng. Mater.*, vol. 4, no. 10, pp. 726–733, 2002.

[159] C. Yan, L. Hao, A. Hussein, and D. Raymont, “Evaluations of cellular lattice structures manufactured using selective laser melting,” *Int. J. Mach. Tools Manuf.*, vol. 62, pp. 32–38, 2012.

[160] T. Sheydaeian, Fishman, Vlasea, “On the effect of throughout layer thickness variation on properties of additively manufactured cellular titanium structures,” *Addit. Manuf.*, pp. 1–31, 2016.

[161] Y. Y. Zhao, T. Fung, L. P. Zhang, and F. L. Zhang, “Lost carbonate sintering process for manufacturing metal foams,” *Scr. Mater.*, vol. 52, no. 4, pp. 295–298, 2005.

[162] S. Fujibayashi, M. Neo, H. M. Kim, T. Kokubo, and T. Nakamura, “Osteoinduction of porous bioactive titanium metal,” *Biomaterials*, vol. 25, no. 3, pp. 443–450, 2004.

[163] M. Vlasea, E. Toyserkani, and R. Pilliar, “Effect of Gray Scale Binder Levels on Additive Manufacturing of Porous Scaffolds with Heterogeneous Properties,” vol. 9, pp. 1–9, 2014.

[164] J. D. Currey and K. Brear, “Hardness, Young’s modulus and yield stress in mammalian mineralized tissues,” *J. Mater. Sci. Mater. Med.*, vol. 1, no. 1, pp. 14–20, 1990.

[165] Z. Esen and Ş. Bor, “Processing of titanium foams using magnesium spacer particles,” *Scr. Mater.*, vol. 56, no. 5, pp. 341–344, 2007.

[166] E. Dudrová and M. Kabátová, “Fractography of Sintered Iron and Steels,” *Powder Metall. Prog.*, vol. 8, no. 2, pp. 59–75, 2008.

[167] A. Mortensen and J. Llorca, “Metal Matrix Composites,” *Annu. Rev. Mater. Res.*, vol. 40,

pp. 243–272, 2010.

[168] J. W. Kaczmar and K. Pietrzak, “The production and application of metal matrix composite materials,” *J. Mater. Process. Technol.*, vol. 106, pp. 58–67, 2000.

[169] S. C. Tjong and Z. Y. Ma, “Microstructural and mechanical characteristics of in situ metal matrix composites,” vol. 29, no. July, pp. 49–113, 2000.

[170] K. Morsi and V. V. Patel, “Processing and properties of titanium-titanium boride (TiBw) matrix composites - A review,” *J. Mater. Sci.*, vol. 42, no. 6, pp. 2037–2047, 2007.

[171] B. T. M. T. Godfrey, P. S. Goodwin, and C. M. Ward-close, “Titanium Particulate Metal Matrix Composites Reinforcement , Production Methods , and Mechanical Properties **,” *Adv. Eng. Mater.*, vol. 4, no. 3, pp. 85–92, 2000.

[172] R. G. Munro, “Material properties of titanium diboride,” *J. Res. Natl. Inst. Stand. Technol.*, vol. 105, no. 5, p. 709, 2000.

[173] K. B. Panda and K. S. R. Chandran, “Titanium-Titanium Boride (Ti-TiB) Functionally Graded Materials through Reaction Sintering : Synthesis , Microstructure , and Properties,” *Metall. Mater. Trans. A*, vol. 34, pp. 1993–2003, 2003.

[174] V. V Patel, A. El-desouky, J. E. Garay, and K. Morsi, “Pressure-less and current-activated pressure-assisted sintering of titanium dual matrix composites : Effect of reinforcement particle size,” *Mater. Sci. Eng. A*, vol. 507, pp. 161–166, 2009.

[175] K. S. R. Chandran, K. B. Panda, and S. S. Sahay, “TiB w -Reinforced Ti Composites : Processing , Properties , Application Prospects , and Research Needs,” *J. Miner. Met. Mater. Soc.*, vol. 56, pp. 42–48, 2004.

[176] F. M. Makau, K. Morsi, N. Gude, R. Alvarez, and M. Sussman, “Viability of Titanium-Titanium Boride Composite as a Biomaterial,” *ISRN Biomater.*, vol. 2013, pp. 1–8, 2013.

[177] A. P. I. Popoola, L. Phume, S. Pityana, and V. S. Aigbodion, “Surface & Coatings Technology In-situ formation of laser Ti6Al4V – TiB composite coatings on Ti6Al4V alloy for biomedical application,” *Surf. Coat. Technol.*, vol. 285, pp. 161–170, 2016.

[178] B. Sivakumar, R. Singh, and L. C. Pathak, “Corrosion behavior of titanium boride composite coating fabricated on commercially pure titanium in Ringer ’ s solution for bioimplant applications,” *Mater. Sci. Eng. C*, vol. 48, pp. 243–255, 2015.

[179] Y. De Hazan, J. Heinecke, A. Weber, and T. Graule, “High solids loading ceramic colloidal dispersions in UV curable media via comb-polyelectrolyte surfactants,” *J. Colloid Interface Sci.*, vol. 337, no. 1, pp. 66–74, 2009.

[180] Z. C. Eckel, C. Zhou, J. H. Martin, A. J. Jacobsen, W. B. Carter, and T. A. Schaedler, "Additive manufacturing of polymer-derived ceramics.," *Science*, vol. 351, no. 6268, pp. 58–62, 2016.

[181] P. Falkowski and a. Grzelak, "Effect ofSolvents on Curing Process of Photopolymerizable Ceramic Suspensions," *Arch. Metall. Mater.*, vol. 58, no. 4, pp. 3–6, 2013.

[182] M. L. Griffith and J. Halloran, "Ultraviolet Curing of Highly Loaded Ceramic Suspensions for Stereolithography of Ceramics," *Solid Free. Fabr. Symp.*, pp. 396–403, 1994.

[183] Y.-G. Huang, J.-R. Chen, X.-H. Zhang, H.-Q. Wang, Z. Fang, and Q.-Y. Li, "Effects of La $_2$ O $_3$ on electrolytic boronising of titanium," *Surf. Eng.*, vol. 31, no. 8, pp. 570–574, 2015.

[184] J. P. Wiff, Y. Takatsuru, and K. Matsumaru, "Fabrication of Chemical Mechanical Polishing (CMP) Pad Dresser by Using Chemical Reaction Between Diamond Abrasive Grains and Titanium Matrix," pp. 1–6, 2010.

[185] S. Sahay, K. Ravichandran, R. Atri, B. Chen, and J. Rubin, "Evolution of microstructure and phases in in situ processed Ti-TiB composites containing high volume fractions of TiB whiskers," *J. Mater. Res.*, vol. 14, no. 11, pp. 4214–4223, 1999.

[186] "Standard Test Method for Microindentation Hardness of Powder Metallurgy (PM)," pp. 1–6, 2017.

[187] M. Abdel Ghafaar, A. A. Mazen, and N. A. El-Mahallawy, "Application of the Rule of Mixtures and Halpin-Tsai Equations to Woven Fabric Reinforced Epoxy Composites," *J. Eng. Sci. Assiut Univ.*, vol. 34, no. 1, pp. 227–236, 2006.

[188] Z. Fan, Z. X. Guo, and B. Cantor, "The kinetics and mechanism of interfacial reaction in sigma fibre-reinforced Ti MMCs," *Compos. Part A Appl. Sci. Manuf.*, vol. 28, no. 2, pp. 131–140, 1997.